P-ISSN 0126-3188
E-ISSN 2443-3926

LIPI

# METALURGI

MAJALAH ILMU DAN TEKNOLOGI

VOLUME 36 Nomor 1, APRIL 2021

AKREDITASI JURNAL ILMIAH NO.3/E/KPT/2019



Pusat Penelitian Metalurgi dan Material
Lembaga Ilmu Pengetahuan Indonesia

**Sekretariat dan Penerbit :**
Pusat Penelitian Metalurgi dan Material – LIPI Ged. 470, Kawasan Puspiptek Serpong, Tangerang Selatan, 15343
Telp: (021) 7560911

E-mail:
jurnalmetalurgi@mail.lipi.go.id

Majalah ilmu dan teknologi terbit berkala setiap tahun, satu volume terdiri atas 3 nomor

# METALURGI

VOLUME 36 NOMOR 1, APRIL 2021

P-ISSN 0126-3188
E-ISSN 2443-3926

**AKREDITASI : SK No. 3/E/KPT/2019**

# PENGANTAR REDAKSI

Puji syukur Majalah Metalurgi Volume 36 Nomor 1, April 2021 kali ini dapat menampilkan 5 buah karya tulis ilmiah.

Tulisan pertama disampaikan oleh Reza Miftahul Ulum dan kawan-kawan mengenai *The Product Characteristics of Treated Ferronickel Slag Produced by Alkali Fusion and Carbothermic Process*. Tulisan kedua berjudul *Damage Investigation on Weld Aluminum Component of a Compressor After-Cooler* yang ditulis oleh Dewa Nyoman Adnyana. Tulisan selanjutnya yang ditulis oleh Made Subekti Dwijaya dan kawan-kawan dengan judul *Calcium Carbonate Deposition on Ti-6Al-6Mo Alloy*. Untuk tulisan keempat ditulis oleh Andi Mulya Anshari dan kawan-kawan menyampaikan tema *Study on Microstructure and Mechanical Properties of Mg-Zn-Fe-Cu-Co as High Entropy Alloys for Ureteral Implant*. Pada tulisan kelima, Miftakhur Rohmah dan kawan-kawan dengan judul Pengaruh Penempaan dan Perlakuan Panas terhadap Sifat Mekanik dan Ketahanan Korosi pada Modifikasi Baja Laterit A-588.

Semoga penerbitan Majalah Metalurgi volume ini dapat bermanfaat bagi perkembangan dunia penelitian di Indonesia.

**REDAKSI**

**METALURGI**

ISSN 0126 – 3188 Vol. 36 No. 1 April 2021



UDC (OXDCF) 620.18

Reza Miftahul Ulum 1, Burhanuddin As-Siraj[1], Latifa Hanum Lalasari[2], Wahyu Mayangsari[2] ([1]Departemen Teknik Metalurgi dan Material-Universitas Indonesia, [2]Pusat Penelitian Metalurgi dan Material-LIPI)

Karakteristik Produk Terak Feronikel yang dihasilkan dengan Perlakuan Fusi Alkali dan Karbotermik

Metalurgi, Vol. 36 No. 1 April 2021

Pemanfaatan terak sebagai sumber daya sekunder umumnya diolah dengan proses reduksi dengan reduktor batubara atau dengan pelindian. Namun, pada penelitian kali ini digunakan reduktor cangkang kelapa sawit sebagai alternatif pengganti batu bara. Reduktor ini dipilih karena ketersediannya di Indonesia yang memadai. Tujuan dari penelitian ini adalah untuk mengetahui pengaruh reduktor cangkang kelapa sawit dan konsentrasinya terhadap proses reduksi terak feronikel yang telah dilakukan fusi alkali sebelumnya. Sampel awal merupakan terak feronikel yang telah dihaluskan kemudian dilakukan proses fusi alkali dengan ditambahkan 20 % berat aditif natrium karbonat ($Na_2CO_3$) kemudian dilakukan roasting. Sampel tersebut kemudian dicampurkan dengan reduktor cangkang kelapa sawit dengan perbandingan (reduktor : sampel) yaitu 15:85, 20:80, dan 25:75 dalam persen berat. Sampel yang telah dicampur kemudian dikompaksi. Proses reduksi dilakukan dengan menggunakan tube furnace pada temperatur 1100 °C selama 60 menit dengan laju pemanasan 10°C/menit. Cangkang kelapa sawit dianalisis dengan menggunakan ultimate dan proximate analysis, sedangkan produk hasil reduksi kemudian dilakukan penghalusan dan pemisahan magnet secara manual. Produk hasil yang bersifat magnet dikarakterisasi dengan SEM-EDS (scanning electron microscope-energy dispersive spectroscopy) dan XRD (x-ray diffraction). Pada penelitian ini didapatkan bahwa proses reduksi menggunakan reduktor cangkang kelapa sawit menghasilkan produk berupa natrium silikat, hematit, magnetit dan logam besi. Konsentrasi reduktor optimum dalam penelitian ini adalah 15 % berat reduktor.

*Kata Kunci: Terak feronikel, fusi alkali, proses karbotermik*

*The Product Characteristics of Treated Ferronickel Slag Produced by Alkali Fusion and Carbothermic Process*

*The utilization of slag as a secondary resource is usually processed by a reduction process with coal reducing agents or by a leaching process. However, this study will use palm kernel shell as an alternative reducing agent to substitute coal. Palm kernel shell was chosen as an alternative reducing agent because of their availability in Indonesia. The purpose of this study is to determine the effect of palm kernel shell as a reducing agent and its concentration (wt.%) on the ferronickel slag reduction process. The initial sample is the ground-ferronickel slag, which had been proceeded by alkali fusion by adding 20 wt.% sodium carbonate ($Na_2CO_3$) as an additive and then roasted. The roasted product is then mixed with palm kernel shell reductant by the ratio (reductant : sample), which are 15:85, 20:80, and 25:75 in weight percent. Samples that have been mixed are then compacted. The reduction process is then carried out using a tube furnace at a temperature of 1100 °C for 60 minutes with a heating rate of 10°C/minute. The palm kernel shells were analyzed using ultimate and proximate analysis, while the reduced product was characterized ground and manually separated magnetically. The magnetic samples were then characterized by SEM-EDS (scanning electron microscope-energy dispersive spectroscopy) and XRD (x-ray diffraction). In this study, it was found that the reduction process using palm kernel shell produces products in the form of natrium silicate, hematite, magnetite, and iron metal. The optimum reducing agent concentration in this study is by adding 15 wt.% reductants.*

*Keywords: Ferronickel slag, alkali fusion, carbothermic process*

**METALURGI**

ISSN 0126 – 3188 Vol. 36 No. 1 April 2021



UDC (OXDCF) 669.722

Dewa Nyoman Adnyana (Department of Mechanical Engineering-The National Institute of Science and Technology (ISTN))

Investigasi Kerusakan pada Sambungan Las Komponen Aluminium Sebuah Alat Penukar Kalor Kompresor

Metalurgi, Vol. 36 No. 1 April 2021

Studi ini dilakukan pada sebuah alat penukar kalor kompresor yang mengalami kebocoran pada bagian sambungan las komponen yang terbuat dari paduan aluminium tanpa pengerasan perlakuan panas. Tujuan dari studi ini adalah menentukan jenis dan faktor penyebab serta mekanisme kegagalan/kerusakan dalam kaitannya dengan struktur metalurgi yang terjadi. Dalam studi ini sejumlah pengujian telah dilakukan meliputi pemeriksaan visual dan makroskopik, pengujian metalografi dan kekerasan, serta analisa SEM (scanning electron microscope) yang dilengkapi dengan EDS (energy dispersive spectroscopy). Hasil studi yang diperoleh menunjukkan bahwa jenis kegagalan yang terjadi pada alat penukar kalor kompresor adalah korosi antar-butir akibat peristiwa sensitisasi yang terjadi. Disamping itu, kerusakan yang terjadi kemungkinan juga dipengaruhi oleh cacat las yang terbentuk yaitu berupa gas porositas.

*Kata Kunci: Alat penukar kalor kompresor, investigasi kerusakan, korosi antar-butir, paduan aluminium tanpa pengerasan perlakuan panas, sensitisasi, porositas gas*

*Damage Investigation on Weld Aluminum Component of a Compressor After-Cooler*

*This study was carried out on a compressor heat exchanger (after-cooler) which leaked in the welded joint of a component made of non-heat-treatable aluminum alloys. The purpose of this study is to determine the type, cause, and mechanism of failure/damage with the metallurgical structure that occurs. In this study, several tests were carried out including visual and macroscopic examinations, metallographic and hardness testing, and SEM (scanning electron microscope) analysis equipped with EDS (energy dispersive spectroscopy). The results show that the type of failure that occurs in the compressor after-cooler is intergranular corrosion due to the sensitization that occurred in the microstructure. Besides, the damage that occurs may also be influenced by the weld defect in the form of gas porosity.*

*Keywords: Compressor heat exchanger, damage investigation, intergranular corrosion, non-heat treatable aluminum alloys, sensitization, gas porosity*

**METALURGI**

ISSN 0126 – 3188 Vol. 36 No. 1 April 2021



UDC (OXDCF) 546.38

Made Subekti Dwijaya[a], Muhammad Satrio Utomo[a], Syafira A Ramadhani[b], Fendy Rokhmanto[a], Ibrahim Purawiardi[a], Galih Senopati[a], Aprilia Erryani[a] ([a]Research Center for Metallurgy and Materials-Indonesian Institute of Sciences, [b]Sumbawa University of Technology)

Deposisi Kalsium Karbonat pada Paduan Ti-6Al-6Mo

Metalurgi, Vol. 36 No. 1 April 2021

Oseointegrasi adalah salah satu properti penting dalam pengembangan material untuk aplikasi implan tulang. Meskipun material logam biokompatibel seperti paduan titanium sudah memiliki properti biokompatibel bawaan yang sudah mencukupi sebagai material implan tulang, sifat osseointegrasi masih dapat ditingkatkan dengan pelapisan biokeramik. Kalsium karbonat ($CaCO_3$) dan hidroksiapatit adalah dua biokeramik utama pada tulang yang dapat dimanfaatkan untuk meningkatkan sifat osseointegrasi pada material implan. Tantangan saat ini pada pelapisan biokeramik pada material implant adalah memperoleh metode pelapisan yang mudah diterapkan dan ekonomis untuk selanjutnya diterapkan di industri. Pada penelitian ini dilakukan sebuah metode yang sederhana untuk mendeposisi kalsium karbonat pada permukaan Ti-6Al-6Mo. Pada kegiatan ini digunakan dua larutan biomimetik yang sudah secara luas digunakan, yaitu PBS (phosphate buffer saline) dan SCS (supersaturated calcification solution) untuk membuat pembentukan kalsium karbonat pada permukaan Ti-6Al-6Mo. Pengamatan struktur mikro dan elemental dengan SEM (scanning electron microscope) – EDS (energy dispersive spectroscopy) menunjukkan keberadaan deposit kalsium karbonat pada permukaan Ti-6Al-6Mo. Lebih lanjut, analisa kristalografi dengan difraksi sinar-x (XRD) juga menguatkan keberadaan deposit kalsium karbonat pada permukaan Ti-6Al-6Mo. Metode yang diajukan juga diterapkan pada Ti murni (>95%) sebagai perbandingan dan diperoleh hasil yang serupa. Pengaruh durasi perendaman juga diamati dalam penelitian ini. Hasil dari imersi dengan durasi 7 dan 10 hari tidak menunjukkan perbedaan yang signifikan.

*Kata Kunci: Kalsium karbonat, implan, larutan kalsifikasi lewat jenuh (SCS), paduan Ti-6Al-6Mo*

*Calcium Carbonate Deposition on Ti-6Al-6Mo Alloy*

*Osseointegration is one of the important properties in the development of implant materials for orthopedic applications. While biocompatible metallic materials such as titanium alloys should already have adequate biocompatibility properties as implant materials, their osseointegration property could be further improved by bioceramic coating. Calcium carbonate (CaCO3) and hydroxyapatite are two major bioceramics in bones that can be utilized to improve the osseointegration property of metallic implant materials. The current challenge on bioceramic coating of metallic implant materials is to obtain a coating method that is facile and economically feasible for implementation in the industry. The current activity proposes a simple and straightforward method to deposit calcium carbonate on Ti-6Al-6Mo. Two common biomimetic solutions were utilized in current activity: PBS (phosphate buffer saline) and SCS (supersaturated calcification solution) to induce the calcium carbonate formation on the Ti-6Al-6Mo surface. Microstructural and elemental observations by SEM (scanning electron microscope) – EDS (energy dispersive spectroscopy) has shown the presence of calcium carbonate on the surface of the Ti-6Al-6Mo. Moreover, the crystallography analysis by XRD (x-ray diffraction) also confirmed the formation of calcium carbonate on the surface of Ti-6Al-6Mo. We also studied the proposed method on pure Ti (>95%) as a comparison and similar outcomes were also observed. The effect on the duration of immersion was also accounted for in the current setting. The outcomes of immersion duration for 7 and 10 days were not significantly different.*

*Keywords: calcium carbonate, implant, supersaturated calcification solution (SCS), Ti-6Al-6Mo alloy*

**METALURGI**

ISSN 0126 – 3188 Vol. 36 No. 1 April 2021



UDC (OXDCF) 620.18

Andi Mulya Ashari[a], Franciska Pramuji Lestari[b], Rahma Nisa Hakim[b], Inti Mulyati[b], Yudi Nugraha Thaha[b], Ika Kartika[b], Eddy Agus Basuki[a] ([a] Departement of Metallurgical Engineering-Bandung Institute of Technology, [b]Research Center for Metallurgy and Materials-Indonesian Institute of Sciences)

# Studi Mikrostruktur dan Sifat Mekanik Mg-Zn-Fe-Cu-Co sebagai Paduan Entropi Tinggi untuk Implan Ureteral

Metalurgi, Vol. 36 No. 1 April 2021

Magnesium dan paduannya merupakan kandidat yang menjanjikan untuk bahan yang dapat terdegradasi dengan sifat biokompatibilitas yang baik. Paduan berdasarkan komposisi Mg-Zn-Fe-Cu-Co dirancang dengan metode equiatomic paduan entropi tinggi. Makalah ini membahas struktur mikro dan sifat mekanik dari paduan entropi tinggi. Serbuk Mg (60 µm), Zn (45 µm), Fe (10 µm), Cu (63 µm), dan Co (1 µm) dicampur dan digiling menggunakan shaker mill pada 700 rpm selama 30 menit di atmosfer udara pada temperatur kamar. Serbuk logam hasil gilingan yang dihasilkan dipadatkan dan disinter pada tekanan 300 MPa selama 180 detik dan 600 MPa selama 120 detik. Sintering dilakukan pada suhu 700 °C selama 2 jam dalam tungku vakum dengan laju pemanasan 5 °C / menit pada kondisi atmosfer argon dengan kemurnian tinggi. Pengaruh variasi kandungan magnesium terhadap struktur mikro dan sifat mekanik paduan Mg-Zn-Fe-Cu-Co dilakukan dengan SEM-EDS (scanning electron microscope-energy dispersive spectroscopy), XRD (x-ray diffraction) dan uji keras secara mikro. Paduannya pada dasarnya multifase dan kristal. Paduan 20Mg-20Zn-20Fe-20Cu-20Co terdiri dari fase HCP (hexagonal closed packed) dan fase kubik. Sifat fisik dan mekanik Mg-Zn-Fe-Cu-Co dipengaruhi oleh kandungan magnesium dalam paduan matriks. Adanya pori-pori mengindikasikan pemadatan dan proses sintering yang belum tuntas. Paduan memiliki kekerasan sedang antara 286,06 HV - 80,98 HV, sedangkan densitas paduan relatif sedang pada kisaran 3,057 g.cm$^{-3}$ sampai 1,71 g.cm$^{-3}$. Larutan padat dan penguatan presipitasi intermetalik diyakini sebagai mekanisme penguatan utama paduan. Disimpulkan bahwa entropi tinggi adalah metode yang menjanjikan untuk pemrosesan paduan Mg. Paduan dengan komposisi kimia 20Mg-20Zn-20Fe-20Cu-20Co memiliki sifat mekanik optimal yang memenuhi persyaratan minimum paduan entropi tinggi sebagai kandidat aplikasi implan ureter.

*Kata Kunci: Logam mampu luruh, paduan entropi tinggi, sifat mekanik, metalurgi serbuk, magnesium*

*Study on Microstructure and Mechanical Properties of Mg-Zn-Fe-Cu-Co as High Entropy Alloys for Ureteral Implant*

*Magnesium and its alloys are promising candidates for degradable materials with good biocompatibility. Alloys based on Mg-Zn-Fe-Cu-Co compositions were designed using equiatomic method of high entropy alloy. This paper discusses the microstructure and mechanical properties of these new high entropy alloy. Pure Magnesium (60 µm), Zinc (45 µm), Fe (10 µm), Cu (63 µm), and Co (1 µm) powder were mixed and milled using a shaker mill at 700 rpm for 30 minutes in air atmosphere at room temperature. The resulting milled powders were compacted and sintered at 300 MPa for 180 s and 600 MPa for 120 s. Sintering was performed at 700 °C for 2 hours in a tube vacuum furnace at 5 °C/min heating rate under high purity argon atmosphere. The effect of variations in magnesium content on the microstructure (SEM-EDS and XRD) and mechanical properties (micro hardness tester) of the Mg-Zn-Fe-Cu-Co alloy were performed. The alloys were basically multiphase and crystalline. The 20Mg-20Zn-20Fe-20Cu-20Co alloy consisted of HCP (hexagonal closed packed) phase and cubic phase. The physical and mechanical properties of Mg-Zn-Fe-Cu-Co were affected by the magnesium content in the matrix alloys. The presence of pores indicated uncomplete compaction and sintering process. The alloys have a medium hardness of between 286.06 HV - 80.98 HV, while the densities of the alloys were relatively moderate in the range of 3.057 g.cm$^{-3}$ to 1.71 g.cm$^{-3}$. Solid solution and intermetallic precipitation strengthening were believed the primary strengthening mechanics of the alloys. It is concluded that high entropy is a promising method for the processing of Mg alloys. Alloy with chemical composition of 20Mg-20Zn-20Fe-20Cu-20Co had optimal mechanical properties that meet the minimum requirements of high entropy alloys as candidate for ureteral implant applications.*

*Keywords: Biodegradable metal, high entropy alloy, mechanical properties, powder metallurgy, magnesium*

**METALURGI**

ISSN 0126 – 3188 Vol. 36 No. 1 April 2021



UDC (OXDCF) 620.112

Miftakhur Rohmah, Dedi Irawan, Toni Bambang Romijarso (Pusat Penelitian Metalurgi dan Material-LIPI)

Pengaruh Penempaan dan Perlakuan Panas terhadap Sifat Mekanik dan Ketahanan Korosi pada Modifikasi Baja Laterit A-588

Metalurgi, Vol. 36 No. 1 April 2021

Baja paduan rendah berkekuatan tinggi yang diaplikasikan menjadi baja tahan cuaca merupakan terobosan terbaru untuk menghasilkan sifat mekanik dan ketahanan korosi yang tinggi. Modifikasi baja laterit dengan penambahan kadar nikel yang diterapkan proses termomekanikal terkontrol (TMCP) berupa kombinasi proses penempaan panas dan perlakuan panas menjadi fokus penelitian ini, dimana nikel berfungsi sebagai penstabil austenit. Sampel yang digunakan merupakan baja laterit A-588 hasil *investment casting* yang ditambahkan 1, 2, dan 3 %berat nikel, kemudian diproses penempaan panas dengan pembebanan 100 ton pada temperatur 1050 ℃. Variabel perlakuan panas yang digunakan yakni (1) langsung pendinginan udara, (2) dilanjutkan proses pemanasan pada temperatur 750 ℃ yang diikuti pendinginan cepat. Karakterisasi material menggunakan uji metalografi, uji keras, uji tarik, dan uji polarisasi. Pada hasil tempa panas+pendinginan udara, pertambahan kadar nikel hingga 3 %massa mempengaruhi nilai fraksi fasa ferit-perlit yang terbentuk, pertambahan ukuran butir hingga ±0,1 mm, penurunan kekerasan hingga 185,22 BHN, penurunan kekuatan hingga 554 MPa, dan pertambahan regangan sebesar 29,1%. Sedangkan pada hasil tempa panas+perlakuan panas dengan pendinginan air, pertambahan nikel hingga 3 %massa menyebabkan terbentuknya fasa dislokasi bilah martensit + ferit + austenit sisa, penurunan kekerasan hingga 236,18 BHN, penurunan kekuatan hingga 852 MPa, penurunan regangan hingga 24,7%. Fasa austenit sisa (*retained austenite)* memiliki efek merusak pada sifat mekanis.

*Kata Kunci: Baja laterit A-588, austenit sisa, modifikasi baja laterit, tempa panas*

*Effect of Forging and Heat Treatment on the Mechanical Properties and Corrosion Resistance in A-588 Lateritic Steel Modified*

*The application of HSLA (high-strength low alloy) for weathering steels is the newest innovation to produce high mechanical and corrosion resistance properties. Modification of laterite steel by nickel addition with a TMCP (thermomechanical control process) in the form of a combination of hot forging and heat treatment processes is the focus of this study, in which a nickel acts as an austenite stabilizer. The sample used was A-588 Lateritic Steel, resulting from investment casting, which has added nickel content of 1, 2, and 3%, then processed by hot forging with 100 tons loading at 1050 ℃. Heat treatment variables used were (1) direct air cooling and (2) followed by a heating process at a temperature of 750 ℃ followed by a rapid cooling process. Material characterization was using a metallographic test, hardness test, tensile test, and polarization test. In hot forging + air cooling samples, the increase in nickel content up to 3 %mass affects the value of the ferrite-pearlite phase fraction formed, the increase in grain size up to ± 0,1 mm, the decrease in hardness is up to 185.22 BHN, the decline in strength is up to 554 MPa, and the elongation increase is 29.1%. Whereas in the hot forging sample + heat treatment with water cooling, the rise in nickel up to 3 %mass causes the formation of martensite + ferrite + retained austenite lath dislocation phase, a decrease in hardness to 236.18 BHN, a reduction in strength to 852 MPa, a decrease in elongation up to 24.7%. The retained austenite phase has a detrimental effect on mechanical properties.*

*Keywords: Lateritic steel A-588, retained austenite, lateritic steel modification, hot forging*

METALURGI
Majalah Ilmu dan Teknologi
p-ISSN 0126-3188 | e-ISSN 2443-3926
www.ejurnalmaterialmetalurgi.com

# THE PRODUCT CHARACTERISTICS OF TREATED FERRONICKEL SLAG PRODUCED BY ALKALI FUSION AND CARBOTHERMIC PROCESS

**Reza Miftahul Ulum[a,*], Burhanuddin As-Siraj[a], Latifa Hanum Lalasari[b], Wahyu Mayangsari[b]**

[a]Departemen Teknik Metalurgi dan Material, Universitas Indonesia
Jl. Kampus UI Depok, Depok, Jawa Barat, Indonesia 16424
[b] Pusat Penelitian Metalurgi dan Material
Gedung 470, Kawasan PUSPIPTEK Serpong, Tangerang Selatan, Indonesia 15343
*E-mail: reza.ulum@ui.ac.id

*Masuk tanggal : 06-01-2021, revisi tanggal : 26-01-2021, diterima untuk diterbitkan tanggal 30-04-2021*

## Abstrak

Pemanfaatan terak sebagai sumber daya sekunder umumnya diolah dengan proses reduksi dengan reduktor batu bara atau dengan pelindian. Namun, pada penelitian kali ini digunakan reduktor cangkang kelapa sawit sebagai alternatif pengganti batu bara. Reduktor ini dipilih karena ketersediannya di Indonesia yang memadai. Tujuan dari penelitian ini adalah untuk mengetahui pengaruh reduktor cangkang kelapa sawit dan konsentrasinya terhadap proses reduksi terak feronikel yang telah dilakukan fusi alkali sebelumnya. Bahan awal merupakan terak feronikel yang telah dihaluskan kemudian dilakukan proses fusi alkali dengan ditambahkan 20 %berat aditif natrium karbonat ($Na_2CO_3$) kemudian dilakukan *roasting*. Sampel tersebut kemudian dicampurkan dengan reduktor cangkang kelapa sawit dengan perbandingan (reduktor : sampel) yaitu 15:85, 20:80, dan 25:75 dalam persen berat. Sampel yang telah dicampur kemudian dikompaksi. Proses reduksi dilakukan dengan menggunakan *tube furnace* pada temperatur 1100 °C selama 60 menit dengan laju pemanasan 10 °C/menit. Cangkang kelapa sawit dianalisis dengan menggunakan *ultimate* dan *proximate analysis*, sedangkan produk hasil reduksi kemudian dilakukan penghalusan dan pemisahan magnet secara manual. Produk hasil yang bersifat magnet dikarakterisasi dengan SEM-EDS (*scanning electron microscope-energy dispersive spectrometry*) dan XRD (*x-ray diffraction*). Pada penelitian ini didapatkan bahwa proses reduksi menggunakan reduktor cangkang kelapa sawit menghasilkan produk berupa natrium silikat, hematit, magnetit dan logam besi. Konsentrasi reduktor optimum dalam penelitian ini adalah 15 %berat reduktor.

**Kata Kunci:** Terak feronikel, fusi alkali, proses karbotermik

## Abstract

*The utilization of slag as a secondary resource is usually processed by a reduction process with coal reducing agents or by a leaching process. However, this study will use palm kernel shell as an alternative reducing agent to substitute coal. Palm kernel shell was chosen as an alternative reducing agent because of their availability in Indonesia. The purpose of this study is to determine the effect of palm kernel shell as a reducing agent and its concentration (wt.%) on the ferronickel slag reduction process. The raw material is the ground-ferronickel slag, which had been proceeded by alkali fusion by adding 20 wt.% sodium carbonate ($Na_2CO_3$) as an additive and then roasted. The roasted product is then mixed with palm kernel shell reductant by the ratio (reductant : sample), which are 15:85, 20:80, and 25:75 in weight percent. Samples that have been mixed are then compacted. The reduction process is then carried out using a tube furnace at a temperature of 1100 °C for 60 minutes with a heating rate of 10 °C/minute. The palm kernel shells were analyzed using ultimate and proximate analysis, while the reduced product was characterized ground and manually separated magnetically. The magnetic samples were then characterized by SEM-EDS (scanning electron microscope-energy dispersive spectrometry) and XRD (x-ray diffraction). In this study, it was found that the reduction process using palm kernel shell produces products in the form of natrium silicate, hematite, magnetite, and iron metal. The optimum reducing agent concentration in this study is by adding 15 wt.% reductants.*

***Keywords:*** *Ferronickel slag, alkali fusion, carbothermic process*

## 1. INTRODUCTION

Nickel laterite is the result of natural weathering from ultramafic processes. Based on the chemical composition, nickel types laterite are divided into two, which are limonite and saprolite. Limonite ($FeO(OH)\text{-}nH_2O$) has a nickel composition of 0.7-1% from the total mass and has a rich iron (Fe) composition. On the other hand, saprolite ($(Ni,Mg)Si_4O_5(OH)_4$) contains 1.5-2.5% of nickel with a high amount of $Mg\text{-}SiO_2$ [1]. The products from nickel laterite by pyrometallurgical processing are both ferronickel and its by-product known as slag.

One of the methods to utilize ferronickel slag is to reduce the slag by using a reducing agent. In general, the reduction process uses coal or coke as the reducing agent. The ferronickel slag is considered as waste; thus, a low-cost reduction operation needs to be used. Palm kernel shells is an alternative reducing agent with a low selling value compared to coal or even coke. Similar to that of coal, the reduction reactions of palm kernel shell will involve the oxidation of carbon to CO gas, which acts as a reducing gas in the carbothermic reaction.

The palm kernel shell is considered a biomass product that has a high-calorie content and a high net calorific value. It provides a great number of burning calories and leads to significant heat generation from its combustion [2]. Its high calorific value means that the palm kernel shell has the potential to be also used as an alternative energy source to replace coal.

The palm kernel shell availability is relatively abundant because Indonesia is a tropical country with several palm oil land. Indonesia is the largest palm oil producer in the world [3]. As the palm oil industry and land in the industry developed, the production of waste from palm oil extraction will also increase every year. The palm kernel shell waste is usually disposed of immediately. The waste will give a negative impact on the surrounding environment if it is not managed carefully.

Arum Cahyanurani S. et al., [4] reported that the valuable metals in the slag are difficult to be separated due to their bonding in the silica-iron matrix in the fayalite phase, which is a dominant phase in ferronickel slag. Moreover, M. D. Alfariz et. al., [5] reported that increasing nickel and iron content can be obtained by the reduction process of ferronickel slag using palm kernel shell charcoal as reducing agent and $Na_2CO_3$ as an additive in one stage. The use of the additive in alkali fusion can facilitate the decomposition of the silica-iron matrix which leads to easier precious metals recovery. By combining the alkali fusion and reduction (carbothermic) process in different stages, this study aims to analyze the products of the alkali fusion and carbothermic reduction of ferronickel slag using palm kernel shell as a reducing agent.

## 2. MATERIALS AND METHODS

The ground ferronickel slag with particle size 75 microns was used in this study. The sample was first treated by alkali fusion processing. This process was carried out by mixing the sample with 20 wt.% sodium carbonate, compacting the sample and heating the sample in the tube furnace for 1 hour at 1100 °C. At the end of each experiment, the product was furnace cooled. Before the carbothermic process was conducted, the sample was then ground and mixed by 15, 20, and 25 wt.% palm kernel shell as a reductant, and the mixtures were compacted. Proximate and ultimate analysis was carried out to determine the main content of the reducing agent used in the experiments. The proximate and ultimate test results can be seen in Table 1 and Table 2. Meanwhile, the initial slag composition from the XRF (x-ray flourescence) analysis is shown in Table 3.

The carbothermic process was performed by heating the sample in the tube furnace at 1100 °C for 1 hour in an inert atmosphere, with a heating rate of 10°C/minute. The carbothermic product was then ground and separated magnetically by a permanent magnet manually. The magnetic particles from each carbothermic product are then characterized by SEM-EDS (scanning electron mycroscope-energy dispersive spectroscopy) and XRD (x-ray diffraction) for further analysis.

Table 1. Proximate analysis results

| No. | Palm Kernel Shell Proximate analysis results (%) | |
|---|---|---|
| 1 | *Moisture* | 6.10 |
| 2 | *Ash* | 3.36 |
| 3 | *Volatile Matter* | 12.00 |
| 4 | *Fixed Carbon* | 78.54 |

Table 2. Ultimate analysis results

| No. | Palm Kernel Shell Ultimate analysis result (%) | |
|---|---|---|
| 1 | Sulphur | 0.02 |
| 2 | Carbon | 80.79 |
| 3 | Hydrogen | 2.85 |
| 4 | Nitrogen | 0.89 |
| 5 | Oxygen | 12.09 |

Tables 1 and 2 show that the carbon content of palm kernel shells is 80.79% and it has a fixed carbon level of 78.54%. The higher the carbon content in a reducing agent, the more likely CO-$CO_2$ will be formed and act as the main reducing agent for the reduction process [6]. The slag's major components are $SiO_2$, $Fe_2O_3$, MgO, $Al_2O_3$, and others as shown in Table 3.

Table 3. Slag initial composition from XRF analysis

| Compounds | $Na_2O$ | MgO | $Al_2O_3$ | $SiO_2$ | CaO |
|---|---|---|---|---|---|
| Wt.% | 0.56 | 29.5 | 5.34 | 46.76 | 0.81 |
| Compounds | $Fe_2O_3$ | NiO | ZnO | $Cr_2O_3$ | Others |
| Wt.% | 13.3 | 0.085 | 0.029 | 1.55 | 2.066 |

## 3. RESULTS AND DISCUSSIONS

The XRD (x-ray diffraction) result of the alkali fusion product is shown in Fig. 1. The compounds contained in the product from alkali fusion, which is named as a roasted product in this study, are quartz ($SiO_2$), sodium silicate ($Na_2SiO_3$), fayalite ($Fe_2SiO_4$), and hematite ($Fe_2O_3$). The sodium silicate ($Na_2SiO_3$) appears to form during the alkali fusion process; this was not identified in the previous study [4]-[5].

### 3.1. Alkali Fusion Results

Sodium silicate is formed by the reaction between ($Na_2CO_3$) and quartz according to reactions (1) to (3) [7].

$$Na_2CO_3 \rightarrow Na_2O + CO_2 \quad (1)$$
$$Na_2O + SiO_2 \rightarrow Na_2SiO_3 \quad (2)$$
$$Na_2CO_3 + SiO_2 \rightarrow Na_2SiO_3 + CO_2 \quad (3)$$

Reactions (1) to (3) in this study occurs between sodium carbonate and silicate from the ferronickel slag which produces $Na_2SiO_3$. First, the additive sodium carbonate ($Na_2CO_3$) decomposes into sodium oxide ($Na_2O$) and carbon dioxide ($CO_2$) via reaction (1). The sodium oxide ($Na_2O$) is then reacted with quartz ($SiO_2$) to produce sodium silicate ($Na_2SiO_3$) according to reaction (2) [7]. The sodium carbonate additive ($Na_2CO_3$) can react with the fayalite phase ($Fe_2SiO_4$) which produces several compounds such as hematite ($Fe_2O_3$), sodium silicate ($Na_2SiO_3$), and carbon monoxide gas (CO) based on the reaction of (4) [8]. The products formed in this study are similar to those reported in the literature from the roasting process using sodium carbonate ($Na_2CO_3$) at a temperature of 1100 °C [7].

$$Fe_2SiO_4 + Na_2CO_3 \rightarrow Fe_2O_3 + Na_2SiO_3 + CO \quad (4)$$

SEM-EDS (scanning electron microscope-energy dispersive spectroscopy) analysis for the roasted products (before the carbothermic process is conducted) is shown in Fig. 3. Figure 3 shows that 4 different locations in the sample have been analyzed to determine the elemental content of the roasted product, which is shown in Table 4. Figure 3 shows that the morphology of the roasted product consists of dominant colors of black and gray (dark) which indicated the domination of oxygen/oxide compound.

The observation areas of numbers 1 and 4 have a similarity based on their white color's appearance. According to Table 1, it can be analyzed that the Fe levels in the observation areas of numbers 1 and 4 are the highest compared to other observation areas. The white areas have high iron content, i.e. 10.7 and 14.8 wt.% for areas number 1 and 4 with, respectively. In the area of number 2, a dominant gray (dark) color can be observed. This indicates the predominant constituent of oxygen at 41.3 wt.%. While in area number 3, a slightly mixed gray (dark) and white content can be observed. Area number 3 consists of 39.2 wt.% oxygen.

### 3.2. Carbothermic Process Results

After the carbothermic process is done, all of the samples were ground into a powder, separated magnetically using a permanent magnet. Almost all of the particles were attracted to the magnet. This carbothermic product was then characterized by XRD and SEM-EDS analysis. The effect of palm kernel shell utilization as a reductant on the carbothermic process of the roasted product from the XRD analysis is shown in Fig. 3. The combination of alkali fusion and carbothermic process shows a tendency to decompose the fayalite phase producing some compounds that can be reduced easier during the carbothermic reduction process. This results in the formation of hematite, magnetite, and iron metal.

Hematite formed due to the fayalite reaction with the additives will be reduced to magnetite, to wustite (FeO), and eventually to ferrous metal (Fe) according to the reaction (5) to (7)[9].

$$3Fe_2O_3 + CO \rightarrow 2Fe_3O_4 + CO_2 \quad (5)$$
$$Fe_3O_4 + CO \rightarrow 3FeO + CO_2 \quad (6)$$
$$FeO + CO \rightarrow Fe + CO_2 \quad (7)$$

Besides, it clearly shows the inequality between one and two stages of the alkali fusion and reduction (carbothermic) process. Fe phase formed when two stages of heat treatment were performed, while Fe was bonded in the phase of

fayalite when heat treatment carried out in one stage [5].

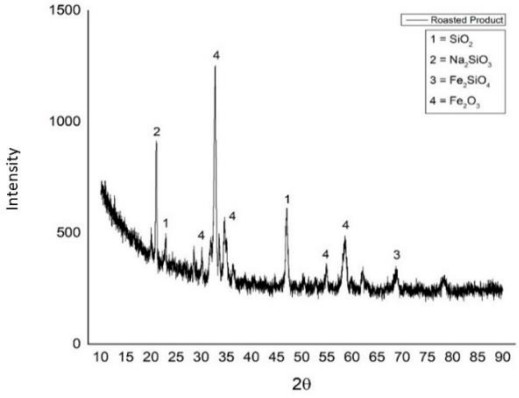


Figure 1. XRD analysis result of the roasted product

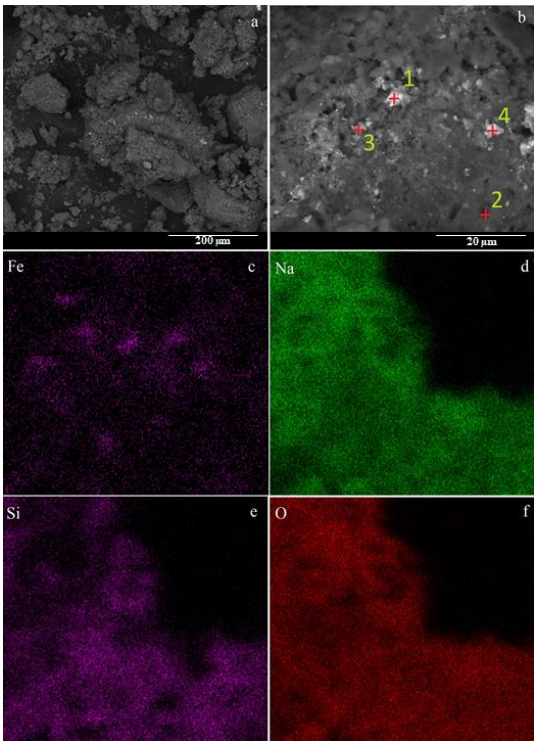


Figure 2. SEM-EDS analysis showing elemental mapping analysis of the roasted product

The effect of variation of palm kernel concentration on the formations of iron (Fe), hematite ($Fe_2O_3$), and magnetite ($Fe_3O_4$) detected in the carbothermic products can be analyzed by XRD analysis. Based on the analysis of the peak height of the iron metal phase, the palm kernel shell addition of 15 wt.% appears to give the highest Fe peak, followed by the palm kernel shell addition of 25 wt.% and 20 wt.%.

The hematite compound's peak height appears to be at the highest at 25 wt.% palm kernel shell addition, followed by the 15 wt.% and 20 wt.% palm kernel shell. Meanwhile, the magnetite compound's peak height appears to be at the highest at 15 wt.% palm kernel shell addition, followed by 25 wt.% and 20 wt.% palm kernel shell addition.

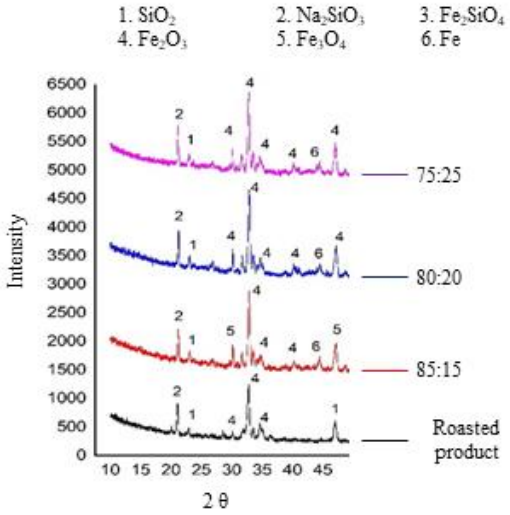


Figure 3. XRD analysis results of the carbothermic products from 75:25, 80:20 and 85:15 (roasted product : palm kernel shell reductant: 25, 20 and 15 wt.% respectively)

Based on the three prominent peaks in this study, the carbothermic process seems to give the most to the less optimum result at the palm kernel shell addition of 15 wt.%, 25 wt.%, and 20 wt.%. To further validate the result, the elemental mapping by SEM-EDS analysis is performed on the carbothermic product from the 15 wt.% palm kernel shell addition as shown in Fig. 4.

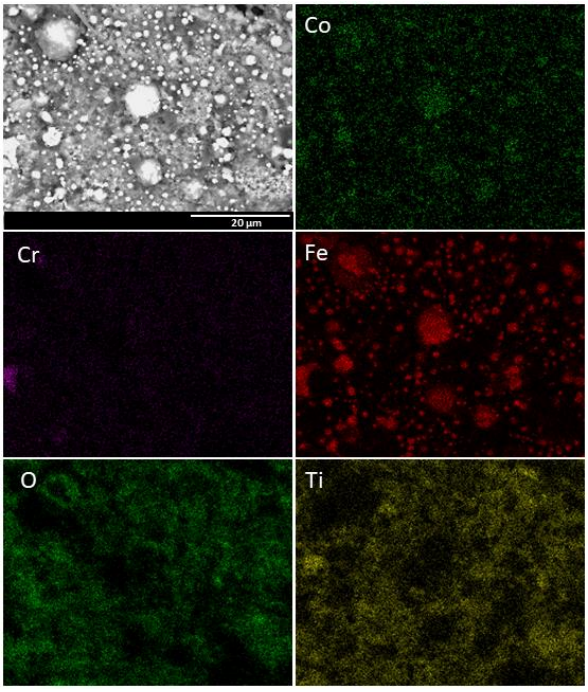


Figure 4. SEM-EDS analysis showing elemental mapping analysis of the carbothermic reduction product from 15 wt.% palm kernel shell addition

Tabel 4. SEM-EDS analysis of the initial roasted product shown in the Fig. 2

| Element (wt/%) | Observation Area | | | |
|---|---|---|---|---|
| | 1 | 2 | 3 | 4 |
| O | 30.4 | 41.3 | 39.2 | 26.1 |
| Na | 35.2 | 27.4 | 31.2 | 21.7 |
| Mg | 0.68 | 0.19 | 0.13 | 0.51 |
| Al | 5.19 | 10.7 | 7.30 | 4.63 |
| Si | 7.8 | 11.4 | 8.92 | 6.03 |
| P | 3.04 | 2.20 | 5.44 | 2.74 |
| Sn | 0.87 | 0.56 | 0.6 | 4.56 |
| Ca | 1.42 | 2.76 | 1.81 | 4.58 |
| Ti | 0.65 | 0.45 | 1.16 | 3.92 |
| Mn | 0.81 | 0.29 | 0.34 | 4.37 |
| Fe | 10.7 | 1.96 | 2.95 | 14.8 |
| Co | 1.35 | 0.44 | 0.44 | 3.21 |
| Ni | 1.35 | 0.35 | 0.51 | 2.85 |

As shown in Fig. 4, it indicates that the carbothermic product from the 15 wt.% palm kernel shell addition consists of Fe-containing particles formed after the alkali fusion and carbothermic process. The SEM-EDS result shown in Fig. 4 is in agreement with the XRD result provided in Fig. 3.

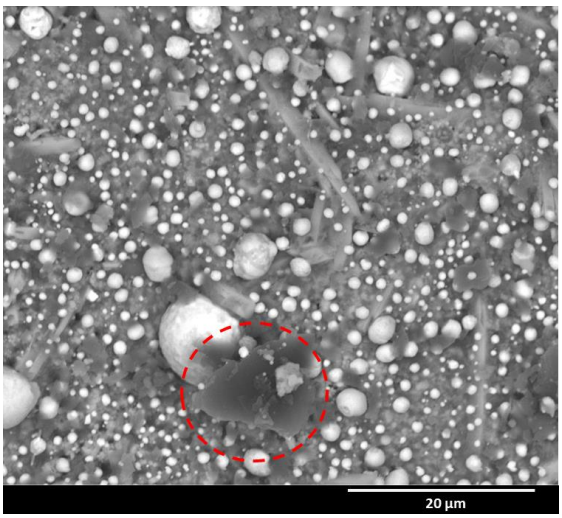

Figure 5. SEM-EDS analysis of the carbothermic reduction product from 20 wt.% palm kernel shell addition

It is expected that the more palm kernel shell addition, the more metallic iron would be produced since there is more carbon source. However, the present result shows contradiction. The contradiction can be explained by SEM-EDS analysis of the carbothermic products from the 20 wt.% palm kernel shell addition is shown in Fig. 5. Figure 5 indicates that the more palm kernel shell addition, the more dark particles are observed in the carbothermic product (area marked with a dashed circle in Fig.5). According to EDS analysis shown in Table 5, the particles are dominantly composed of carbon. The result indicates that the carbon source was not completely oxidized into CO or $CO_2$ gas which may be caused by the lack of carbothermic reduction time. The residual carbon may be avoided by the use of the finer size of palm kernel shell to accelerate the formation of $CO/CO_2$ gas during the carbothermic reduction process.

Tabel 5. SEM-EDS analysis of the carbothermic reduction product shown the Fig. 5

| Element | Wt.% | At.% |
|---|---|---|
| C | 73.31 | 82.55 |
| O | 14.63 | 12.37 |
| Na | 3.86 | 2.27 |
| Mg | 0.51 | 0.28 |
| Al | 0.82 | 0.41 |
| Si | 1.33 | 0.64 |
| P | 0.67 | 0.29 |
| Sn | 0.81 | 0.09 |
| Ca | 1.04 | 0.35 |
| Ti | 0.44 | 0.12 |
| Cr | 0.16 | 0.04 |
| Mn | 0.26 | 0.06 |
| Fe | 1.34 | 0.33 |
| Co | 0.51 | 0.12 |
| Ni | 0.31 | 0.07 |

The present study demonstrates the possible application of the combined alkali fusion and carbothermic process for the treatment of ferronickel slag processing as a secondary source of iron. However, the energy consumption of the combined alkali fusion and the carbothermic process is relatively high due to the two separate heating stages applied in the process.

## 4. CONCLUSIONS

The use of alkali fusion followed by the carbothermic process results in the decomposition of the ferronickel slag. The silica-iron matrix in the fayalite phase appears to change into different compounds, one of which is $Na_2SiO_3$. The carbothermic reduction products can be separated by a magnetic separation process. The optimal addition of palm kernel shell was at 15 wt.% which produced various carbothermic products, such as natrium silicate, hematite, magnetite, and iron metal.

## ACKNOWLEDGEMENT

The authors would like to express their gratitude for the funding from PUTI 2020 Universitas Indonesia NKB-2028/UN2.RST/HKP.05.00/2020.

## REFERENCES

[1] Tim-Bestekin, "Nickel Ore Sulawesi," 2016. [Online]. Available: https://bestekin.com/2016/02/01/nickel-ore-sulawesi/. [Accessed: 22-Sep-2019].

[2] R. Z. Abd Rashid, H. Mohd. Salleh, M. H. Ani, N. A. Yunus, T. Akiyama, and H. Purwanto, "Reduction of low grade iron ore pellet using palm kernel shell," *Renewable Energy*, vol. 63, pp. 617–623, 2014.

[3] R. Kurniawan and S. Managi, "Coal consumption, urbanization, and trade openness linkage in Indonesia," *Energy Policy*, vol. 121, pp. 576–583, 2018.

[4] A. C. Setyabrata, A. Maksum, A. B. Prasetyo, B. Priyono, and J. Wahyuadi Soedarsono, "Effect of Sodium Carbonate on the Reduction Process of Nickel Slag from Sulawesi," in *IOP Conference Series: Materials Science and Engineering*, vol. 553, no. 1, p. 012028, 2019.

[5] M. D. Alfariz, W. Mayangsari, a. B. Prasetyo, A. Mksum, T. Prasetyo, R. M. Ulum, and J. W. Soedarsono, "Effect of sodium carbonate ($Na_2CO_3$) additives and palm kernel shell charcoal to increase nickel and iron content from ferronickel slag using the pyrometallurgical method," in *The 4th International Tropical Renewable Energy Conference (i-TREC 2019) AIP Conf. Proc.*, vol. 040030, pp. 1–6, 2020.

[6] J. W. Soedarsono, C. E. Arifin, J. S. Saragi, A. A. Putra, A. Kawigraha, R. D. S. Ariobimo, and A. Rustandi, "The effect of reduction parameter in processing lump ore with green sugarcane bagasse reductor in muffle furnace," in *Materials Science Forum*, vol. 893, pp. 195–201, 2017. Doi : 10.4028/www.scientific.net/MSF.893.195.

[7] A. B. Prasetyo, A. Maksum, J. W. Soedarsono1, and F. Firdiyono, "Thermal characteristics of ferronickel slag on roasting process with addition of sodium carbonate ($Na_2CO_3$)," in *International Seminar on Metallurgy and Materials*, vol. 541, pp. 012037, 2019. Doi: 10.1088/1757-899X/541/1/012037.

[8] M. Jiang, T. Sun, Z. Liu, J. Kou, N. Liu, and S. Zhang, "Mechanism of sodium sulfate in promoting selective reduction of nickel laterite ore during reduction roasting process," *International Journal of Mineral Processing*, vol. 123, pp. 32–38, 2013.

[9] S. K. Haldar, *Mineral Exploration Principles and Applications*, 2nd ed. Elsevier, 2018.

Metalurgi (2021) 1: 7 - 16

LIPI

METALURGI
Majalah Ilmu dan Teknologi
p-ISSN 0126-3188 | e-ISSN 2443-3926
www.ejurnalmaterialmetalurgi.com

# DAMAGE INVESTIGATION ON WELD ALUMINUM COMPONENT OF A COMPRESSOR AFTER-COOLER

**Dewa Nyoman Adnyana**
Department of Mechanical Engineering, Faculty of Industrial Technology
The National Institute of Science and Technology (ISTN), Jakarta Selatan, Indonesia 12640
E-mail : adnyanadn@yahoo.com

*Masuk tanggal : 18-12-2020, revisi tanggal : 29-01-2021, diterima untuk diterbitkan tanggal 30-04-2021*

## Abstrak

Studi ini dilakukan pada sebuah alat penukar kalor kompresor yang mengalami kebocoran pada bagian sambungan las komponen yang terbuat dari paduan aluminium tanpa pengerasan perlakuan panas. Tujuan dari studi ini adalah menentukan jenis dan faktor penyebab serta mekanisme kegagalan/kerusakan dalam kaitannya dengan struktur metalurgi yang terjadi. Dalam studi ini sejumlah pengujian telah dilakukan meliputi pemeriksaan visual dan makroskopik, pengujian metalografi dan kekerasan, serta analisa SEM (*scanning electron microscope*) yang dilengkapi dengan EDS (*energy dispersive spectroscopy*). Hasil studi yang diperoleh menunjukkan bahwa jenis kegagalan yang terjadi pada alat penukar kalor kompresor adalah korosi antar-butir akibat peristiwa sensitisasi yang terjadi. Disamping itu, kerusakan yang terjadi kemungkinan juga dipengaruhi oleh cacat las yang terbentuk yaitu berupa porositas gas.

**Kata Kunci:** Alat penukar kalor kompresor, investigasi kerusakan, korosi antar-butir, paduan aluminium tanpa pengerasan perlakuan panas, sensitisasi, cacat las *(*porositas*)*

## Abstract

*This study was carried out on a compressor heat exchanger (after-cooler) which leaked in the welded joint of a component made of non-heat-treatable aluminum alloys. The purpose of this study is to determine the type, cause, and mechanism of failure/damage in relation to the metallurgical structure that occurs. In this study, several tests were carried out including visual and macroscopic examinations, metallographic and hardness testing, and SEM (scanning electron microscope) analysis equipped with EDS (energy dispersive spectroscopy). The results show that the type of failure that occurs in the compressor after-cooler is intergranular corrosion due to the sensitization that occurred in the microstructure. In addition, the damage that occurs may also be influenced by the weld defect in the form of gas porosity.*

***Keywords:*** *Compressor heat exchanger (after-cooler), damage investigation, intergranular corrosion, non-heat treatable aluminum alloys, sensitization, welding defect (porosity)*

## 1. INTRODUCTION

As compressor heat exchanger (after-cooler) components are generally made of medium-strength aluminum alloys such as the AA5xxx and AA3xxx. Besides that, these aluminum alloys are also widely used for components in car air conditioners and other structural applications because they have a good combination of strength and formability[1],[2]. Such properties can be achieved by the mechanism of solid solution hardening and enhanced by deformation due to the high strain hardening behavior [3],[4]. The AA5xxx is the aluminum alloys in which magnesium (Mg) used as the principal alloying element, while the AA3xxx is the aluminum alloys in which manganese (Mn) used as the principal alloying element [5]. For further improvement in properties such as good weldability and high corrosion resistance, the alloys are also added with other solute elements in small amounts and/or modified by processing routes [6],[7]. Although by addition of other solute elements may have produced different types of intermetallic phases and could increase

the strength of the alloys, however, they may lead to a higher susceptibility to localized corrosion [8],[9]. Due to the limited solubility of Mg or Mn in the aluminum matrix in both alloys at lower temperatures, the alloys become supersaturated and the excess alloying atoms together with other solute atoms would precipitate and form various intermetallic phases, preferentially at grain boundaries [1]-[2],[9]. Under certain conditions, either during fabrication/welding or in extended service at high temperatures, the solubility of principal alloying elements in the aluminum matrix will further decrease because they may interact with the existing intermetallic phases and form other new precipitates. This condition may result in a different concentration between the grains and the grain boundaries and makes the alloys sensitized and susceptible to intergranular corrosion, stress corrosion, or pitting corrosion [2],[8]–[9]. Many recently published works stated that the type of intermetallic phases that may play an important role in the intergranular corrosion and other localized corrosion on the non-heat-treatable aluminum alloys include $Mg_2Si$, $Al_3Mg_5$, $Al_6$ (Mn, Fe), $Al_6$ Mn, etc [1]-[2],[8].

The failed compressor after-cooler that used in this study consists of two separated pressure chambers, one is used to cool the hot stream of pressurized air from the compressor and the second is used to cool the hot stream of compressor lubricating oil. From the design and manufacture datasheet, it was mentioned that the failed compressor after-cooler is made of non-heat-treatable aluminum alloys of AA5xxx and AA3xxx, and fabricated by brazing and welding. In this study, the effect of welding that may have led to sensitization and intergranular corrosion of the after-cooler component was also evaluated in relation to the service fluid and environmental condition that occurs during operation.

## 2. MATERIALS AND METHODS

The present work aims to study the damage mechanism that has caused a compressor after-cooler to leak. Figure 1 shows a leaked compressor after-cooler used in the present study. The after-cooler is equipped with two separated pressure chambers, namely compressor air cooler and compressor lubricating oil cooler. The operating data of the compressor after-cooler is as follows: duty of 897 BTU/min., and maximum working pressure of 150 psi. As indicated in Fig. 1, the leak is located at the oil cooler around the corroded area on the weld joint between the inlet header and the sidebar/parting sheet.

The design and construction of the failed after-cooler is a typical brazed aluminum plate-fin heat exchanger [10]. As seen in Figs. 1, 2, and 3, the after-cooler consists of a block (core) of alternating layers (passages) of corrugated fins. These corrugated fins consist of heat transfer fins to heat exchange the cooling air from the forced draft fan, and distributor fins to heat exchange the hot streams of pressurized air or compressor lubricating oil. The block is bounded by cap sheets at both sides, whereas all the layers that carrying the pressurized hot air or compressor hot lubricating oil are connected by headers with nozzles which are directly attached by welding on to the brazed core at the sidebars and parting sheets across the ports. From Fig.s 2 and 3, the header looks only joined using an external single fillet weld without any internal fillet weld. According to the ALPEMA [10]-[11], typical materials used for the construction of brazed aluminum plate-fin heat exchangers are non-heat -treatable aluminum alloys of AA3003 type for core matrix (fins, parting sheets, sidebars, and cap plate), and AA5083 type for header and nozzle.

As seen in Figs. 1 to 3, the after-cooler inlet nozzles are aimed to enter the pressurized hot air or compressor hot lubricating oil flow into the after-cooler, while the after-cooler outlet nozzles are aimed to remove the pressurized cold air or compressor cold lubricating oil flow out of the after-cooler. The pressurized hot air or compressor hot lubricating oil is collected in the port of inlet headers before being distributed through each passage containing distributor fins. On the way from the inlet header to the outlet header, the pressurized hot air or compressor hot lubricating oil flow within the passages containing distributor fins experiences heat loss due to heat exchange from the passages containing heat transfer fins. The extended surface of the heat transfer fins is cooled using ambient airflow driven by a forced draft fan.

A close-up view of the failed after-cooler shown in Fig. 4 reveals that the oil leak located on the linear crack that formed on the parting line of weld joint between inlet header and sidebar/parting sheet.

In this study, several specimens were prepared from the sectional parts of the failed after-cooler shown in Figures 2 and 3 for several laboratory examinations and analysis. Macroscopic examination on some damaged surface of the after-cooler was performed using a stereomicroscope. In addition, a metallographic examination was also performed using an optical microscope at various magnifications. The metallographic samples were mounted using epoxy and prepared by grinding, polishing, and

etching. The etchant applied was Keller solution [12]. A hardness survey was also carried out on the same samples for the metallographic examination using the Vickers hardness method at a load of 2 kg (HV2). Moreover, examination of some damaged surfaces of the after-cooler was also performed using SEM (scanning electron microscopy) to determine the damaged surface topography and the nature of the failure. The SEM was also equipped with an EDS (energy dispersive spectroscopy) analysis to detect the presence of any corrosion by-product.

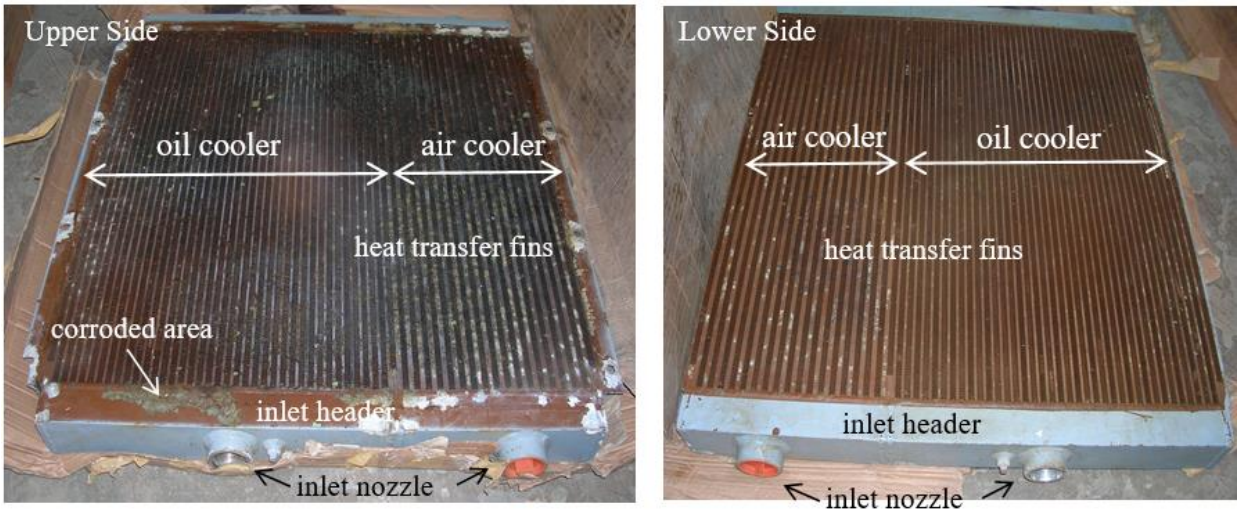


Figure 1. The leaked compressor after-cooler used in the present study, showing its upper side and lower side, respectively

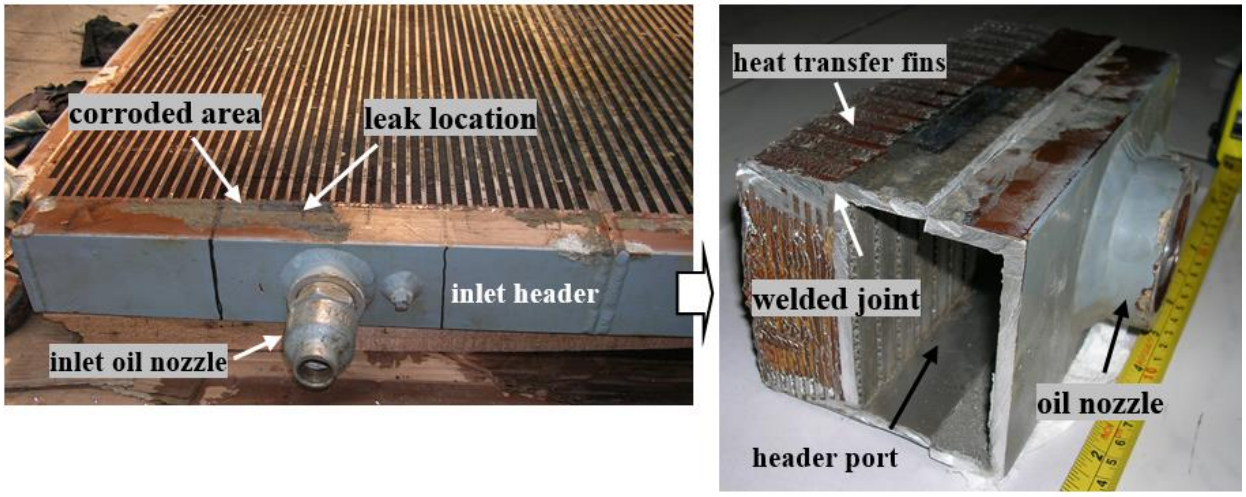


Figure 2. Cutting-off some parts of the compressor after-cooler around the leak location for samples preparation

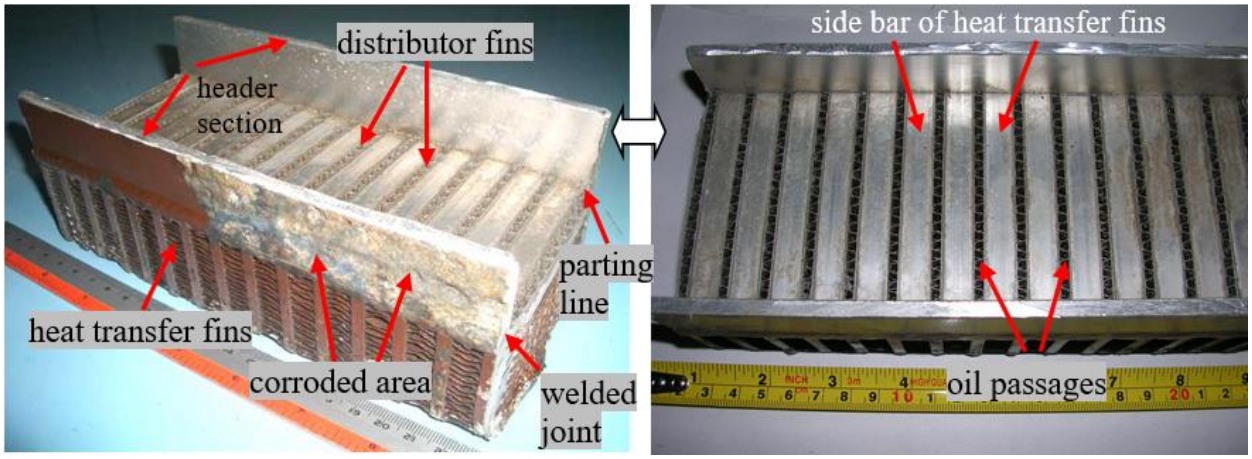


Figure 3. Close up view of the inside header port, showing several oil passages containing distributor fins and parting line of the weld joint between the header and sidebars/parting sheets

Figure 4. Close up view of the corroded surface around the weld joint of the leaked compressor after-cooler

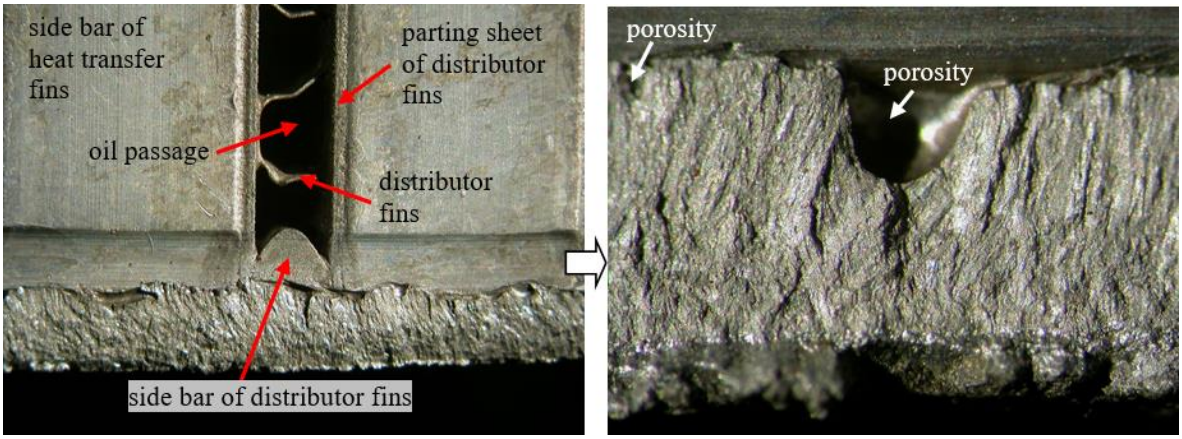

Figure 5. Fracture surface of the weld joint between header and sidebar/parting sheet

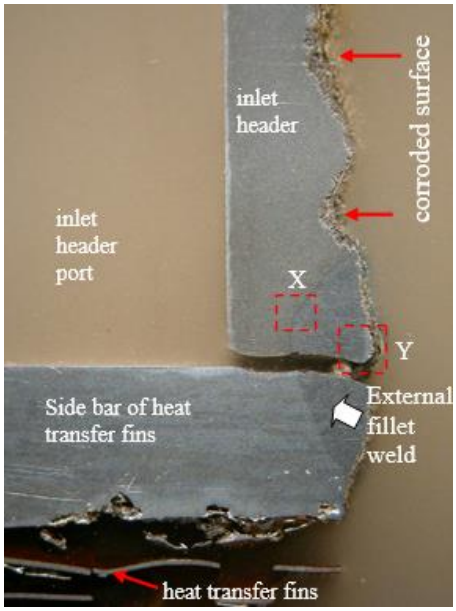

Figure 6. Cross section of a polished and etched specimen obtained from the leaked weld joint between header and sidebar/parting sheet

## 3. RESULTS AND DISCUSSIONS

### 3.1. Visual and Macroscopic Examination

The results of the macroscopic examination obtained from the leaked area on the weld joint between the inlet header and the sidebar/parting sheet of the compressor after-cooler (see Fig. 4) are presented in Fig. 5. It can be seen from Fig. 5 that most of the weld fracture surface contained several voids due to gas porosity. In addition, the corrosion seems to have entered into the weld fracture surface. Besides that, the application of one single fillet weld may have further reduced the load-carrying capacity of the weld joint

between the inlet header and the sidebar/parting sheet and therefore it was prone to cracking.

### 3.2. Metallographic Examination and Analysis

Figure 6 shows a cross-section of a polished and etched specimen obtained from the leaked weld joint between the inlet header and the sidebar of the after-cooler/oil cooler. The specimen shows a fracture line lied along the parting line between the header and the sidebar of heat transfer fins. The crack leading to the fracture was likely originated from the corroded weld surface. Microstructures obtained from the specimen shown in Fig. 6 are presented in Fig. 7 at different locations. In the weld joint of the header side shown in Fig. 7, the microstructures obtained are located around the WM (weld metal), HAZ (heat affected zone), and around the BM (base metal HAZ). The microstructure of weld metal generally shows a dendritic type, while the microstructure of the header material at its base metal shows typical wrought aluminum alloy microstructure containing fine particles of the intermetallic second phases [1],[2],[8]–[9]. Similarly, the microstructure obtained from the weld metal shown in Fig. 5 also apparently exhibits several large voids or porosity (see Fig. 8). This further confirms that the fillet weld between the inlet header and the sidebar/parting sheet of the compressor after-cooler contained some amount of weld defect. In addition, the microstructures are shown in Fig. 9 also exhibit the area with heavy damage of external corrosion. The corrosion damage on the weld metal surface in general shows typical interdendritic corrosion. This interdendritic corrosion may have been caused by sensitization that occurred on the weld metal due to formation of a number of intermetallic phases during welding process or in service at extended high-temperature exposure [1]-[2],[8]-[9].

Another specimen of metallographic examination was also obtained from the leaked weld joint between the inlet header and the parting sheet of distribution fins (see Fig. 9). The microstructures obtained are very much similar to those observed from the previous microstructures shown in Figs. 7 and 8. The fracture shown in Fig. 9 was most likely originated from the corroded weld surface that was heavily damaged by interdendritic corrosion and progressed into the internal port of the inlet header through the parting line between the header and the parting sheet of distributor fins. Similarly, the extended crack or fracture that occurred was most also likely influenced by some weld defect (porosities) that formed in the weld joint between the header and the parting sheet.

Details of the microstructure obtained from the corroded surface area of the inlet header are depicted in Fig. 10. It is seen that most of the header surface was severely affected by intergranular corrosion. Similar to the microstructures shown in Figs. 7, 8 and 9, this intergranular corrosion was most likely caused by sensitization due to the formation of some intermetallic phases at the grain boundaries [1]-[2],[8],[9].

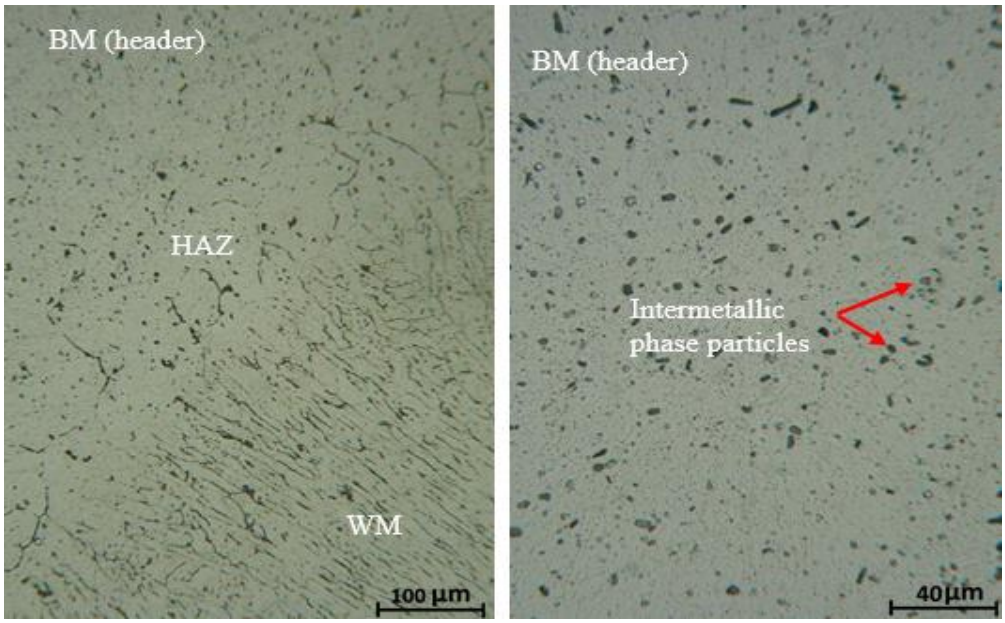


Figure 7. Microstructure obtained from the weld joint between header and sidebar/parting sheet at location X as indicated in Figure 6 (etched with Keller solution). Note BM is base metal, HAZ is heat-affected zone, and WM is weld metal

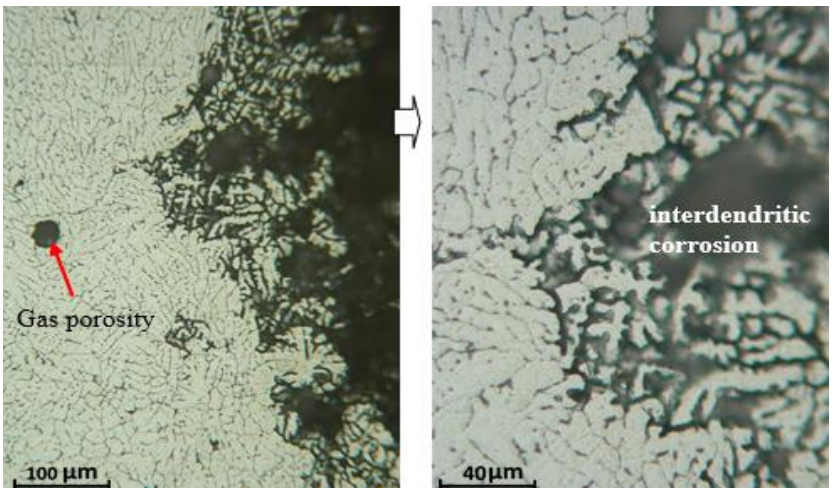

Figure 8. Microstructure obtained from the corroded weld metal of the header side at location Y as indicated in Figure 6 (etched with Keller solution)

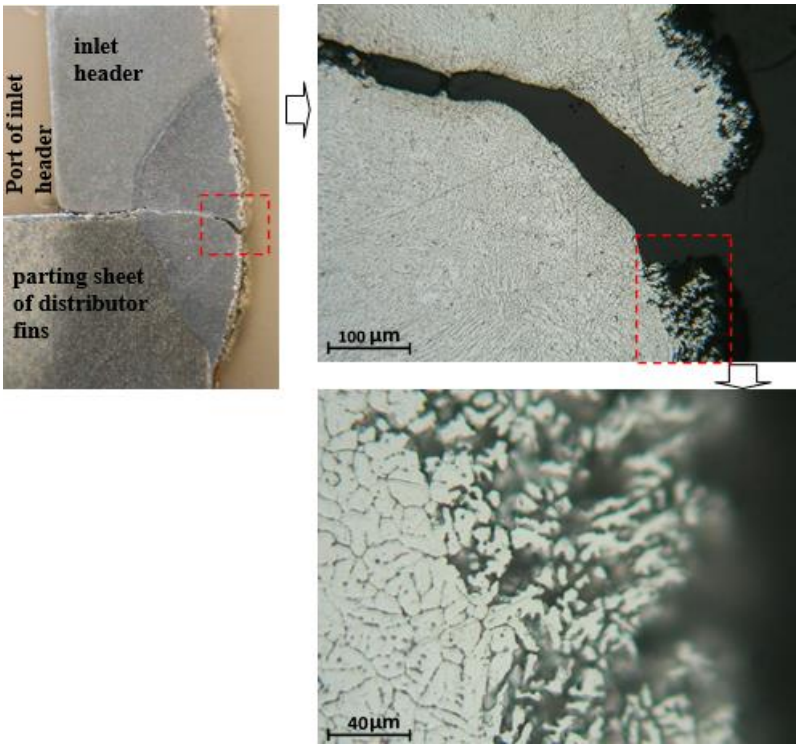

Figure 9. Microstructure obtained from the weld joint between header and parting sheet of distributor fins at location as indicated (etched with Keller solution)

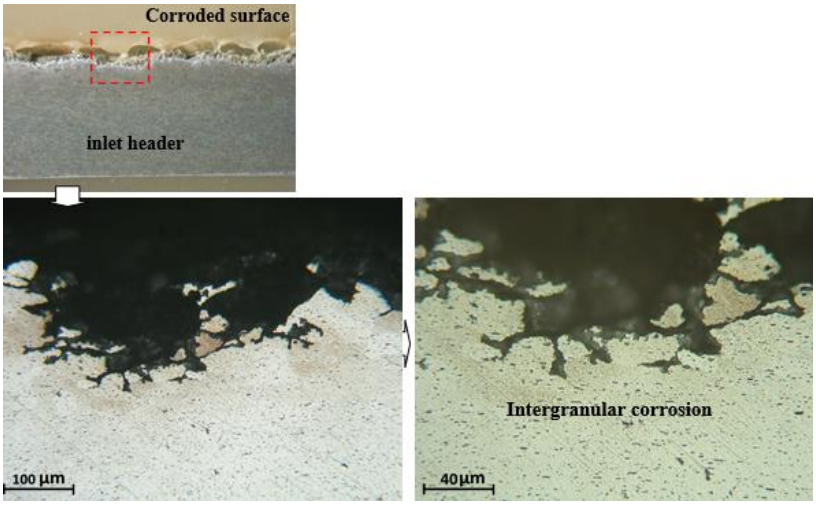

Figure 10. Microstructure obtained from the corroded area of the header surface at location as indicated (etched with Keller solution)

### 3.3. Hardness Test and Analysis

The hardness test was performed on the same metallographic specimen at different test locations (see Table 1). The results obtained show that the header base metal has hardness values in the range of 87.4-102 HV, i.e, slightly lower than its HAZ which is in the range of 94.6-105 HV. The hardness values of the weld metal are around 64.4 to 84.1 HV. Furthermore, the sidebar or parting sheet materials have hardness values in the range of 23.2-34.1 HV, i.e. lower than the hardness values of the sidebar or parting sheet material at its respective HAZ (24.4-59.3 HV). The higher hardness values obtained from the header material compared to the hardness values of the sidebar/parting sheet material indicated that both materials are made from different aluminum alloys. As mentioned in the ALPEMA standard [10]-[11], the header material is usually made of an aluminum alloy AA5083 type, whereas the sidebar/parting sheet material is usually made of an aluminum alloy AA3003 type. Both of these aluminum alloys belong to the non-heat-treatable alloys [5].

Table 1. Hardness survey (HV) obtained from various test locations of the metallographic sample shown in Figure 11

| Test Location | Hardness (HV) |
|---|---|
| 1 | 87.4 |
| 2 | 102.0 |
| 3 | 94.6 |
| 4 | 105.0 |
| 5 | 64.4 |
| 6 | 84.1 |
| 7 | 23.2 |
| 8 | 34.1 |
| 9 | 24.4 |
| 10 | 59.3 |

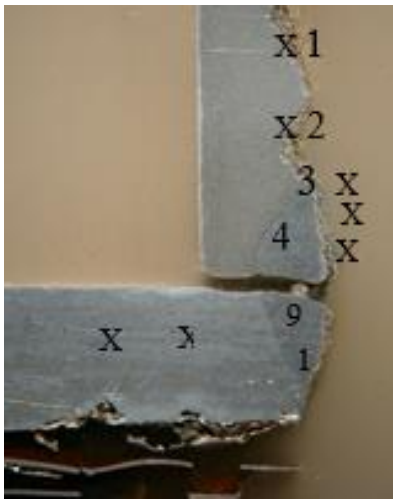


Figure 11. Various test locations for hardness survey

### 3.4. SEM Fractography and EDS Analysis

SEM fractography obtained from the fracture surface of the leaked after-cooler are presented in Fig. 12. The fractography obtained show the fracture surface of the weld joint between the header and the sidebar/parting sheet that contained many porosities. These porosities in some extent may have contributed to the crack or fracture formation. The crack seemed to initiate from the corroded surface of the weld joint and propagated into the weld defect (porosity) where the crack may have come to stop. However, the crack may have further continued to the nearest parting line between the header and the sidebar to complete the crack path. As seen clearly in Fig. 12, a large porosity appears to fill with some inclusions.

The EDS spectrum of elements obtained from the header fracture surface shown in Fig. 12 that experienced corrosion damage shows some major elements such as aluminum (Al), carbon (C), and oxygen (O) (see Fig. 13). The oxygen content obtained is much likely affected by the oxide formation due to corrosion (as corrosion product). Whereas the high carbon content found in the EDS spectrum may be influenced by some leakage of compressor hot lubricating oil that entered into the oil cooler. In addition to those elements, there are also other elements observed in the EDS spectrum such as magnesium (Mg), silicon (Si), sodium (Na), chloride (Cl) and calcium (Ca). Both elements of Mg and Si are the alloying elements of the aluminum alloy AA5xxx. The source of Na and Cl was most likely coming from the seawater and/or its moisture or maybe present from other aqueous environments. Figure 14 also shows the EDS spectrum of elements representing the corresponding composition of inclusion that formed inside a large porosity shown in Fig. 12. The inclusion is a typical aluminum oxide that likely formed from the filler metal used during welding.

Another result of the EDS analysis obtained from the corroded surface area located around the edge of the header and the weld fracture surface is presented in Fig. 15. Most of the result obtained indicated that oxygen (O) and carbon (C) along with aluminum (Al) and its alloying elements such as Si, Mg, Fe, Zn and some sulfur (S), chloride (Cl) and calcium (Ca) were detected on much of the corroded surface scale/corrosion product.

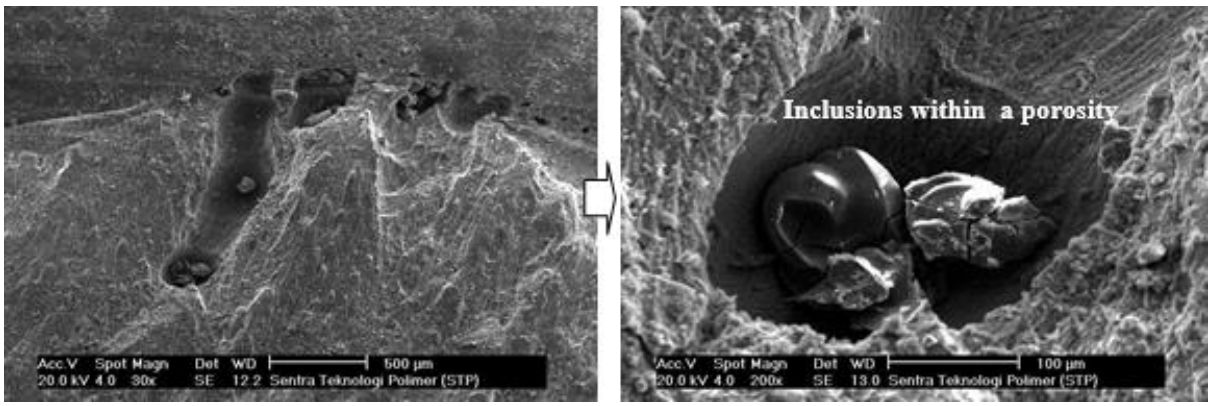


Figure 12. SEM micro fractography of the through fracture surface obtained from the leak area of the weld joint between the header and the sidebar/parting sheet, showing some inclusions within the weld defect

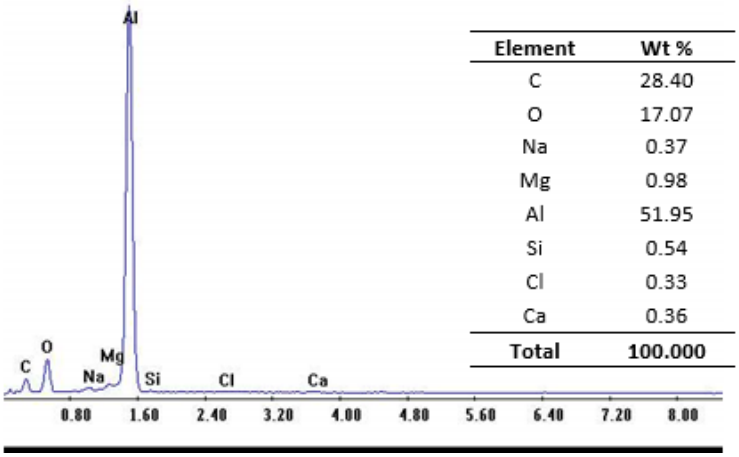


| Element | Wt % |
|---|---|
| C | 28.40 |
| O | 17.07 |
| Na | 0.37 |
| Mg | 0.98 |
| Al | 51.95 |
| Si | 0.54 |
| Cl | 0.33 |
| Ca | 0.36 |
| **Total** | **100.000** |

Figure 13. EDS spectrum of elements obtained from the header fracture surface shown in Fig. 12

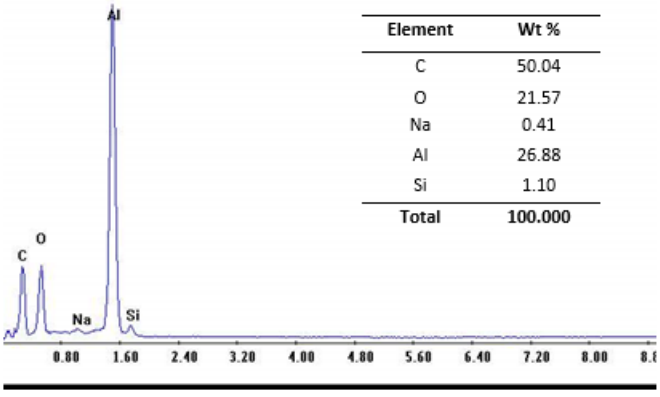


| Element | Wt % |
|---|---|
| C | 50.04 |
| O | 21.57 |
| Na | 0.41 |
| Al | 26.88 |
| Si | 1.10 |
| **Total** | **100.000** |

Figure 14. EDS spectrum of elements obtained from the inclusion formed in the weld defect (porosity) shown in Fig. 12

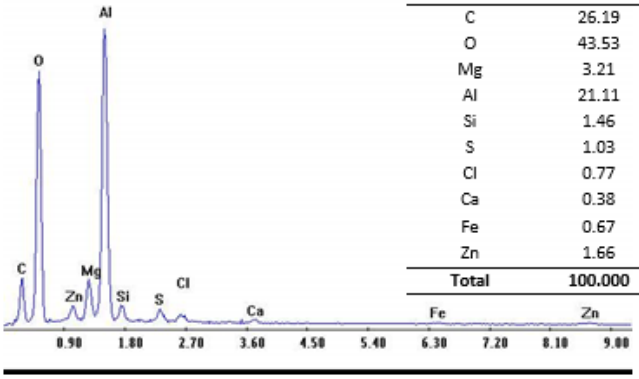


| Element | Wt % |
|---|---|
| C | 26.19 |
| O | 43.53 |
| Mg | 3.21 |
| Al | 21.11 |
| Si | 1.46 |
| S | 1.03 |
| Cl | 0.77 |
| Ca | 0.38 |
| Fe | 0.67 |
| Zn | 1.66 |
| **Total** | **100.000** |

Figure 15. EDS spectrum of elements obtained from the corroded header surface shown in Fig. 10

Based on the test results obtained from the EDS analysis, metallographic examination and hardness test, the material used for the header, sidebar, and parting sheet of the failed after-cooler are typical of wrought aluminum alloys. Some difference in hardness values observed on the header material in comparison with the sidebar and the parting sheet material is probably influenced by the difference in the chemical composition of the material. The header material is likely made of aluminum alloy AA5xxx series, while the sidebar/parting sheet material is probably made of aluminum alloy AA3xxx series. These two aluminum alloys belong to the non-heat-treatable alloys which are well known to have good properties for brazing and welding [6],[10]-[11].

The weld joint failure of the after-cooler in the present study was most likely caused by the combination of external corrosion (intergranular/interdendritic corrosion) and some welding defects (porosity) formed at the parting joint between the header and the sidebar/parting sheet of the corrugated fins. This may have led the compressor after-cooler to leak. The crack propagation would be accelerated in combination with the external corrosion that occurred on the weld joint surface that may have significantly reduced the effectiveness of the weld joint area. The external corrosion would have resulted from the high Cl and/or S levels obtained on the most corroded/fracture surfaces of the failed after-cooler (see Figs. 13 and 15). Chloride is the most important halide ion that has the greatest effect in accelerating attack in most aluminum alloys [3]. The source of this chloride could be coming from the natural constituent of the marine environment or other environments. The external corrosion observed in the present study is a typical intergranular or interdendritic corrosion (see Figs. 8 to 10). Some aluminum alloys that contain an appreciable amount of soluble alloying elements, primarily magnesium, silicon, copper, and zinc, are known susceptible to intergranular/ interdendritic corrosion [1], [2], [8]–[9].

The aforementioned mechanism of external corrosion and weld defect would cause a lowering of the load-carrying capacity of the weld joint and hence initiated failure of the weld joint during operation. Crack propagation may have also been accelerated by cyclic stresses induced by the internal pressure of the oil stream/flow or by flow-induced vibration of the after-cooler during operation.

In addition to the external corrosion and weld defect, the premature failure of the compressor after-cooler was also likely caused by insufficient weld design as the weld joint between the header and the sidebar/parting sheet of the after-cooler only used a single fillet weld. The application of another fillet weld on the inside parting line between header and sidebar/parting sheet may improve the load-carrying capacity of the weld joint structure, and hence it may increase the operating life of the after-cooler significantly.

## 4. CONCLUSIONS

The results of the EDS (energy dispersive spectroscopy) analysis, metallographic examination, and hardness test of the material used for both the header and the sidebar/parting sheet of the corrugated fins are likely according to the material specification of the non-heat-treatable wrought aluminum alloys of AA5xxx and AA3xxx series, respectively.

According to the fracture morphology and mode of failure, the leaked after-cooler under investigation had experienced a combination effect of the external corrosion and welding defect (porosities). Most of the external corrosion was concentrated on some particular area of the header/weld joint surface where the leak was found. The external corrosion was a typical interdendritic/intergranular corrosion and very much likely caused by some aqueous environment containing corrosive agents such as Cl, Na, and/or S.

The most possible source of Cl and/or Na content was the marine environment or from other environments. Sulfur (S) as being other corroding agents towards the acceleration of interdendritic/intergranular corrosion of the header/weld joint was also found in the corroded area. The source of S that had only contaminated some particular area of the header/weld joint surface of the failed after-cooler may be coming from the compressor hot lubricating oil.

## ACKNOWLEDGEMENT

The author wishes to express his gratitude to the Head and Members of the Department of Mechanical Engineering, Faculty of Industrial Technology of the National Institute of Science and Technology (ISTN) for their support and encouragement in publishing this work.

## REFERENCES


[1] M. Yoshino, S. Iwao, M. Edo and H. Chiba, "Mechanism of Intergranular corrosion of brazed Al-Mn-Cu alloys with various Si content," *Mater. Trans.*, vol. 58, no. 5, pp. 768–775, 2017. Doi : 10.2320/matertrans.L-M2017808.

[2] W. Wei, "Study of sensitization in AA 5083 aluminum alloy," University of Manchester, 2017.

[3] O. M. Alyousif and R. Nishimura, "The effect of applied stress on environment-induced cracking of aluminum alloy 5052-H3 in 0.5 M NaCl solution," *Int. J. Corros.*, vol. 8, pp. 1–5, 2012. Doi : 10.1155/2012/894875

[4] Y. Oya, Y. Kojima and N. Hara, "Influence of silicon on intergranular corrosion for aluminum alloys," *Mater. Trans.*, vol. 54, no. 7, pp. 1200–1208, 2013. Doi : 10.2320/matertrans.M2013048.

[5] J. R. Davis, "Aluminum and aluminum alloys," *ASM International*, pp. 351–416, 2001.

[6] L. Radovic, M. Bucko and M. Miladinov, "Corrosion behavior of TIG welded AlMg6Mn alloy," *Sci. Tech. Rev.*, vol. 66, no. 2, pp. 10–17, 2016. Doi :10.5937/STR1602010R.

[7] Y. Kailin, S. Hai wang, R. Yu Chen, T. Sheng Hsieh, L. Tsai, and C. Chin Chiang, "The effect of heat treatment on the sensitized corrosion of the 5383-H116 Al-Mg alloy," *Materials (Basel).*, vol. 10, no. 3, pp. 1–9, 2017. Doi: 10.3390/ma10030275

[8] V. S. Sinyavskii, V. V. Ulanova and V. D. Kalinin, "On the mechanism of intergranular corrosion of aluminum alloys," *J. Prot. Met.*, vol. 40, no. 5, pp. 481–490, 2004. Doi : 10.1023/B:PROM.0000043067.38199.95

[9] S. Kumari, S. Wenner, J.C. Walmsley, O. Lunder, and K. Nisancioglu, "Progress in understanding initiation of intergranular corrosion on AA 6005 aluminum alloy with low copper content," *J. Electrochem. Soc.*, vol. 166, no. 11, pp. C3114–C3123, 2019.

[10] *The standard of the brazed aluminum plate-fin heat exchanger manufacturers association (ALPEMA)*, Second. 2000.

[11] J. R. Thome, *Heat Transfer Engineering*, Third. The new 3rd edition of the ALPEMA plate-fin heat exchanger standards, 2010.

[12] M. Warmuzek, "Metallographic techniques for aluminum and its alloys," *Metallography and Microstructures, ASM Handbook*, pp. 711–751, 2004.

Metalurgi (2021) 1: 17 - 24

METALURGI
Majalah Ilmu dan Teknologi
p-ISSN 0126-3188 | e-ISSN 2443-3926
www.ejurnalmaterialmetalurgi.com

# CALCIUM CARBONATE DEPOSITION ON Ti-6Al-6Mo

**Made Subekti Dwijaya[a,*], Muhammad Satrio Utomo[a], Syafira Ajeng Ramadhanty[b], Fendy Rokhmanto[a], Ibrahim Purawiardi[a], Galih Senopati[a], Aprilia Erryani[a]**

[a]Research Center for Metallurgy and Materials, Indonesian Institute of Sciences
Gedung 470, Kawasan PUSPIPTEK, Tangerang Selatan, Indonesia 15343
[b]Sumbawa University of Technology
West Nusa Tenggara, Indonesia
*E-mail: made006@lipi.go.id

*Masuk tanggal : 10-03-2021, revisi tanggal : 12-04-2021, diterima untuk diterbitkan tanggal 30-04-2021*

## Abstrak

Oseointegrasi adalah salah satu properti penting dalam pengembangan material untuk aplikasi implan tulang. Meskipun material logam biokompatibel seperti paduan titanium sudah memiliki properti biokompatibel bawaan yang sudah mencukupi sebagai material implan tulang, sifat oseointegrasi masih dapat ditingkatkan dengan pelapisan biokeramik. Kalsium karbonat ($CaCO_3$) dan hidroksiapatit adalah dua biokeramik utama pada tulang yang dapat dimanfaatkan untuk meningkatkan sifat oseointegrasi pada material implan. Tantangan saat ini pada pelapisan biokeramik pada material implan adalah memperoleh metode pelapisan yang mudah diterapkan dan ekonomis untuk selanjutnya diterapkan di industri. Pada penelitian ini dilakukan sebuah metode yang sederhana untuk mendeposisi kalsium karbonat pada permukaan Ti-6Al-6Mo. Pada kegiatan ini digunakan dua larutan biomimetik yang sudah secara luas digunakan, yaitu PBS *(phosphate buffer saline)* dan SCS (*supersaturated calcification solution*) untuk membuat pembentukan kalsium karbonat pada permukaan Ti-6Al-6Mo. Pengamatan struktur mikro dan elemental dengan SEM (*scanning electron microscope*) – EDS (*energy dispersive spectroscopy*) menunjukkan keberadaan deposit kalsium karbonat pada permukaan Ti-6Al-6Mo. Lebih lanjut, analisa kristalografi dengan difraksi sinar-x (XRD) juga menguatkan keberadaan deposit kalsium karbonat pada permukaan Ti-6Al-6Mo. Metode yang diajukan juga diterapkan pada Ti murni (>95%) sebagai perbandingan dan diperoleh hasil yang serupa. Pengaruh durasi perendaman juga diamati dalam penelitian ini. Hasil dari imersi dengan durasi 7 dan 10 hari tidak menunjukkan perbedaan yang signifikan.

**Kata Kunci:** Kalsium karbonat, implan, larutan kalsifikasi lewat jenuh, Ti-6Al-6Mo

## Abstract

*Osseointegration is one of important property in development of implant materials for orthopedic applications. While biocompatible metallic materials such as titanium alloys should already have adequate biocompatibility properties as implant materials, their osseointegration property could be further improved by bioceramic coating. Calcium carbonate ($CaCO_3$) and hydroxyapatite are two major bioceramics in bones that can be utilized to improve the osseointegration property of metallic implant materials. Current challenge on bioceramic coating of metallic implant materials is to obtain coating method that is facile and economically feasible for implementation in the industry. The current activity proposes a simple and straightforward method to deposit calcium carbonate on Ti-6Al-6Mo. Two common biomimetic solutions were utilized in current activity PBS (phosphate buffer saline) and SCS (supersaturated calcification solution) to induce the calcium carbonate formation on the Ti-6Al-6Mo surface. Microstructural and elemental observations by SEM (scanning electron microscope) – EDS (energy dispersive spectroscopy) has shown the presence of calcium carbonate on the surface of the Ti-6Al-6Mo. Moreover, the crystallography analysis by XRD (x-ray diffraction) also confirmed the formation of calcium carbonate on the surface of Ti-6Al-6Mo. We also studied the proposed method on pure Ti (>95%) as comparison and similar outcomes were also observed. The effect on duration of immersion was also accounted in current setting. The outcomes of immersion duration for 7 and 10 days were not significantly different.*

***Keywords:*** *Calcium carbonate, implant, supersaturated calcification solution (SCS), Ti-6Al-6Mo*

## 1. INTRODUCTION

As osseointegration is an important property to be considered in orthopedic implant material development. Osseointegration is defined as the capability for an implant material to integrate structurally and functionally into the bone living tissue [1]. While metallic orthopedic implant materials such as titanium alloys, cobalt alloys, and steel alloys might provide sufficient biocompatibility properties, their osseointegration property could be improved.

One way to improve the osseointegration is by coating. The coating can be done by several methods such as biomimetic, electrodeposition, chemical or physical vapor deposition, and thermal spray or HVOF (high-velocity oxygen fuel) [2]. Among these methods, comprehensive studies have been focusing on the development of solution-based or biomimetic coating method of bioceramics onto various metallic implant materials including titanium alloys [3]. This coating method is preferable due to its ease of application which requires minimum instruments compared to other methods [4].

The application of bioactive coatings on the surface of a titanium implant is one of the most important ways to improve the surface properties [5]. Moreover, the degradation of the bioactive coatings could be associated with the increased osteoconductivity and enhanced bone-implant contact [6]. Both calcium phosphate and calcium carbonate are resorbable *in vivo.* Calcium carbonate was widely known in the field of bone regeneration due to its biodegradation and osteconductivity [7]. However, the effectiveness of bioactive coating have not yet been demonstrated as the coating cannot be achieved using spray coating and spin coating since the bioactive layer will be decomposed by heat treatment [8].

Here, we propose a study about calcium carbonate deposition onto Ti-6Al-6Mo by the biomimetic route. The Ti-6Al-6Mo has been developed in previous research as a candidate to substitute the current standard implant material, Ti-6Al-4V due to its content of vanadium which might be toxic and harmful if released [9]-[12]. It is expected that the deposition of calcium carbonate would improve its biocompatibility properties.

## 2. MATERIALS AND METHODS

### 2.1. Sample Preparation

There are two variants of the sample: pure Ti (>95%) and Ti-6Al-6Mo. The pure Ti sample was commercially obtained as a rod which was cut into a 5x5x2 mm plate using a wire cut. The Ti-6Al-6Mo was alloyed using an arc furnace and rolled into a plate which was then cut into a 5x5x2 mm plate using a wire cut. The mechanical and microstructural properties of the Ti-6Al-6Mo can be found in previous publications [9]-[12]. The Ti and Ti-6Al-6Mo plates were then cleaned using ethanol, acetone, and aquadest in an ultrasonic water bath for 15 minutes each. After that, the samples were air-dried at room temperature.

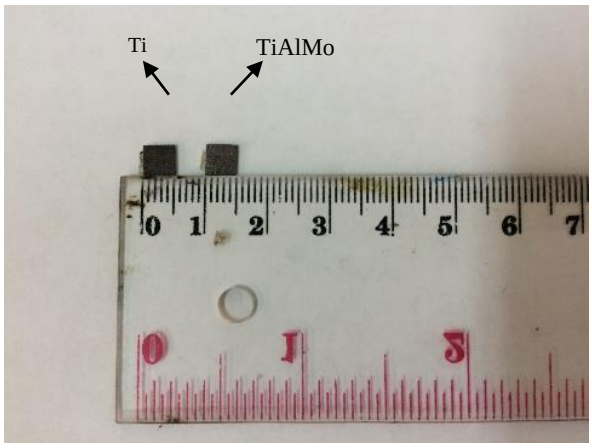


Figure 1. Titanium and Ti-6Al-6Mo plates

### 2.2. Solution Preparation

The PBS (phosphate buffered saline) and SCS (supersaturated aclcification solution) solutions are two among various synthetic chemical solutions that have similar ionic properties with human body fluid. They have been used in various research involving biomimetic methods and simulation tests on biocorrosion of implant materials in the human body. The PBS solution was prepared as standard stock in the laboratory. The PBS solution composition is shown in Table 1. Meanwhile, the SCS solution was prepared by mixing $CaCl_2.2H_2O$, $NaH_2PO_4.H_2O$, and $NaHCO_3$ in deionized water [13]. The SCS solution composition is shown in Table 2.

Table 1. PBS (phosphate buffered saline) solution composition

| Component | Concentration (mM) |
|---|---|
| NaCl | 137 |
| KCl | 2.67 |
| $Na_2HPO_4$ | 8.10 |
| $KH_2PO_4$ | 1.47 |
| $CaCl_2$ | 0.90 |

Table 2. SCS (supersaturated aclcification solution) solution composition

| Component | Concentration (mM) |
|---|---|
| $CaCl_2.2H_2O$ | 5.0 |
| $NaH_2PO_4.H_2O$ | 2.5 |
| $NaHCO_3$ | 1.5 |

### 2.3. PBS and SCS Immersion

Following sample and solution preparation, the pure Ti and Ti-6Al-6Mo plates were grouped depending on the solution and duration for immersion. Both pure Ti and Ti-6Al-6Mo plates were fully immersed in horizontal orientation. The immersion durations were varied for 7, 10, and 14 days in ambient temperature. The usual immersion time for the biomimetics method using SBF (simulated body fluids) is 7 days. By prolonging the duration of immersion to 10 and 14 days, the deposition of $CaCO_3$ preferably became thicker or covered the surface of the plates more evenly. The immersion solutions were replaced every two days to keep the ionic concentration stable. Table 3 shows the sample grouping with immersion solution and duration variations.

Table 3. Sample Ti and TiAlMo grouping

| Sample code | Immersion solution | Immersion duration (days) |
|---|---|---|
| Ti SCS7 | SCS | 7 |
| Ti SCS10 | SCS | 10 |
| Ti SCS14 | SCS | 14 |
| TiAlMo SCS7 | SCS | 7 |
| TiAlMo SCS10 | SCS | 10 |
| TiAlMo SCS14 | SCS | 14 |
| Ti PBS7 | PBS | 7 |
| Ti PBS10 | PBS | 10 |
| Ti PBS14 | PBS | 14 |
| TiAlMo PBS7 | PBS | 7 |
| TiAlMo PBS10 | PBS | 10 |
| TiAlMo PBS14 | PBS | 14 |

### 2.4. Cleaning and Drying

After immersion under specified duration, the pure Ti and Ti-6Al-6Mo were washed using distilled water and dried on a hotplate at 60 °C for an hour.

### 2.5. XRD and SEM Characterizations

All pure Ti and Ti-6Al-6Mo plates were immersed and dried before characterized using SEM-EDS (scanning electron microscope-energy dispersive spectroscopy) and XRD (x-ray diffraction). XRD characterization would provide information regarding elemental formation in the samples. XRD characterization was conducted at $2\theta$ = 20-120° using XRD Bruker with Cobalt *x-ray* source. The morphological and chemical composition of calcium carbonate deposition was observed using SEM coupled with EDS. The SEM instrument used was JEOL JSM-6390A model with 250X and 500X magnification. The samples were coated using gold sputtering for 20 seconds to prepare the surface conductivity for SEM investigations.

## 3. RESULTS AND DISCUSSIONS

Figures 1(a)-1(c) and 2(a)-2(c) presented the morphological of Ti and Ti-6Al-6Mo plates that were immersed in PBS (phosphate buffered saline).

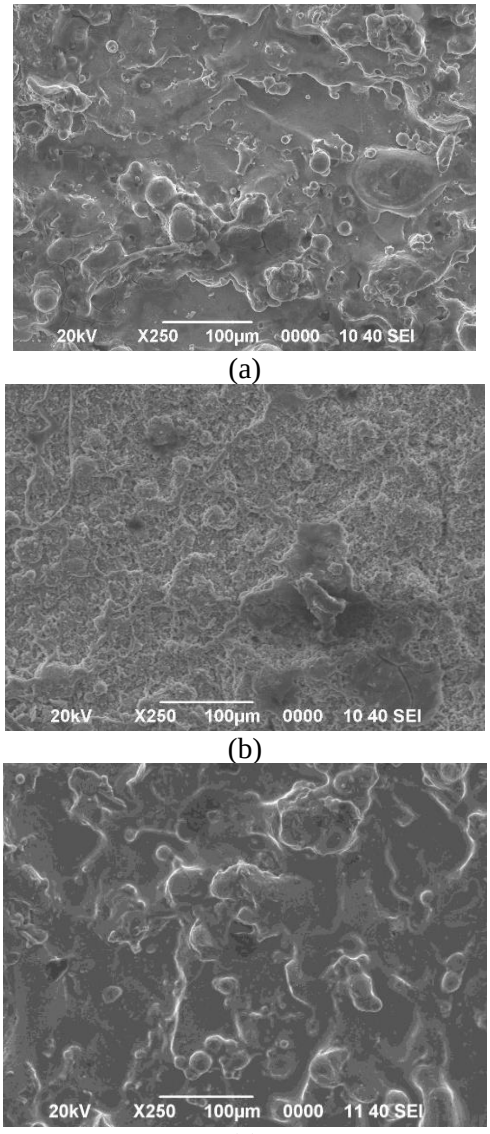


Figure 1. Surface morphological of (a) Ti PBS7, (b) Ti PBS10, and (c) Ti PBS14

The surface morphological examination of Dulbecco's PBS immersed Ti and Ti-6Al-6Mo plates show an uneven and rough surface with varied surface topography. The surface looks homogenous with no distinctive or visible deposition of calcium carbonate whether, on 7 (Ti PBS7 & TiAlMo PBS7), 10 (Ti PBS10 & TiAlMo PBS10), or 14 days (Ti PBS14 & TiAlMo PBS14) immersed plate.

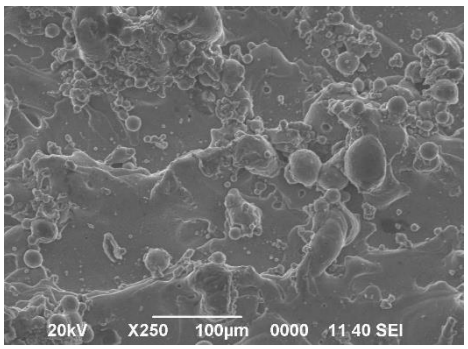


(a)

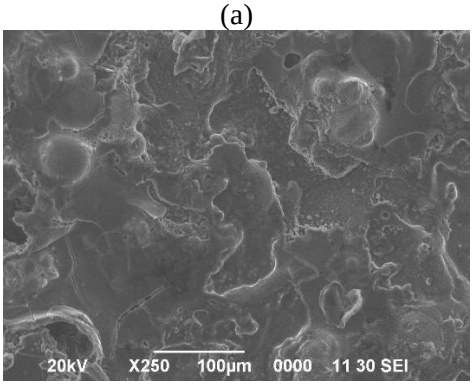


(b)

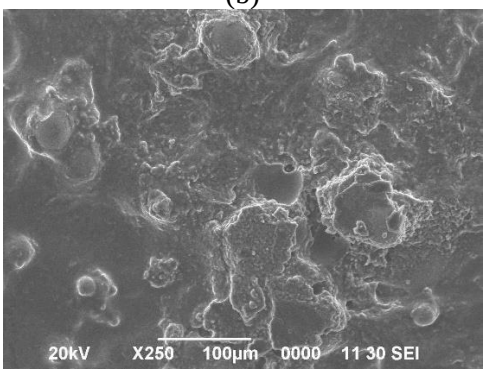


(c)

Figure 2. Surface morphological of (a) TiAlMo PBS7, (b) TiAlMo PBS10, and (c) TiAlMo PBS14

The surface morphological of SCS (supersaturated calcification solution) immersed Ti and Ti-6Al-6Mo plates were shown in Figs. 3(a)-3(c) and Figs. 4(a)-4(c). The surface morphological of SCS-immersed Ti and Ti-6Al-6Mo plates showed similar features to the PBS immersed one, which is uneven and rough. The difference with the PBS group was there is some whitish deposition of suspected calcium carbonate on the SCS immersed group. The suspected calcium carbonate deposit was not uniformly covered the surface and looked agglomerated, as shown in Figs. 3(a)-3(c) and Figs. 4(a)-4(c). All of the plate surfaces didn't have a good, uniform morphology as shown by the SEM (scanning electron microscope) results. This could be attributed to the wire cut process and no polishing treatment after cutting. The polishing process could increase the uniformity of the surface and reduce the extreme differences of the surface contour [14]. The extreme contour of the plate surfaces made it hard to characterized using AFM (atomic force microscope). The AFM probes couldn't generate the surface images due to the height of one part of the surface were too high while the other part was too low.

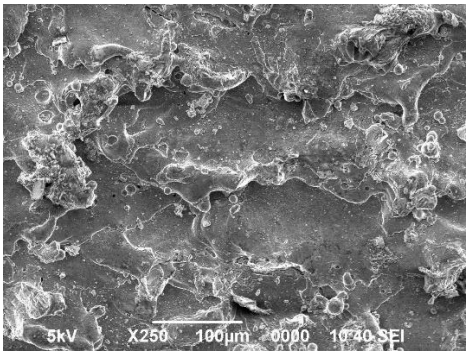


(a)

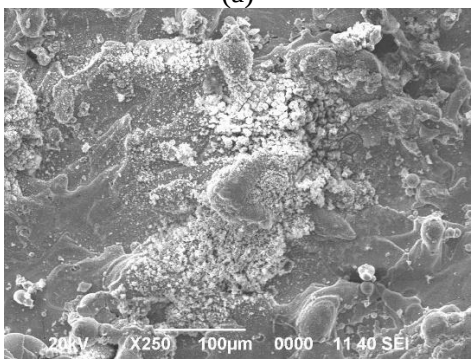


(b)

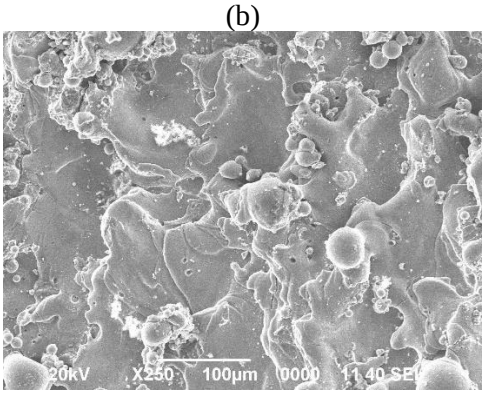


(c)

Figure 3. Surface morphological of (a) Ti SCS7, (b) Ti SCS10, and (c) Ti SCS14

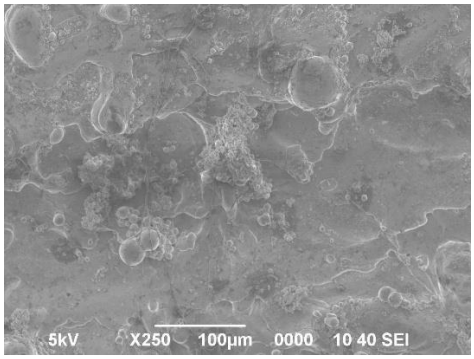


(a)

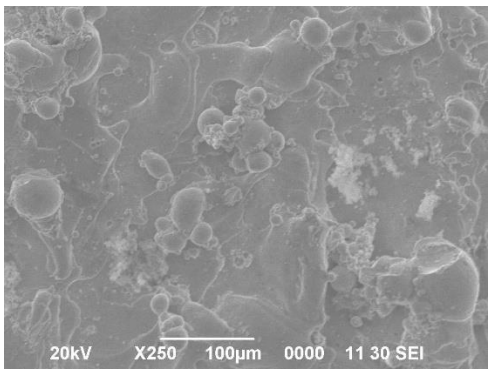


(b)

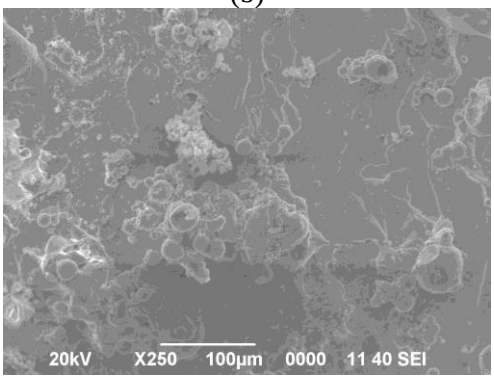


(c)

Figure 4. Surface morphological of (a) TiAlMo SCS7, (b) TiAlMo SCS10, and (c) TiAlMo SCS14

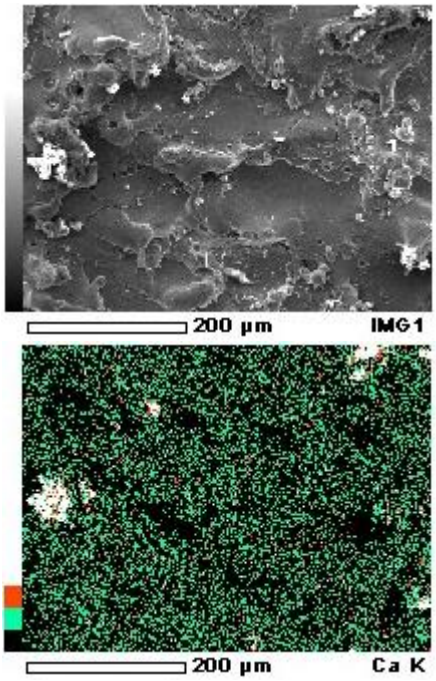


Figure 5. EDS mapping of TiSCS7 surface

The element mapping of Ti SCS7, Ti SCS10, and Ti SCS14 was shown in Figs. 5-7. The white color of EDS (energy dispersive spectroscopy) mapping results indicates the whitish compound on the plate surface as calcium, while the other color showed on the mapping results are indicating other elements. This could be an indication of calcium carbonate deposition was successfully deposited using the biomimetic route. The mapping also shows that the calcium was not uniformly covered the plate.

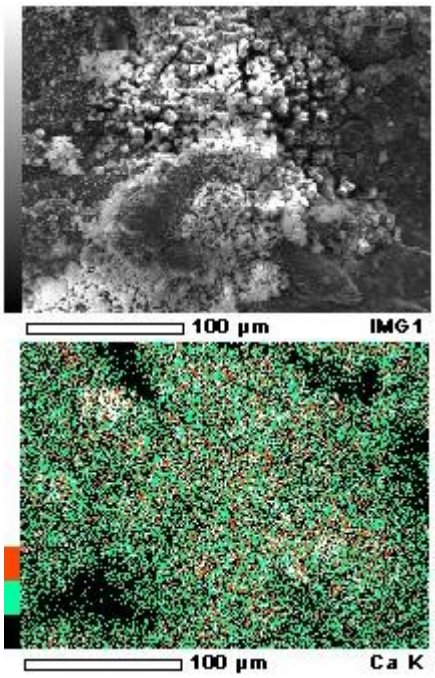


Figure 6. EDS mapping of TiSCS10 surface

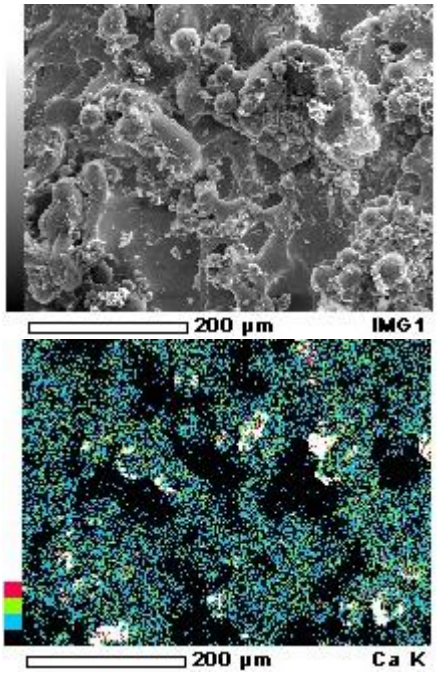


Figure 7. EDS mapping of TiSCS14 surface

Figures 8(a)-8(c) and 9(a)-9(c) show the XRD (x-ray diffraction) characterization results of the SCS immersed plate. Based on XRD results in Figure 8(a)-(c) it was confirmed that the calcium on the surface was calcium carbonate.

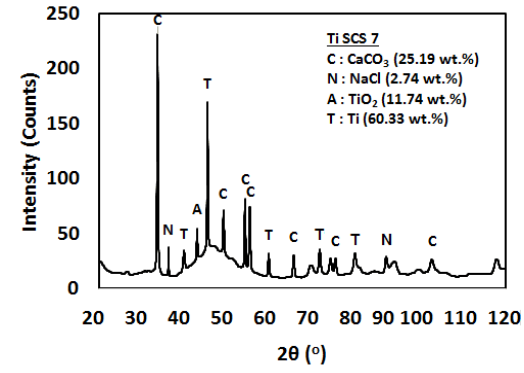


(a)

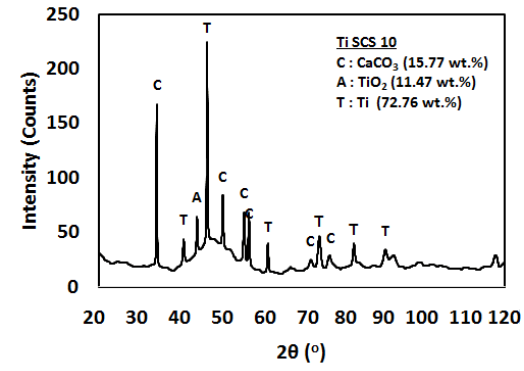


(b)

Figure 8. XRD plot of (a) TiSCS7 and (b) TiSCS10 immersed in SCS for 7 and 10 days

The Ti SCS7 was immersed for 7 days shows higher intensity than Ti SCS10 which was immersed for 10 days. This could be attributed due to the calcium carbonate on Ti SCS7 was more agglomerated than the calcium carbonate on Ti SCS10. The quantitative analysis of TiSCS7 and TiSCS10 shows a similar trend with the peak intensity. The TiSCS7 has 25.19 wt.% of $CaCO_3$ while TiSCS10 got 15.77 wt.%. This indicates the longer the immersion time doesn't always affect positively on $CaCO_3$ deposition process.

The Ti-6Al-6Mo plates which were immersed in SCS also indicated the calcium carbonate formation as shown in Figs. 9(a)-9(c). The intensity of the $CaCO_3$ XRD peak on the Ti-6Al-6Mo group increased a little along with the increasing duration of immersion. On the other hand, the quantitative analysis of the XRD shows conflicting results with the intensity of the peak. TiAlMoSCS7 has 33.58 wt% and TiAlMoSCS10 has 29.44 wt% of $CaCO_3$. This shows the higher intensity of the peak doesn't always go hand in hand with the quantity of the compounds. The thickness of $CaCO_3$ deposition on the 7$^{th}$, 10$^{th}$, and 14$^{th}$ day couldn't be determined whether using SEM or AFM. The AFM probe couldn't generate the image of the surface due to the extreme difference of the plate's surface contour.

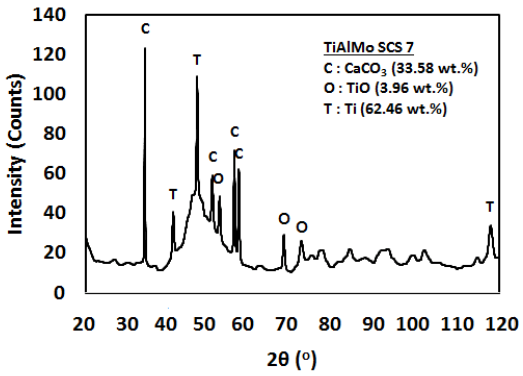


(a)

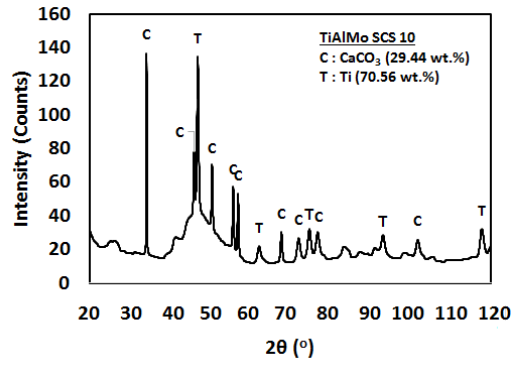


(b)

Figure 9. XRD plot of (a) TiAlMo SCS7 and (b) TiAlMo SCS10 immersed in SCS for 7 and 10 days

Molybdenum is selected due to its high capability as a beta phase stabilizer and more fair price compared to vanadium [9]. The previous experiment has shown that the Ti-Al-Mo exhibited both alpha and beta phases with hardness value ranges from 35 to 40 HRC in various thermomechanical conditions [9]. A previous study also suggested that solution-treated followed by air quenching promotes the hardness value of Ti-Al-Mo compared to water quenching due to higher alpha phase intensity compared to alpha' (α') and beta (β) phases [10].

The agglomerated and uneven deposit of calcium carbonate on the plate surface shows the deposition process was not fully complete. There is multiple causes which contributed to the incomplete deposition of calcium carbonate. First, it could be attributed to the lack of active ion on the plate surface. While using the same SCS formula, our findings differ from Ciobanu et al. This might be due to differences in the method. Here, the sample didn't expose to strong acid/base solution before immersion in SCS. In Ciobanu et al, the samples were alkaline treated using NaOH before treatment using SCS to form sodium titanate ($Na_2Ti_5O_{11}$) on the Ti-6Al-4V surface. In SCS, the sodium ions are released and exchanged with $H_3O$ ions forming Ti-OH groups.

Later, the Ca ions merge with the Ti-OH groups forming amorphous calcium titanate. Finally, the calcium titanate merges with phosphate ions forming amorphous calcium phosphate. Their result was validated by SEM-EDS and XRD [13].

Another titanium pre-treatment to improve the calcium carbonate deposition is via heat treatment to transform the surface into rutile which proved to be highly bioactive [15]. The method to transform the inert native oxide of titanium surface into rutile consist of oxidizing the titanium plate in a furnace at 500-800 °C with 1 hour holding time, followed by furnace cooling after the plate is cleaned in an ultrasonic bath. This process will affect the zeta potential of the titanium surface. When the Ti plate had a positively charged surface, it will selectively be adsorbing the negatively charged chloride ions onto the surface. As the chloride began to accumulate the surface charge has become negative, therefore the positively charged calcium ions are adsorbed on the surface to form a calcium carbonate layer [16].

The immersion solution temperature also held an important role in the deposition process of the biomimetic route. The temperature should be around 36-37 °C to mimic human body temperature [17].

The future experiments should include the in vitro test to confirm the bioactivity and biocompatibility of the calcium carbonate coating.

## 4. CONCLUSIONS

The deposition of calcium carbonate on Ti and TiAlMo plate using biomimetic route were performed. Micrograph and elemental observations show the presence of calcium carbonate on the surface of the Ti-6Al-6Mo immersed in SCS. The outcomes of immersion duration for 7 and 10 days were not significantly different. Similar outcomes were also observed on the pure Ti samples.

## ACKNOWLEDGEMENT

The authors would like to thank the LPDP 2020 Indonesian Ministry of Research and Technology/National Research and Innovation Agency for funding this research activity. The authors would also like to thank the Indonesian Institute of Sciences for providing materials, fabrication, and testing facilities used in the current setting.

## REFERENCES

[1] A. J. Rahyussalim, S. Supriadi, A. F. Marsetio, P. M. Pribadi, and B. Suharno, "The potential of carbonate apatite as an alternative bone substitute material," *Med. J. Indones.*, vol. 28, no. 1, pp. 92–97, 2019. Doi :10.13181/mji.v28i1.2681.

[2] E. B. Ansar, K. Ravikumar, S. S. Babu, F. B. Fernandez, M. Komath, and B. Basu, "Inducing apatite pre-layer on titanium surface through hydrothermal processing for osseointegration," *Mater. Sci. Eng. C*, vol. 105, pp. 110019(1)- 110019(7), 2019. Doi : 10.1016/j.msec.2019.110019.

[3] J. Faure, A. Balamurugan, H. Benhayoune, P. Torres, G. Balossier, and J. M. F. Ferreira, "Morphological and chemical characterisation of biomimetic bone like apatite formation on alkali treated Ti6Al4V titanium alloy," *Mater. Sci. Eng. C*, vol. 29, no. 4, pp. 1252–1257, 2009. Doi:10.1016/j.msec.2008.09.047.

[4] T. C. Lee, P. Koshy, H. Z. Abdullah, and M. I. Idris, "Precipitation of bone-like apatite on anodised titanium in simulated body fluid under UV irradiation," *Surf. Coat. Technol.*, vol. 301, pp. 20–28, 2016. Doi :10.1016/j.surfcoat.2015.11.010.

[5] Y. Liu, Y. Zhou, T. Jiang, Y. De Liang, Z. Zhang, and Y. N. Wang, "Evaluation of the osseointegration of dental implants coated with calcium carbonate: An animal study," *Int. J. Oral Sci.*, vol. 9, no. 3, pp. 133–138, 2017. Doi :10.1038/ijos.2017.13.

[6] H. Yamamoto, Y. Shibata, T. Tachikawa, and T. Miyazaki, "In vivo performance of two different hydroxyapatite coatings on titanium prepared by discharging in electrolytes," *J. Biomed. Mater. Res. - Part B Appl. Biomater.*, vol. 78, no. 1, pp. 211–214, 2006. Doi : 10.1002/jbm.b.30477.

[7] X. Li, X. Yang, X, Liu, W. He, Q. Huang, S. Li, and Q. Feng, "Calcium carbonate nanoparticles promote osteogenesis compared to adipogenesis in human bone-marrow mesenchymal stem cells," *Prog. Nat. Sci. Mater. Int.*, vol. 28, no. 5, pp. 598–608, 2018. Doi :10.1016/j.pnsc.2018.09.004.

[8] R. Shi, K. Hayashi, and K. Ishikawa, "Rapid osseointegration bestowed by carbonate apatite coating of rough titanium," *Adv. Mater. Interfaces*, vol. 7, no. 18, pp. 1–11, 2020. Doi :10.1002/admi.202000636.

[9] C. Sutowo, F. Rokhmanto, and G. Senopati, "Proses perlakuan termomekanis pada paduan α/β Ti-6Al-6Mo sebagai alternatif baru untuk aplikasi biomedis," *Widyariset*,

vol. 3, no. 1, pp. 47–54, 2017. Doi : 10.14203/widyariset.3.1.2017.47-54.
[10] I. Kartika, R. Werdaningsih, Alfirano, F. Rokhmanto, and Y. N. Thaha, "An investigation of α and α' phases intensity and hardness of Ti-6Al-6Mo implant alloy influenced by temperature of solution treatment and quenching media," *AIP Conf. Proc.*, vol. 2120, no. 1, pp. 050009(1)-050009(6), 2019. Doi:10.1063/1.5115685.
[11] F. Rokhmanto, I. N. G. P. Astawa, E. P. Utomo, D. P. Malau, R. I. Purawiardi, and J. Triwardono, "Characteristic the α phase in Ti-6Al-6Mo implant alloy after various pre-heating time of heavy hot rolling process," *Proc. 3RD Int. Semin. Metall. Mater. Explor. New Innov. Metall. Mater.*, vol. 2232, no. 1, pp. 070003(1)- 070003(6), 2020.
[12] G. Senopati, I. N. G. P. Astawa, and C. Sutowo, "Synthesis and characterization of Ti-6Al-6Mo prepared by arc melting process," *IOP Conf. Ser.: Mater. Sci.* Eng., vol. 202. no.1. pp. 012034(1)- 012034(6), 2017.
[13] G. Ciobanu, G. Carja, and O. Ciobanu, "Structural characterization of hydroxyapatite layer coatings on titanium supports," *Surface and Coatings Technology*, vol. 202, no. 11, pp. 2467–2470, 2008. Doi :10.1016/j.surfcoat.2007.11.038.
[14] J. C. M. Souza, M. B. Sordi, M. Kanazawa, S. Ravindran, B. Henriques, F. S. SIlva, C. Aparicio, and L. F. Cooper., "Nano-scale modification of titanium implant surfaces to enhance osseointegration," *Acta Biomater.*, vol. 94, pp. 112–131, 2019. Doi: 10.1016/j.actbio.2019.05.045.
[15] J. Forsgren, F. Svahn, T. Jarmar, and H. Engqvist, "Formation and adhesion of biomimetic hydroxyapatite deposited on titanium substrates," *Acta Biomater.*, vol. 3, no. 6, pp. 980–984, 2007. Doi: 10.1016/j.actbio.2007.03.006.
[16] D. K. Pattanayak, T. Kawai, T. Matsushita, H. Takadama, T. Nakamura, and T. Kokubo, "Effect of HCl concentrations on apatite-forming ability of NaOH-HCl- and heat-treated titanium metal," *J. Mater. Sci. Mater. Med.*, vol. 20, no. 12, pp. 2401–2411, 2009. Doi : 10.1007/s10856-009-3815-0.
[17] L. Jonášová, F. A. Müller, A. Helebrant, J. Strnad, and P. Greil, "Biomimetic apatite formation on chemically treated titanium," *Biomaterials*, vol. 25, no. 7–8, pp. 1187–1194, 2004. Doi : 10.1016/j.biomaterials.2003.08.009.

Metalurgi (2021) 1: 25 - 32

LIPI

METALURGI
Majalah Ilmu dan Teknologi
p-ISSN 0126-3188 | e-ISSN 2443-3926
www.ejurnalmaterialmetalurgi.com

# STUDY ON MICROSTRUCTURE AND MECHANICAL PROPERTIES OF Mg-Zn-Fe-Cu-Co AS HIGH ENTROPY ALLOYS FOR URETERAL IMPLANT

**Andi Mulya Ashari 1[a,*], Franciska Pramuji Lestari[b], Rahma Nisa Hakim[b], Inti Mulyati[b], Yudi Nugraha Thaha[b], Ika Kartika[b], Eddy Agus Basuki[a]**

[a] Departement of Metallurgical Engineering, Bandung Institute of Technology
Jl. Ganesha No. 10, Bandung, Indonesia 40132
[b] Research center for Metallurgy and Material, Indonesian Institute of Science
Gedung 470, Kawasan PUSPIPTEK Serpong, Tangerang Selatan, Indonesia 15343
*E-mail: andimulyaa94@gmail.com

*Masuk tanggal : 12-03-2021, revisi tanggal : 09-04-2021, diterima untuk diterbitkan tanggal 30-04-2021*

## Abstrak

Magnesium dan paduannya merupakan kandidat yang menjanjikan untuk bahan yang dapat terdegradasi dengan sifat biokompatibilitas yang baik. Paduan berdasarkan komposisi Mg-Zn-Fe-Cu-Co dirancang dengan metode equiatomic paduan entropi tinggi. Makalah ini membahas struktur mikro dan sifat mekanik dari paduan entropi tinggi. Serbuk Mg (60 µm), Zn (45 µm), Fe (10 µm), Cu (63 µm), dan Co (1 µm) dicampur dan digiling menggunakan shaker mill pada 700 rpm selama 30 menit di atmosfer udara pada temperatur kamar. Serbuk logam hasil gilingan yang dihasilkan dipadatkan dan disinter pada tekanan 300 MPa selama 180 detik dan 600 MPa selama 120 detik. Sintering dilakukan pada suhu 700 °C selama 2 jam dalam tungku vakum dengan laju pemanasan 5 °C / menit pada kondisi atmosfer argon dengan kemurnian tinggi. Pengaruh variasi kandungan magnesium terhadap struktur mikro dan sifat mekanik paduan Mg-Zn-Fe-Cu-Co dilakukan dengan SEM-EDS (*scanning electron microscope-energy dispersive spectroscopy*), XRD (*x-ray diffraction*) dan uji keras secara mikro. Paduannya pada dasarnya multifase dan kristal. Paduan 20Mg-20Zn-20Fe-20Cu-20Co terdiri dari fase HCP (*hexagonal closed packed*) dan fase kubik. Sifat fisik dan mekanik Mg-Zn-Fe-Cu-Co dipengaruhi oleh kandungan magnesium dalam paduan matriks. Adanya pori-pori mengindikasikan pemadatan dan proses sintering yang belum tuntas. Paduan memiliki kekerasan sedang antara 286,06 HV - 80,98 HV, sedangkan densitas paduan relatif sedang pada kisaran 3,057 g.cm$^{-3}$ sampai 1,71 g.cm$^{-3}$. Larutan padat dan penguatan presipitasi intermetalik diyakini sebagai mekanisme penguatan utama paduan. Disimpulkan bahwa entropi tinggi adalah metode yang menjanjikan untuk pemrosesan paduan Mg. Paduan dengan komposisi kimia 20Mg-20Zn-20Fe-20Cu-20Co memiliki sifat mekanik optimal yang memenuhi persyaratan minimum paduan entropi tinggi sebagai kandidat aplikasi implan ureter.

**Kata Kunci:** Logam mampu luruh, paduan entropi tinggi, metalurgi serbuk, paduan Mg-Zn-Fe-Cu-Co

## Abstract

*Magnesium and its alloys are promising candidates for degradable materials with good biocompatibility. Alloys based on Mg-Zn-Fe-Cu-Co compositions were designed using the equiatomic method of high entropy alloy. This paper discusses the microstructure and mechanical properties of these new high entropy alloys. Pure Magnesium (60 µm), Zinc (45 µm), Fe (10 µm), Cu (63 µm), and Co (1 µm) powder were mixed and milled using a shaker mill at 700 rpm for 30 minutes in an air atmosphere at room temperature. The resulting milled powders were compacted and sintered at 300 MPa for 180 s and 600 MPa for 120 s. Sintering was performed at 700 ºC for 2 hours in a tube vacuum furnace at a 5 °C/min heating rate under a high purity argon atmosphere. The effect of variations in magnesium content on the microstructure (SEM-EDS and XRD) and mechanical properties (microhardness tester) of the Mg-Zn-Fe-Cu-Co alloy were performed. The alloys were multiphase and crystalline. The 20Mg-20Zn-20Fe-20Cu-20Co alloy consisted of the HCP (hexagonal closed packed) phase and cubic phase. The physical and mechanical properties of Mg-Zn-Fe-Cu-Co were affected by the magnesium content in the matrix alloys. The presence of pores indicated uncomplete compaction and sintering process. The alloys have a medium hardness of between 286.06 HV - 80.98 HV, while the densities of the alloys were relatively moderate in the range of 3.057 g.cm$^{-3}$ to 1.71 g.cm$^{-3}$. Solid solution and intermetallic precipitation strengthening were believed the primary strengthening mechanics of the alloys. It is concluded that high entropy is a promising method for the processing of*

*Mg alloys. Alloy with the chemical composition of 20Mg-20Zn-20Fe-20Cu-20Co had optimal mechanical properties that meet the minimum requirements of high entropy alloys as a candidate for ureteral implant applications.*

***Keywords:*** *Biodegradable metal, high entropy alloy, powder metallurgy, Mg-Zn-Fe-Cu-Co alloy*

## 1. INTRODUCTION

Urinary tract stones (UTI) or kidney stones are a disease that affects the urinary system. Urinary tract infections are frightening and remain a major health burden of working age. In Indonesia, the prevalence of urinary tract infection patients per 1,000 Indonesian populations is 0.6% or 6% [1]. The ureteral lesion-induced bacterial infection, hydronephrosis, urinary cysts, and other urinary system complications, that affected the patient's life quality [2]. These diseases bring tremendous physical pain and heavy economic burden to a patient [3]-[4]. After surgery, the ureteral lesion healed with a ureteral stent, that placed in the urinary tract to keep urine flowing smoothly and prevent ureteral stenosis [2],[5]. However, the ureteral stent is an extraneous body for a sufferer, there have been many problems surrounding the use of ureteral stent, as well as stent fractures, encrustations establishment, urethral re-formations, and obstructions. The good ureteral stent has the following advantages: (1) good mechanical and drainage properties; (2) good biocompatibility; (3) X-ray and B-ultrasound radiopaque should be performed regularly after stent implantations [6]. Usually, a conventional ureteral stent is made by the polymer, which is cheap and well-tolerated by the sufferer but was prone and weak, that is not ideal for drainage and support in the ureter [2],[6]. Several studies have reported the use of biodegradable polymers for urethral stents, such as PLA (polylactic acid) [6], PGA (polyglycolide) [7], PCL (polycaprolactone) [2], Poly(L-lactide-co-ε-caprolactone) (PCLC) [8], and their copolymers. In contrast, biodegradable metal stents are of increasing interest in recent times because the mechanical properties of metals are inherently better than polymers and more desirable for stent expansion. The metallic stent is generally applied to treat cardiovascular disease, diseases of the bile duct and digestive tract in 1972 [6]-[5]. Magnesium and its alloys are promising candidates for degradable materials with high strength, low modulus of elasticity, and good biocompatibility [2],[4]-[5],[9]. So far, there have been a few studies on the use of biodegradable metal ureteral stents. In 2017, Zhang [2],[10]-[11] demonstrated that pure Mg, Mg-6Zn (Mass %), and ZK60 alloy have no obvious adverse effects on rat bladders and ZK60 alloy has good mechanical properties, with a uniform elongation of 10-30% and an ultimate tensile strength of 200-400 MPa, making it suitable for use as an implant material. A more recent study by Tie et. al., [5][12] demonstrated pure Mg, Mg-Y, AZ30, and Mg-Zn-Sr alloys have the potential alloys for urological applications.

Alloys are one of the most effective ways to improve the mechanical properties of metals [9],[13]-[16]. As we all know, solid solution strengthening and second phase strengthening are the two main methods to improve the mechanical properties of magnesium alloys [17]-[18]. In 2004, the two research groups respectively released the alloy development strategy of equal atomic ratio and high mixing entropy. They found that high-entropy alloys have a simple microstructure with less than 3 phases, and a cubic solution is the main phase [19]-[20]. Other researchers have studied the mechanical properties of high-entropy alloys [17],[19],[21]. In recent years, extensive and in-depth research has been conducted on the mechanical properties of high-entropy alloys. The composition of high-entropy alloys is mainly concentrated on Fe, Co, Cr, Ni, Ti, V, Cu, and Al [19]. However, there are a few reports on other ingredients such as magnesium, and zinc. The mentioned high entropy alloys usually attain excessive hardness and strength. So it's essential to study Mg-containing high entropy alloys. 20Mg-20Zn-20Fe-20Cu-20Co, 50Mg-25Zn-24Fe-0.5Cu-0.5Co, 70Mg-25Zn-4Fe-0.5Cu-0.5Co, 90Mg-5Zn-4Fe-0.5Cu-0.5Co, and pure Mg had been designed to examine the microstructure and mechanical properties of Mg-containing high entropy alloys in this paper.

## 2. MATERIALS AND METHODS

### 2.1. Samples Preparation

Pure elements of Magnesium (60 μm), Zinc (45 μm), Fe (10 μm), Cu (63 μm), and Co (1 μm) powder were weighted on a digital weighing balance in a normal atmosphere, at room temperature. 20Mg-20Zn-20Fe-20Cu-20Co, 50Mg-25Zn-24Fe-0.5Cu-0.5Co, 70Mg-25Zn-4Fe-0.5Cu-0.5Co, 90Mg-5Zn-4Fe-0.5Cu-0.5Co and pure Mg powder mixtures were filled in an alumina jar and mixed using shaker mill machine without ball at 700 rpm for 30 minutes [22]. The mixed powder was then compacted at 300 MPa for 180s and 600 MPa for 120 s under

normal atmospheric, at room temperature. The as-compacted samples were sintered at 700 °C for 2 hours in a tube furnace at 5 °C/min purged with a high purity argon atmosphere during sintering and cooling.

### 2.2. Test Methods

High entropy alloys have several parameters such as $\Delta S_{mix}$, $\Delta H_{mix}$, $\Delta G_{mix}$ ($\Omega$), and atomic size ($\delta$). Following Boltzmann's theory [19]. the mixing entropy for a five-element regular solution is given as:

$$\Delta S_{mix} = -R \sum_{i=1}^{n} C_i \ln C_i \text{ [19][21]} \qquad (1)$$

where $C_i$ is mole percent of a component, and R (8.314 J $K^{-1}$ $mol^{-1}$) is gas constanta. The mixing enthalpy alloy ($\Delta$Hmix) must be between -11.6 and 3.2 kJ / mol [18],[21], to be calculated using the derivative formula in equation 2 of Miedema's macroscopic model [23];

$$\Delta H_{mix} = \sum C_i C_j H_{ij} \text{ [21]} \qquad (2)$$

$\Delta H_{ij}$ is the binary enthalpy of the formation of elements i and j. The next criterion is the atomic radius value ($\delta$), stating that the phases which contain mostly solid and intermetallic solutions are formed at values lower than (<) 6.6%, and at values lower than 4% only solid solutions are formed [18]. To calculate the value of $\delta$, this equation 3 is used;

$$\delta = 100 \sqrt{\sum_{i=1}^{n} C_i \left(1 - \frac{r_i}{r}\right)^2} \text{ [21]} \qquad (3)$$

$C_i$ and $r_i$ are the compositions and the atomic radii of elements, i and r are the average atomic radii. Other thermodynamic parameters for predicting the formation of solid solutions are as follows equation 4;

$$\Omega = \frac{Tm\Delta S_{mix}}{\Delta H_{mix}} \text{ [21]} \qquad (4)$$

If $\Omega$> 1.1 and $\delta$ <3.6%, only a solid solution is formed. If 1.1 <$\Omega$ <10 and 3.6% <$\delta$ <6.6%, only solid solutions and intermetallic compounds are formed, and if $\Omega$ > 10 only solid solutions are formed.

The densities and hardness of alloy samples were tested by Archimedes principle according to ASTM B962-17 standard and microhardness Vickers tester. The relative density of respective samples was then calculated by dividing apparent density by theoretical density of the corresponding samples as obtained from the rule of mixture. The same procedure was replicated for 20Mg-20Zn-20Fe-20Cu-20C0, 50Mg-25Zn-24Fe-0.5Cu-0.5Co, 70Mg-25Zn-4Fe-0.5Cu-0.5Co, 90Mg-5Zn-4Fe-0.5Cu-0.5Co and pure Mg serving as control. Micro-hardness Vickers property testing of as-sintered samples was performed using ASTM-E384-17 standard at a load of 0.3 KN for 12 s. The average hardness value obtained from five indents on each sample was recorded as the hardness of each sample. The morphologies of alloys were examined by a JEOL JSM-6390A SEM (scanning electron microscope). The microstructures of sintered samples were characterized by a Rigaku Smartlab diffraction with Co K α radiation (λ = 1.78896A) and scan speed 4 deg/s.

## 3. RESULTS AND DISCUSSIONS

### 3.1. Microstructure of Mg-Zn-Fe-Cu-CoAlloys

The thermal analysis results were shown in Fig 1. 20Mg-20Zn-20Fe-20Cu-20Co was melted at about 600 °C and the other alloys were melted at about 650 – 750 °C as seen in Fig 1(b) of DSC curves. Small peaks were shown at a temperature of 425 °C except for 90Mg-5Zn-4Fe-0.5Cu-0.5Co alloy, indicating the formation of the Co-Fe phase [24]. Meanwhile, the valley peak was formed between 500-600 °C, indicating the formation of the $MgZn_2$ phase [25]. Also, the XRD results were matched with the thermal analysis results. According to the TGA results in Fig 1(b), it is shown a difference between 20Mg-20Zn-20Fe-20Cu-20Co alloy and other alloys at a temperature of 400 °C. This was caused by Mg oxidation which changes the mass in the alloy.

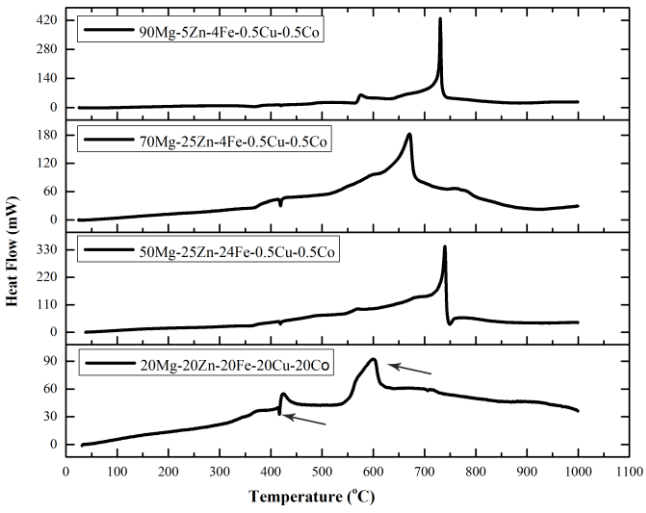


(a)

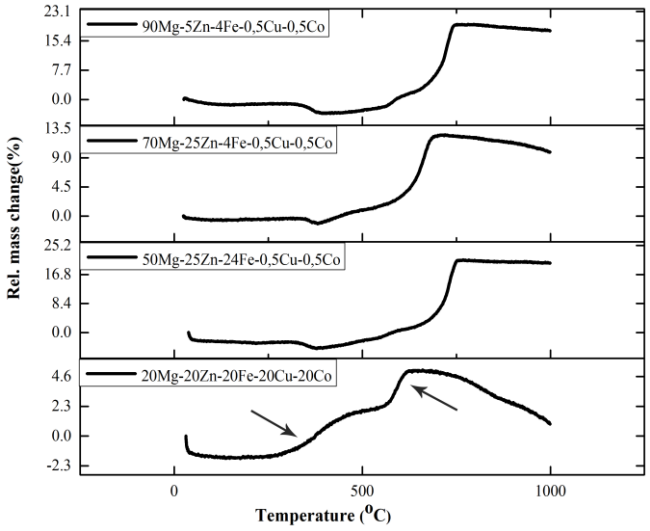


(b)

Figure 1. (a) DSC result and (b) TG result of Mg-Zn-Fe-Cu-Co alloy

The XRD (x-ray diffraction) patterns were shown in Fig 2. Based on equation (1), when the alloys have the same atomic ratio, the mixing entropy reached the maximum. Therefore, as the Mg atomic percentage increases, the mixing entropy decreased [19]. Table 1 shows the entropy results. It is seen that the effect of high mixing entropy significantly occurs in 20Mg-20Zn-20Fe-20Cu-20Co alloy. The solid solution phase was formed previously to the complex intermetallic phase. Only Mg and Co-Fe phase with the structure of HCP and cubic was found in 20Mg-20Zn-20Fe-20Cu-20Co. Other alloys only form complex intermetallic phases, such as the $MgZn_2$ phase, except 90Mg-5Zn-4Fe-0.5Cu-0.5Co which forms the Mg solid solution phase. Moreover, it is shown that the alloys of 50Mg-25Zn-24Fe-0.5Cu-0.5Co and 70Mg-25Zn-4Fe-0.5Cu-0.5Co forms $MgZn_2$, $Cu_2Zn$, MgO, αMg, and Fe phases.

The $MgZn_2$ phase was formed due to the excess Zn element in Mg. The $MgZn_2$ phase is very easy to form because an $MgZn_2$ phase is more stable than Zn which dissolves in the Mg alloy [25]. Based on equations 2 and 3, there is a relationship between enthalpy and δ. The value of δ increases as the enthalpy value decreases [26]-[27]. Thus, the HEA alloy will form a metallic glass alloy with an unstable structure [26],[28]. In this case, the 50 Mg and 70 Mg alloys are characterized by the predominant formation of the intermetallic phase.

The SEM (scanning electron microscope) images of as-sintered Mg-Zn-Fe-Cu-Co alloys were shown in Fig 3.

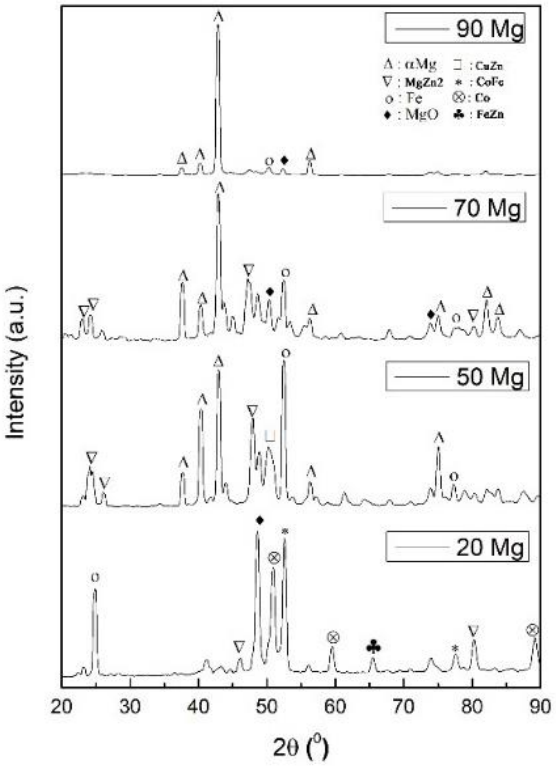


Figure 2. XRD patterns of Mg-Zn-Fe-Cu-Co alloys

The grey globular structure was distributed dispersedly in the base phase of 20Mg-20Zn-20Fe-20Cu-20Co alloy, which was indicated to be the Co-Fe phase. The XRD results match with those of the EDS (energy dispersive spectroscopy) mapping shown in Fig 3. The widths of the globular structure were found less than 5 μm. While, the base phase was a solid solution, which was made up of Mg, Zn, O, and Cu elements. The dark-grey dendritic structure (indicated by white arrow) is evenly distributed in the base phase of 50Mg-25Zn-24Fe-0.5Cu-0.5Co, 70Mg-25Zn-4Fe-0.5Cu-0.5Co, and 90Mg-5Zn-4Fe-0.5Cu-0.5Co alloys, which indicates the formation of the $MgZn_2$, Fe and Cu phase. The inter-dendritic structure (shown by black arrow) or base alloys was a solid solution, consisting of the Mg and MgO phases.

Table 1. High entropy properties of Mg-Zn-Fe-Cu-Co alloys

| Alloys | ΔHm (kJ/mol) | ΔSm (J/K mol) | ΔG | δ |
|---|---|---|---|---|
| 20Mg20Zn20Fe20Cu20Co | 2.321 | 12.6 | 6.70 | 12.463 |
| 50Mg25Zn24Fe0.5Cu0.5Co | 5.116 | 6.83 | 1.37 | 16.130 |
| 70Mg25Zn4Fe0.5Cu0.5Co | -0.27 | 4.04 | -13.5 | 17.527 |
| 90Mg5Zn4Fe0.5Cu0.5Co | 0.820 | 1.80 | 2.06 | 18.490 |

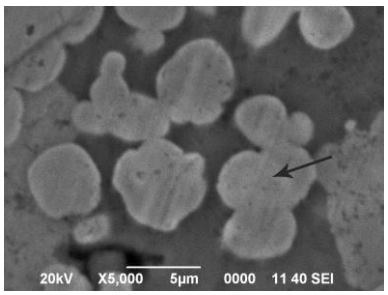


(a)

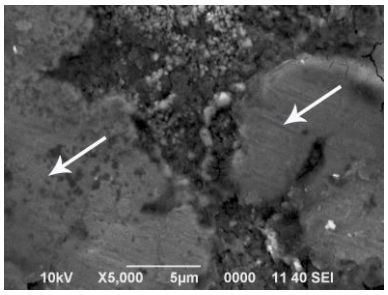


(b)

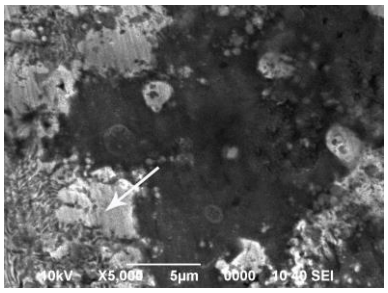


(c)

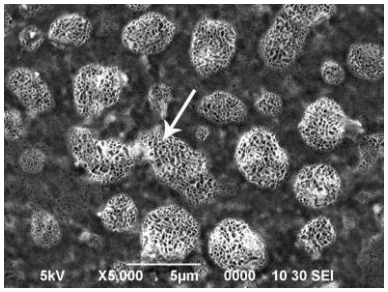


(d)

Figure 3. SEM images of Mg-Zn-Fe-Cu-Co alloys: (a) 20Mg-20Zn-20Fe-20Cu-20Co; (b) 50Mg-25Zn-24Fe-0.5Cu-0.5Co; (c) 70Mg-25Zn-4Fe-0.5Cu-0.5Co; (d) 90Mg-5Zn-4Fe-0.5Cu-0.5Co; and (e) pure Mg

The MgO peak was higher because magnesium tends to react with oxygen, and MgO was the main oxide phase in the magnesium matrix. MgO differs from other combining elements in that MgO was formed at the grain boundaries, whereas MgO is uniformly distributed in the Mg matrix. The presence of MgO can increase the hardness of magnesium and can also stimulate the formation of pores on the surface of Mg which is very useful for implant applications that can be damaged [26].

### 3.2. Mechanical Properties of Mg-Zn-Fe-Cu-Co Alloys

The densities and hardness of Mg-Zn-Fe-Cu-Co alloys were shown in Fig 4(a), and Fig 4(b) respectively. Mg-Zn-Fe-Cu-Co alloys exhibited medium densities (3.057 $g.cm^{-3}$ – 1.711 $g.cm^{-3}$) and medium hardness (286 HV-81 HV), as can be seen in Table 2. The density of the alloy decreases with the increase of magnesium addition, while the densities increase with increasing Zn content in alloys [19],[27]. The shape of the Zn and Mg grains is relatively the same as the spherical shape and the particle size of Mg is larger than Zn. When Zn and Mg are combined, the smaller Zn particles will fill the space between the larger Mg particles. Therefore, the Zn particles will diffuse into Mg [28]. Decreasing the density can also be caused by the lack of pressure during the compaction process [27]. The actual density (gradient line) is lower than theoretical density (black line) as shown in Fig. 4 (a), where the greatest loss was found in 90Mg-5Zn-4Fe-0.5Cu-0.5Co alloys by 36%. The low density was caused by the presence of oxides and porosity which occurs on samples during the sintering process in addition to the imperfections sintering process [29].

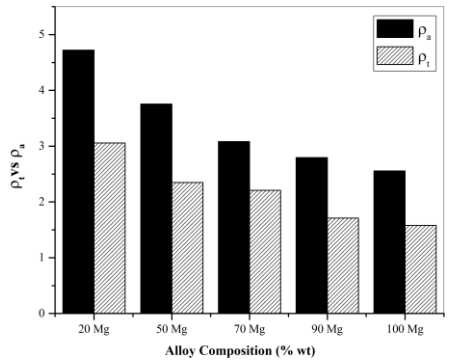


(a)

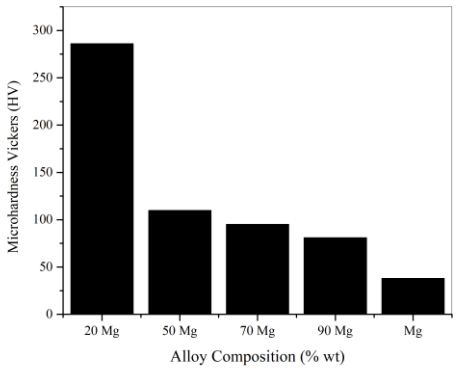


(b)

Figure 4. (a) Actual density vs theoretical density of Mg-Zn-Fe-Cu-Co, (b) microhardness of Mg-Zn-Fe-Cu-Co and (c) presence pores on surface of 20Mg-20Zn-20Fe-20Cu-20Co alloy

Figure 4(b) clearly shows that a similar pattern of behavior in hardness result was obtained. This reduction in hardness over 20Mg-20Zn-20Fe-20Cu-20Co may be a result of the increasing magnesium content in the alloy. The high hardness of 20Mg-20Zn-20Fe-20Cu-20Co (286.08 HV) is due to the presence of an intermetallic phase and high density [30]. The Co-Fe phase is an intermetallic phase present at the grain boundaries of the 20Mg-20Zn-20Fe-20Cu-20Co alloy, resulting from the predominance of Co and Fe elements. It is also believed that the $MgZn_2$ phase as laves phase in the matrix makes the alloy harder and brittle [25]. The hardness of Mg-Zn-Fe-Cu-Co is promising for candidate ureteral application because it was similar to the AZ31 alloy (120-132 HV) and ZK60 alloy (~100 HV) that have been reported in previous studies [2], [31]-[32].

Table 2. Density and micro-hardness properties of Mg-Zn-Fe-Cu-Co alloys at room temperature

| Alloy | $\rho_{theory}$ ($g.cm^{-3}$) | $\rho_{actual}$ ($g.cm^{-3}$) | % Porosity | Micro-Hardness (HV) |
|---|---|---|---|---|
| 20Mg | 4.721 | 3.057 | 35 | 286.06 |
| 50Mg | 3.756 | 2.347 | 37 | 109.78 |
| 70Mg | 3.082 | 2.207 | 28 | 95 |
| 90Mg | 2.795 | 1.711 | 39 | 80.98 |
| Mg | 2.557 | 1.581 | 38 | 37.9 |

## 4. CONCLUSIONS

In the current study, biomaterial high entropy Mg-Zn-Fe-Cu-Co alloy was effectively produced by powder metallurgy route, while mechanical and morphological properties were intensively explored. The following are the finding of the study. Mg-Zn-Fe-Cu-Co alloys were designed by utilizing the strategy of equiatomic ratio and high entropy of mixing. The alloys were essentially multiphase and crystalline. An alloy of 20Mg-20Zn-20Fe-20Cu-20Co has consisted of the HCP phase and cubic phase.

The physical and mechanical properties of Mg-Zn-Fe-Cu-Co were influenced by the magnesium content in the matrix alloys. The presence of pores gave poor results in terms of compaction and the sintering process. Mg-Zn-Fe-Cu-Co alloys have a medium hardness between 286.06 HV and 80.98 HV, while the densities of alloys were moderate between 3.057 $g.cm^{-3}$ and 1.71 $g.cm^{-3}$. It is believed that solid solution strengthening and intermetallic strengthening were the main strengthening mechanics of the alloys.

Based on the results it is concluded that high entropy is a promising method for the processing of Mg elements. Moreover, the 20Mg-20Zn-20Fe-20Cu-20Co alloy having ideal mechanical properties that meet the minimum requirements for high entropy alloys. But further developments still need to be done, such as optimization of the sintering temperature in the process of making high entropy alloys and controlling the oxidation of magnesium alloys using the powder metallurgy method, so that the formation of the alloy surface becomes smoother.


## ACKNOWLEDGEMENT

This project is supported by Research Center for Metallurgy and Materials, Indonesian Institute of Science and Departement of Metallurgical Engineering, Bandung Institute of Technology.


## REFERENCES


[1] R. Kurniawan, "Profile of patients with urinary tract stone at urology departement of Soetomo general hospital Surabaya in january 2016-december 2016," *Indonesian Journal of Urology*, vol. 27, no 1, pp. 22-25, 2020. Doi: 10.32421/juri.v27i1.506.

[2] S. Zhang, Y. Bi, J. Li, Z. Wang, J. Yan, J. Song, H. Sheng, H. Guo, and Y. Li, "Biodegradation behavior of magnesium and ZK60 alloy in artificial urine and rat models," *Bioact. Mater.*, vol. 2, no. 2, pp. 53–62, 2017. Doi :10.1016/j.bioactmat.2017.03.004.

[3] Z. Ma, M. Gao, D. Na, Y. Li, L. Tan, and K. Yang, "Study on a biodegradable antibacterial Fe-Mn-C-Cu alloy as urinary implant material," *Mater. Sci. Eng. C*, vol. 103, no. May, 2019. Doi:10.1016/j.msec.2019.05.003.

[4] J. Y. Lock, E. Wyatt, S. Upadhyayula, A. Whall, V. Nuñez, V. I. Vullev, and H. Liu, "Degradation and antibacterial properties of magnesium alloys in artificial urine for potential resorbable ureteral stent applications," *J. Biomed. Mater. Res. - Part A*, vol. 102, no. 3, pp. 781–792, 2014. Doi : 10.1002/jbm.a.34741.

[5] D. Tie, H. Liu, R. Guan, P. Holt-Torres, Y. Liu, Y. Wang, and N. Hort, "In vivo assessment of biodegradable magnesium alloy ureteral stents in a pig model," *Acta Biomater.*, vol. 116, pp. 415–425, 2020. Doi: 10.1016/j.actbio.2020.09.023.

[6] K. Zhang, H. Cui, H. Jiang, Y. Hao, R. Long, Q. Ma, and H. Zhang, "The current status and applications of ureteral stents,"

*Int. J. Clin. Exp. Med.*, vol. 13, no. 4, pp. 2122–2133, 2020.

[7] F. Soria, E. Morcillo, A. Serrano, A. Budia, I. Fernández, T. Fernández-Aparicio, and F. M. Sanchez-Margallo, "Evaluation of a new design of antireflux-biodegradable ureteral stent in animal model," *Urology*, vol. 115, pp. 59–64, 2018. Doi: 10.1016/j.urology.2018.02.004.

[8] X. Ma, Y. Xiao, H. Xu, K. Lei, and M. Lang, "Preparation, degradation and in vitro release of ciprofloxacin-eluting ureteral stents for potential antibacterial application," *Mater. Sci. Eng. C*, vol. 66, pp. 92–99, 2016. Doi : 10.1016/j.msec.2016.04.072.

[9] Y. Chen, J. Dou, H. Yu, and C. Chen, "Degradable magnesium-based alloys for biomedical applications: The role of critical alloying elements," *J. Biomater. Appl.*, vol. 33, no. 10, pp. 1348–1372, 2019. Doi :10.1177/0885328219834656.

[10] D. Orlov, G. Raab, T. T. Lamark, M. Popov, and Y. Estrin, "Improvement of mechanical properties of magnesium alloy ZK60 by integrated extrusion and equal channel angular pressing," *Acta Mater.*, vol. 59, no. 1, pp. 375–385, 2011. Doi:10.1016/j.actamat.2010.09.043.

[11] W. Yu, Z. Liu, H. He, N. Cheng, and X. Li, "Microstructure and mechanical properties of ZK60-Yb magnesium alloys," *Mater. Sci. Eng. A*, vol. 478, no. 1–2, pp. 101–107, 2008. Doi :10.1016/j.msea.2007.09.027.

[12] S. Champagne, E. Mostaed, F. Safizadeh, E. Ghali, M. Vedani, and H. Hermawan, "In vitro degradation of absorbable zinc alloys in artificial urine," *Materials (Basel).*, vol. 12, no. 2, pp. 1–13, 2019. Doi :10.3390/ma12020295.

[13] Y. Ding, C. Wen, P. Hodgson, and Y. Li, "Effects of alloying elements on the corrosion behavior and biocompatibility of biodegradable magnesium alloys: A review," *J. Mater. Chem. B*, vol. 2, no. 14, pp. 1912–1933, 2014. Doi :10.1039/C3TB21746A.

[14] S. Agarwal, J. Curtin, B. Duffy, and S. Jaiswal, "Biodegradable magnesium alloys for orthopaedic applications: A review on corrosion, biocompatibility and surface modifications," *Mater. Sci. Eng. C*, vol. 68, pp. 948–963, 2016. Doi : 10.1016/j.msec.2016.06.020.

[15] S. K. Jaganathan, E. Supriyanto, S. Murugesan, A. Balaji, and M. K. Asokan, "Biomaterials in cardiovascular research: Applications and clinical implications," *Biomed Res. Int.*, vol. 2014, 2014. Doi : 10.1155/2014/459465.

[16] G. Senopati, C. Sutowo, F. Rokhmanto, I. Kartika, and B. Suharno, "Microstructure , mechanical properties , and corrosion resistance of Ti-6Mo-6Nb-xSn alloys for biomedical application," vol. 988, pp. 175–181, 2020. Doi : 10.4028/www.scientific.net/MSF.988.175.

[17] M. Todai, T. Nagase, T. Hori, A. Matsugaki, A. Sekita, and T. Nakano, "Novel TiNbTaZrMo high-entropy alloys for metallic biomaterials," *Scr. Mater.*, vol. 129, pp. 65–68, 2017. Doi : 10.1016/j.scriptamat.2016.10.028.

[18] V. Geanta, I. Voiculescu, P. Vizureanu, and A. Victor Sandu, "High entropy alloys for medical applications," *Eng. Steels High Entropy-Alloys*, pp. 4–12, 2020. Doi : 10.5772/intechopen.89318.

[19] R. Li, J. Gao, and K. Fa, "Study to microstructure and mechanical properties of Mg containing high entropy alloys," *Mater. Sci. Forum*, vol. 650, pp. 265–271, 2010. Doi : 10.4028/www.scientific.net/MSF.650.265.

[20] Y. J. Zhou, Y. Zhang, Y. L. Wang, and G. L. Chen, "Solid solution alloys of AlCoCrFeNi Tix with excellent room-temperature mechanical properties," *Appl. Phys. Lett.*, vol. 90, no. 18, 2007. Doi :10.1063/1.2734517.

[21] A. Kumar and M. Gupta, "An insight into evolution of light weight high entropy alloys: A review," *Metals (Basel).*, vol. 6, no. 9, 2016. Doi : 10.3390/met6090199.

[22] N. Sharma, G. Singh, P. Sharma, and A. Singla, "Development of Mg-Alloy by powder metallurgy method and its characterization," *Powder Metall. Met. Ceram.*, vol. 58, no. 3–4, pp. 163–169, 2019. Doi : 10.1007/s11106-019-00060-5.

[23] A. R. Miedema, P. F. de Châtel, and F. R. de Boer, "Cohesion in alloys - fundamentals of a semi-empirical model," *Phys. B+C*, vol. 100, no. 1, pp. 1–28, 1980. Doi :10.1016/0378-4363(80)90054-6.

[24] L. A. Dreval, M. A. Turchanin, P. G. Agraval, and Y. Du, "Cu–Fe–Co system: Verification of the high-temperature phase equilibria and thermodynamic modeling of the low-temperature phase relations involving ordered phase," *Powder Metall. Met. Ceram.*, vol. 56, no. 9–10, pp. 546–

555, 2018. Doi :10.1007/s11106-018-9927-7.
[25] J. Nei, K. Young, S. O. Salley, and K. Y. S. Ng, "Determination of C14/C15 phase abundance in laves phase alloys," *Mater. Chem. Phys.*, vol. 136, no. 2–3, pp. 520–527, 2012. Doi : 10.1016/j.matchemphys.2012.07.020.
[26] Y. Chen, Z. Feng, and W. Zhang, "Effect of MgO content on mechanical properties of directionally solidified pure magnesium," *Mater. Res.*, vol. 24, no. 2, 2021. Doi : 10.1590/1980-5373-MR-2020-0469.
[27] M. Y. Kolawole, J. O. Aweda, F. Iqbal, A. Ali, and S. Abdulkareem, "Mechanical properties of powder metallurgy processed biodegradable Zn-based alloy for biomedical application," *Int. J. Mater. Metall. Eng.*, vol. 13, no. 12, pp. 558–563, 2019. Doi :10.5281/zenodo.3593236.
[28] J. Yu, J. Wang, Q. Li, J. Shang, J. Cao, and X. Sun, "Effect of Zn on microstructures and properties of Mg-Zn alloys prepared by powder metallurgy method," *Rare Met. Mater. Eng.*, vol. 45, no. 11, pp. 2757–2762, 2016. Doi : 10.1016/S1875-5372(17)30035-8.
[29] E. M. Salleh, H. Zuhailawati, S. Ramakrishnan, and M. A. H. Gepreel, "A statistical prediction of density and hardness of biodegradable mechanically alloyed Mg-Zn alloy using fractional factorial design," *J. Alloys Compd.*, vol. 644, pp. 476–484, 2015. Doi :10.1016/j.jallcom.2015.04.090.
[30] G. Tosun and M. Kurt, "The porosity, microstructure, and hardness of Al-Mg composites reinforced with micro particle SiC/Al2O3 produced using powder metallurgy," *Compos. Part B Eng.*, vol. 174, p. 106965, 2019. Doi : 10.1016/j.compositesb.2019.106965.
[31] S. A. Torbati-Sarraf and T. G. Langdon, "Properties of a ZK60 magnesium alloy processed by high-pressure torsion," *J. Alloys Compd.*, vol. 613, pp. 357–363, 2014. Doi : 10.1016/j.jallcom.2014.06.056.
[32] J. Xu, X. Wang, M. Shirooyeh, G. Xing, D. Shan, B. Guo, and T. G. Langdon, "Microhardness, microstructure and tensile behavior of an AZ31 magnesium alloy processed by high-pressure torsion," *J. Mater. Sci.*, vol. 50, no. 22, pp. 7424–7436, 2015. Doi :10.1007/s10853-015-9300-x.

Metalurgi (2021) 1: 33 - 42

METALURGI
Majalah Ilmu dan Teknologi
p-ISSN 0126-3188 | e-ISSN 2443-3926
www.ejurnalmaterialmetalurgi.com

# PENGARUH PENEMPAAN DAN PERLAKUAN PANAS TERHADAP SIFAT MEKANIK DAN KETAHANAN KOROSI PADA MODIFIKASI BAJA LATERIT A-588

**Miftakhur Rohmah*, Dedi Irawan, Toni Bambang Romijarso**
Pusat Penelitian Metalurgi dan Material-LIPI
Gedung 470, Kawasan Puspiptek, Tangerang Selatan, Indonesia 15343
*E-mail: Miftakhur.rohmah@lipi.go.id

*Masuk tanggal : 22-02-2021, revisi tanggal : 16-04-2021, diterima untuk diterbitkan tanggal 30-04-2021*

## Abstrak

Baja paduan rendah berkekuatan tinggi yang diaplikasikan menjadi baja tahan cuaca merupakan terobosan terbaru untuk menghasilkan sifat mekanik dan ketahanan korosi yang tinggi. Modifikasi baja laterit dengan penambahan kadar nikel yang diterapkan proses termomekanikal terkontrol (TMCP) berupa kombinasi proses penempaan panas dan perlakuan panas menjadi fokus penelitian ini. Sampel yang digunakan merupakan baja laterit A-588 hasil *investment casting* yang ditambahkan 1, 2, dan 3 %berat nikel, kemudian diproses penempaan panas dengan pembebanan 100 ton pada temperatur 1050 ℃. Nikel berfungsi sebagai penstabil austenit. Variabel perlakuan panas yang digunakan yakni (1) langsung pendinginan udara, (2) dilanjutkan proses pemanasan pada temperatur 750 ℃ yang diikuti pendinginan cepat. Karakterisasi material menggunakan uji metalografi, uji keras, uji tarik, dan uji polarisasi. Pada hasil tempa panas+pendinginan udara, pertambahan kadar nikel hingga 3 %massa mempengaruhi nilai fraksi fasa ferrit-perlit yang terbentuk, pertambahan ukuran butir hingga ±0,1 mm, penurunan kekerasan hingga 185,22 BHN, penurunan kekuatan hingga 554 MPa, dan pertambahan regangan sebesar 29,1%. Sedangkan pada hasil tempa panas+perlakuan panas dengan pendinginan air, pertambahan nikel hingga 3 %massa menyebabkan terbentuknya fasa bilah martensit + ferrit + austenit sisa, penurunan kekerasan hingga 236,18 BHN, penurunan kekuatan hingga 852 MPa, penurunan regangan hingga 24,7%. Fasa austenit sisa (*retained austenite)* memiliki efek merusak pada sifat mekanis.

**Kata Kunci:** Baja laterit A-588, austenit sisa, modifikasi baja laterit, tempa panas

## Abstract

*The application of HSLA (high-strength low alloy) for weathering steels is the newest innovation to produce high mechanical and corrosion resistance properties. Modification of laterite steel by nickel addition with a TMCP (thermomechanical control process) in the form of a combination of hot forging and heat treatment processes is the focus of this study, in which a nickel acts as an austenite stabilizer. The sample used was A-588 Lateritic Steel, resulting from investment casting, which has added nickel content of 1, 2, and 3%, then processed by hot forging with 100 tons loading at 1050 ℃. Heat treatment variables used were (1) direct air cooling and (2) followed by a heating process at a temperature of 750 ℃ followed by a rapid cooling process. Material characterization was using a metallographic test, hardness test, tensile test, and polarization test. In hot forging + air cooling samples, the increase in nickel content up to 3 %mass affects the value of the ferrite-pearlite phase fraction formed, the increase in grain size up to ± 0,1 mm, the decrease in hardness is up to 185.22 BHN, the decline in strength is up to 554 MPa, and the elongation increase is 29.1%. Whereas in the hot forging sample + heat treatment with water cooling, the rise in nickel up to 3 %mass causes the formation of martensite + ferrite + retained austenite lath phase, a decrease in hardness to 236.18 BHN, a reduction in strength to 852 MPa, a decrease in elongation up to 24.7%. The retained austenite phase has a detrimental effect on mechanical properties.*

***Keywords:*** *A-588 lateritic steel, retained austenite, lateritic steel modification, hot forging*

## 1. PENDAHULUAN

Material baja tahan cuaca untuk aplikasi infrastruktur khususnya struktur rangka jembatan di Indonesia menjadi salah satu fokus penelitian untuk meningkatkan sifat mekanik dan sifat ketahanan korosi atmosferik dari baja paduan

rendah-berkekuatan tinggi (*high strength low alloy* / HSLA). Sayangnya, kedua sifat ini sering berbanding terbalik, dengan satu peningkatan dengan mengorbankan sifat lainnya. Dengan sifat "*self protection*" yang membentuk lapisan pelindung patina, baja tersebut dapat melindungi dari serangan korosi ketika terpapar dengan lingkungan atmosferik. Material baja tahan cuaca biasanya tidak memerlukan bentuk pemeliharaan apapun seperti pengecatan dan proteksi katodik, sehingga dapat dijadikan material alternatif yang sangat hemat biaya, jika dibandingkan dengan baja struktural lainnya. Umumnya, material baja tahan cuaca didominasi oleh baja paduan kromium-tembaga dengan penambahan unsur pemadu Ni, P, Mn, Si dan lain-lain yang total kadarnya tidak kurang dari 3-5 %, seperti pada material ASTM A-242, A-588, A-606, A-709, A-852, A-871 [1]-[2]. Karakteristik lapisan pelindung patina yang stabil dipengaruhi oleh: (a) komposisi kimia seperti Al dan Si, (b) pemrosesan baja, berkaitan dengan struktur mikro dan kehalusan butir, (c) kondisi lingkungan, (d) waktu pemaparan, (e) desain struktur [1],[3]–[5].

Konsep pengembangan baja tahan cuaca dengan meningkatkan kadar nikel hingga 3% telah dilakukan beberapa waktu lalu [4]. Namun, kadar Ni yang tinggi akan meningkatkan biaya pembuatan baja. Oleh karena itu, diperlukan upaya pengembangan baja tahan cuaca yang berasal dari baja laterit Indonesia yang memiliki kandungan nikel antara 2-3% setelah melewati proses converting dan metalurgi sekunder lainnya. Baja laterit memiliki kekuatan dan kekerasan tinggi dengan maksimum nikel 3%. Adanya kandungan nikel hingga 3% diharapkan dapat menggantikan penambahan ferronikel sehingga mengurangi biaya produksi.

Nikel berpeluang untuk menggantikan peranan krom pada paduan, sebagai penstabil austenit, meningkatkan ketangguhan, keuletan, dan ketahanan korosi. Y. Zhou, dkk. [6], dan X. Cheng, dkk. menyimpulkan bahwa nilai ketahanan korosi meningkat seiring dengan pertambahan nikel, namun mencapai batas efisien pada 3,5% Ni. Nikel mempengaruhi pembentukan lapisan protektif yang kompak, meningkatkan laju nukleasi $Fe(O,OH)_6$ jaringan nano, serta menghalangi pembentukan $Fe_2NiO_4$ yang tidak menguntungkan [7].

Baja hasil pengecoran memiliki cacat berupa porositas dan inklusi yang mengakibatkan sifat mekanis rendah sehingga diperlukan upaya untuk meningkatkannya dengan kombinasi perlakuan panas dan penempaan. Pada penelitian terdahulu, baja dengan perlakuan termomekanikal (pengerolan) yang menghasilkan struktur mikro ferrit-perlit atau bainit adalah pola utama untuk menghasilkan sifat mekanik dan ketahanan korosi atmosferik yang luar biasa tinggi [4]. Selain itu, proses perlakuan panas dan pembentukan logam dapat merekayasa struktur mikro sesuai yang diharapkan. Proses tempa menghasilkan aliran butir pada struktur mikronya, sehinga hasil produk akhir memiliki integritas struktural yaitu tanpa adanya kekosongan internal (*void*) dan porositas, serta memiliki sifat mekanik yang seragam. Oleh karena itu, penelitian ini secara khusus bertujuan untuk mengetahui pengaruh proses penempaan panas (*hot forging*) yang dilanjutkan proses perlakuan panas terhadap sifat mekanik dan ketahanan korosi pada material baja laterit, khususnya modifikasi paduan A-588. Material A-588 merupakan salah satu HSLA yang diaplikasikan menjadi baja tahan cuaca.

## 2. PROSEDUR PERCOBAAN

Material awal yang digunakan dalam penelitian ini adalah baja laterit hasil pengecoran yang dibuat oleh Pusat Penelitian Metalurgi dan Material LIPI dengan komposisi utama mengacu pada standard ASTM A 588. Baja laterit merupakan baja yang diperoleh dari proses pemurnian dan peleburan ulang NPI (*nickel pig iron*). Untuk mengetahui pengaruh kadar nikel dalam baja laterit, modifikasi paduan dilakukan dengan cara perubahan komposisi kimia, yakni dengan menambahkan 1, 2, dan 3 %berat nikel ke dalam paduan utama, sehingga diperoleh komposisi kimia seperti pada Tabel 1. Paduan yang terbentuk tanpa mengandung unsur vanadium dan silikon jika dibandingkan dengan ASTM A-588.

Tabel 1. Komposisi kimia dari baja laterit A-588 - hasil pengecoran (%berat)

| Komposisi Kimia (%berat) | Modifikasi Baja Laterit | | | |
|---|---|---|---|---|
| | MBL#1 | MBL#2 | MBL#3 | MBL#4 |
| C | 0,16 | 0,15 | 0,14 | 0,13 |
| Mn | 0,74 | 0,67 | 0,56 | 0,48 |
| P | 0,01 | 0,01 | 0,01 | 0,01 |
| Si | 0,12 | 0,07 | - | - |
| Ni | 0,42 | 0,98 | 1,96 | 3,29 |
| Cr | 0,62 | 0,63 | 0,61 | 0,59 |
| Cu | 0,33 | 0,34 | 0,21 | 0,20 |
| V | - | - | - | - |
| S | 0,01 | 0,01 | 0,01 | 0,01 |

Variabel pada penelitian ini adalah perbedaan kandungan kadar nikel dan perbedaan perlakuan panas pada modifikasi baja laterit, yakni 0,42 %berat nikel (kode sampel MBL#1); 1 %berat nikel (kode sampel MBL#2); 2 %berat nikel (kode sampel MBL#3); dan 3 %berat nikel

(kode sampel MBL#4) dari berat total. Secara umum, komposisi kimia baja laterit termodifikasi sesuai dengan ASTM A-588 Grade K. ASTM A-588 komersil mengandung 0,17 %berat karbon (maks), 0,50-1,20 %berat mangan, 0,04 %berat fosfor (maks), 0,05 %berat sulfur (maks), 0,4 %berat nikel (maks), 0,40-0,7 %berat krom, 0,1 %berat molibdenum (maks), dan 0,30-0,50 %berat tembaga [8]. Oleh karena itu, kadar unsur lainnya dianggap homogen dan tidak mempengaruhi secara signifikan karena masih dalam standar paduan A-588.

Paduan hasil pengecoran dipotong sebesar 10x1x1 cm sebanyak 2 buah. Selanjutnya, material tersebut dijadikan bahan baku pada proses tempa panas dan dilanjutkan perlakuan panas dengan diagram proses seperti diilustrasikan pada Gambar 1. Semua komposisi dipanaskan hingga temperatur austenisasi 1050 °C selama 30 menit didalam *muffle furnace* (kecepatan pemanasan 5 °C/menit), dan dilanjutkan dengan proses tempa panas (*hot forging – single punch*).

Proses penempaan dilakukan dengan menggunakan mesin Liyaoyang Metal Forming Tipe J53 dengan beban tempa sebesar 100 ton pada udara ruangan (*open die forging*). Selanjutnya, masing-masing sampel dilakukan variasi perlakuan panas, yakni (A) pendinginan udara / *normalizing*, dan (B) proses rekristalisasi dengan melakukan pemanasan ulang pada 750 °C selama 30 menit dan dilanjutkan dengan pendinginan cepat menggunakan media air (*quenching*). Proses penempaan-dua siklus menghasilkan reduksi ketebalan sebesar 38,84%.

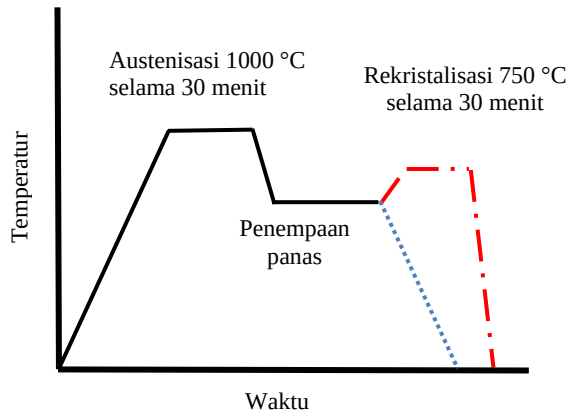


Gambar 1. Mekanisme proses penempaan dan perlakuan panas pada modifikasi baja laterit A-588

Baja laterit hasil tempa dan perlakuan panas kemudian dilakukan karakterisasi sifat mekanik melalui pengujian tarik, kekerasan, metalografi, serta karakterisasi sifat korosi melalui pengujian polarisasi. Pengujian kekerasan menggunakan metode Brinell (merk Mitutoyo HM-200) dengan beban identasi 1000 kgf selama 10 detik.

Pada pengujian metalografi, sampel uji dipreparasi menjadi ukuran 1x1x1 cm, kemudian dimounting dengan resin, diamplas, dipoles, dan dietsa menggunakan larutan pikral. Proses pengampelasan menggunakan kertas ampelas mulai kekasaran grade 80 - 2000. Sedangkan, proses pemolesan menggunakan pasta alumina dengan kekasaran 5 – 0,1 µm. Pada pengujian tarik, sampel uji dipreparasi mengacu pada standar ASTM E8.

Pengujian polarisasi dilakukan untuk mengetahui karakteristik sampel dengan media korosif berupa larutan NaCl 3,5 %volume pada temperatur kamar. Pengujian ini dilakukan dengan menggunakan tiga elektroda yaitu elektrode kalomel jenuh (SCE) sebagai elektroda referensi, platina sebagai elektroda pembantu, dan sampel sebagai elektroda kerja. Sampel dicelupkan selama 1 jam sebelum memulai uji polarisasi. Uji polarisasi dilakukan pada rentang potensial -200mV sampai +200 mV dengan kecepatan scan 1mV/s.

## 3. HASIL DAN PEMBAHASAN

### 3.1. Pengamatan Struktur Mikro

Pengamatan struktur mikro dilakukan untuk mengetahui fasa akhir pada modifikasi baja laterit A-588 sehingga dapat diprediksikan transformasi fasa yang terjadi selama proses penempaan dan perlakuan panas. Pengamatan dilakukan dengan perbesaran 500x (20µm) dengan etsa pikral. Struktur mikro baja laterit setelah proses penempaan dan perlakuan panas ditunjukkan pada Gambar 2.

Gambar 2 menunjukkan struktur mikro pada modifikasi baja laterit A-588 dengan proses tempa dan perlakuan panas yang dilanjutkan dengan pendinginan udara terbuka (*normalizing*). Pada gambar tersebut, secara umum, struktur mikro yang terbentuk setelah proses A menjadi ferit (warna terang), perlit (warna gelap), dan karbida yang tersebar dalam struktur ferit. Struktur mikro *as-cast* setelah tempa panas menghasilkan butiran ferit berbentuk kolom halus yang cenderung memanjang (Gambar 2(a)). Seiring dengan penambahan kadar nikel, butiran ferit menjadi agak kasar seperti pulau tidak beraturan (Gambar 2(b)-2(d)). Pengasaran butiran adalah fenomena yang terjadi selama proses termomekanik seperti tempa panas [9]. Ukuran butir (*micro grain size number* G) dapat ditentukan menggunakan metode *Intercept* (Heyne) sesuai ASTM E112. Variasi penambahan kadar nikel pada penelitian ini berpengaruh terhadap nilai fraksi fasa ferit-perlit

yang terbentuk dan ukuran butir. Peningkatan kadar nikel akan meningkatkan fraksi perlit dan ukuran butir, seperti ditunjukkan pada Tabel 2. Selain itu, modifikasi baja laterit A-588 dengan kondisi tempa panas ternyata memiliki beberapa porositas yang disebabkan oleh kualitas produk hasil cor.

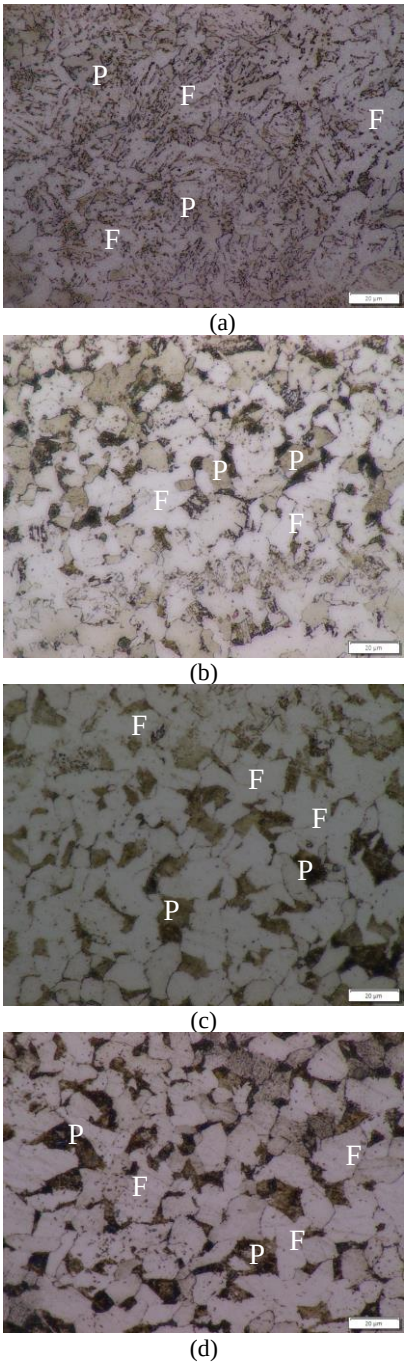


Gambar 2. Struktur mikro pada modifikasi baja laterit A-588 (a) 0,42, (b) 1, (c) 2, dan (d) 3 %berat nikel setelah proses penempaan yang dilanjutkan dengan pendinginan udara terbuka (*normalizing*) – etsa pikral (F=ferit dan P=perlit). Etsa Pikral

Peningkatan ukuran butir pada penelitian ini sesuai dengan analisis ukuran butir Uddeholm Nimax, yang menyatakan bahwa prediksi ukuran butir untuk baja paduan rendah secara empiris dipengaruhi oleh temperatur pemanasan, waktu pemanasan, serta persen berat unsur Ni, Cr, Mo, dan C [10]. Pada saat baja laterit dipanaskan hingga temperatur austenisasi (melewati garis $A_1$), ferit dan perlit terlarut membentuk nukleasi dan pertumbuhan fasa austenit awal. Adanya penstabil austenit seperti nikel memungkinkan pembentukan austenit lebih banyak dan mendorong pertumbuhan butir yang cepat sehingga butiran semakin halus. Pada saat tempa panas, rekristalisasi butiran austenit dan transformasi fasa terjadi bersamaan dengan adanya deformasi sehingga ukuran butir austenit menjadi semakin besar dan kasar. Seiring pendinginan udara terbuka selama proses penempaan, sulit untuk mengkristalkan kembali austenit yang mengalami deformasi karena nukleasi yang tertunda menghambat proses dinamik rekristalisasi, sehingga fasa austenit cenderung bertransformasi menjadi ferit dan perlit [9],[11].

Peningkatan ukuran butir pada penelitian ini sesuai dengan analisis ukuran butir Uddeholm Nimax, yang menyatakan bahwa prediksi ukuran butir untuk baja paduan rendah secara empiris dipengaruhi oleh temperatur pemanasan, waktu pemanasan, serta persen berat unsur Ni, Cr, Mo, dan C [10]. Pada saat baja laterit dipanaskan hingga temperatur austenisasi (melewati garis $A_1$), ferit dan perlit terlarut membentuk nukleasi dan pertumbuhan fasa austenit awal. Adanya penstabil austenit seperti nikel memungkinkan pembentukan austenit lebih banyak dan mendorong pertumbuhan butir yang cepat sehingga butiran semakin halus. Pada saat tempa panas, rekristalisasi butiran austenit dan transformasi fasa terjadi bersamaan dengan adanya deformasi sehingga ukuran butir austenit menjadi semakin besar dan kasar. Seiring pendinginan udara terbuka selama proses penempaan, sulit untuk mengkristalkan kembali austenit yang mengalami deformasi karena nukleasi yang tertunda menghambat proses dinamik rekristalisasi, sehingga fasa austenit cenderung bertransformasi menjadi ferit dan perlit [9],[11].

Tabel 2. Nilai fraksi fasa dan ukuran butir dengan bantuan aplikasi *ImageJ* pada modifikasi baja laterit A-588

| Material | Fraksi fasa (%vol.) | | Ukuran butir | |
|---|---|---|---|---|
| | Ferrit | Perlit | µm | No. G |
| MBL #1 | 76,96 | 23,04 | ± 55µm | 5,5 |
| MBL #2 | 75,71 | 24,29 | ± 75 µm | 4,5 |
| MBL #3 | 75,15 | 24,85 | ± 90 µm | 4 |
| MBL #4 | 72,63 | 27,37 | ± 0,1 mm | 3,7 |

Struktur mikro pada modifikasi baja laterit A-588 setelah proses tempa panas dan perlakuan panas dengan pendinginan air ditunjukkan pada

Gambar 3. Semua Gambar 3(a)-3(d) menunjukkan mikrostruktur multifasa yang meliputi bilah martensit, ferit, dan austenit sisa dengan distribusi homogen. Austenit sisa (*retained austenite*-RA) diindikasikan seperti blok tidak beraturan berwarna terang dengan batas butir kabur. Pemanasan pada temperatur 750 ℃ merupakan pemanasan interkritikal yang mengubah fasa perlit ($\alpha$+$Fe_3C$) stabil di temperatur ruang (proses A) menjadi fasa austenit ($\gamma$).

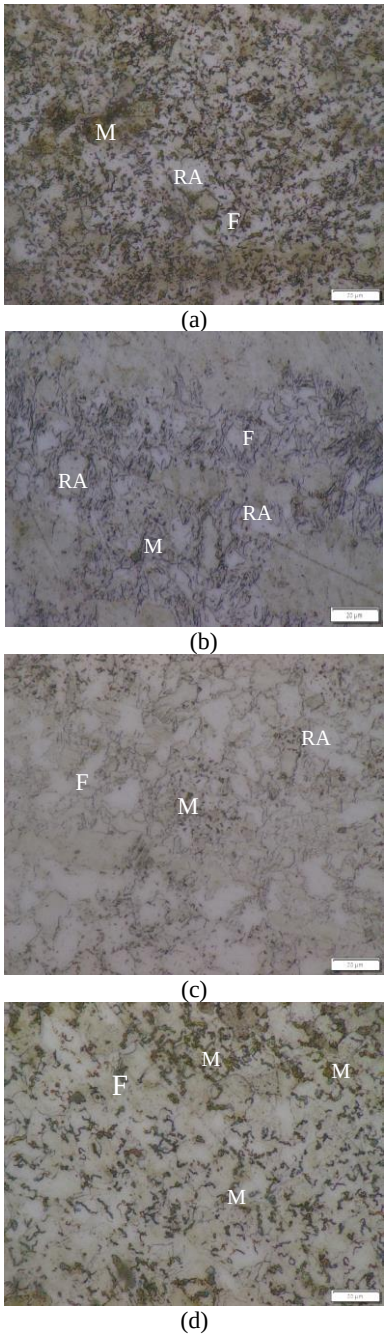


Gambar 3. Struktur mikro pada material (a) 0,42, (b) 1, (c) 2, dan (d) 3 %berat nikel setelah proses penempaan dan perlakuan panas yang dilanjutkan dengan pendinginan air (M= martensit, RA= austenit sisa, F = ferit). Etsa Pikral

Bentuk bilah martensit sebagai dampak kandungan karbon rendah pada baja laterit yakni 0,13-0,19%. Fasa martensit cenderung memiliki sifat keras dan kekuatan tinggi.

Selama perlakuan panas di atas temperatur $A_1$, ada sebagian fasa austenit tidak bertransformasi setelah pendinginan cepat karena stabilitas termal yang tinggi. Bagian yang tidak bertransformasi menjadi martensit ini yang disebut austenit sisa. Seiring pertambahan kadar nikel, butir RA berukuran semakin besar yang ditunjukkan dengan luas area berwarna putih yang semakin besar. Struktur mikro ini sesuai dengan penelitian oleh Hasbi, dkk., [12] martensit merupakan fasa metastabil yang terbentuk dikarenakan kecepatan pendinginan dengan media air tidak memberikan waktu untuk karbon berdifusi menjadi ferit pada baja laterit. Selain itu, pada konsentrasi yang lebih tinggi (1-5 %berat nikel), struktur mikro akhir mengarah pada peningkatan kandungan austenit sisa pada semua temperatur dan kandungan karbon [13]. Elemen paduan penstabil austenit berupa C, Mn, dan Ni memegang peranan penting pembentukan fasa RA.

Setelah perlakuan panas, perlit dari keadaan tempa berubah menjadi ferit, martensit, dan austenit yang tertahan. Butir austenit yang lebih kecil membentuk bilah martensit yang lebih halus setelah perlakuan panas, sedangkan martensit yang lebih panjang dalam baja laterit juga berarti ada butir yang lebih besar sebelum austenit diubah menjadi bainit dan martensit [11].

### 3.2. Pengujian Kekerasan

Pengujian kekerasan dilakukan untuk mengetahui korelasi kandungan fasa dengan kekerasan akibat pengaruh penambahan nikel pada modifikasi baja laterit A-588. Nilai kekerasan tersebut merupakan hasil rata-rata kekerasan dari 5 titik pada setiap sampel dengan menggunakan metode Brinell.

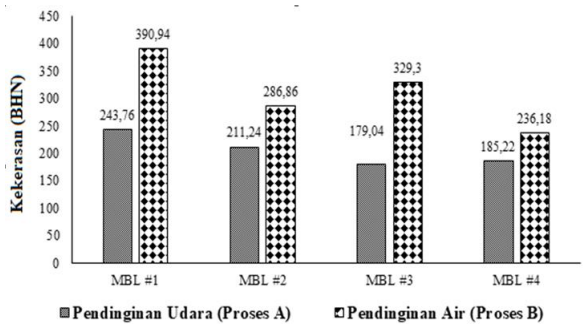


Gambar 4. Nilai kekerasan pada modifikasi baja laterit A-588

Nilai kekerasan modifikasi baja laterit dengan penambahan kadar nikel setelah mengalami proses tempa panas dan perlakuan

panas ditunjukkan pada Gambar 4. Secara umum, penambahan kadar nikel mempengaruhi pola nilai kekerasan secara signifikan pada kedua proses A dan B. Semakin tinggi kadar nikel (hingga 3 %berat), semakin turun nilai kekerasannya. Pada MBL#1 dengan 0,42 %berat nikel, nilai kekerasan mencapai 243,76 BHN (sekitar 23 HRC) setelah tempa panas dan dilanjutkan *normalizing*. Sedangkan, pada MBL#4 dengan 3 %berat nikel, nilai kekerasannya menurun menjadi 185,22 BHN (sekitar 11 HRC). Penurunan ini disebakan oleh ukuran butir akhir semakin besar dan terbentuknya austenit tertahan. Nikel mempengaruhi energi penyusunan ulang sedemikian rupa pada saat transformasi fasa austenit sehingga lebih mudah bagi ferit untuk mengalami deformasi plastis pada temperatur rendah [11],[13].

Dengan kadar nikel yang sama, adanya proses perlakuan panas dengan pendinginan cepat akan memberikan nilai kekerasan yang lebih tinggi jika dibandingkan dengan proses A. Peningkatan kekerasan ini disebabkan oleh terbentuknya fasa akhir martensit sebagai matriks. Pada 0,42 %berat nikel, variabel perlakuan panas memberikan nilai kekerasan sebesar 390,94 BHN (setara 42 HRC) dengan fasa akhir berupa ferit + perlit. Nilai ini jauh lebih tinggi jika dibandingkan dengan hasil tanpa perlakuan panas, yakni nilai kekerasan sebesar 236,18 BHN atau setara 22 HRC dengan fasa akhir berupa ferit + martensit + sisa austenit. Martensit berperan penting dalam meningkatkan nilai kekerasan akibat adanya tegangan dari karbon yang terperangkap ke dalam struktur kristal BCT (*body centered tetragonal*).

### 3.3. Pengujian Tarik

Pengujian tarik berfungsi untuk mengetahui pengaruh kadar nikel terhadap tingkat kekuatan dan keuletan baja laterit ketika dikenai beban statis. Hasil uji tarik ditunjukkan pada Gambar 5 dan 6.

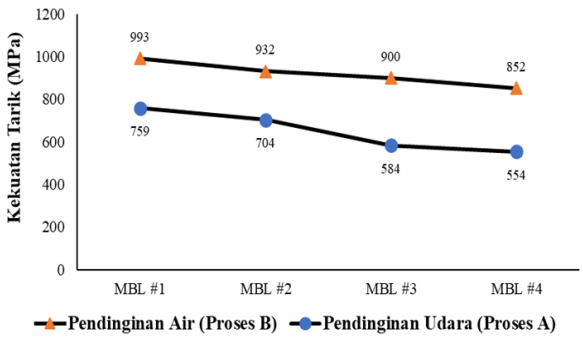


Gambar 5. Nilai kekuatan tarik maksimum (UTS) pada modifikasi baja laterit A-588

Secara umum, berdasarkan Gambar 5 dan 6, kekuatan tarik maksimum (*ultimate tensile strength*-UTS) setelah proses A dan B akan semakin menurun dan sifat keuletan semakin meningkat seiring dengan pertambahan 3 %berat nikel. Pola penurunan nilai kekuatan tarik sesuai dengan pola penurunan nilai kekerasan untuk semua modifikasi baja laterit. Pada proses tempa panas dengan pendinginan udara, kekuatan tertinggi sebesar 759 MPa diperoleh pada MBL#1 dengan kandungan 0,42 %berat nikel, dan kekuatan terendah sebesar 554 MPa diperoleh pada MBL#4 dengan kandungan 3 %berat nikel. Sedangkan untuk proses B dengan pendinginan air, kekuatan tertinggi sebesar 993 MPa diperoleh pada MBL#1 dengan kandungan 0,42 %berat nikel, dan kekuatan terendah sebesar 852 MPa diperoleh pada MBL#4 dengan kandungan 3 %berat nikel. Nikel dan krom cenderung menurunkan temperatur transformasi pembentukan martensit (Ms) sehingga jumlah martensit yang terbentuk lebih sedikit, kekuatan cenderung menurun, membentuk pola patahan *quasi-cleavage* dengan karakteristik campuran getas-ulet [14]. Selain itu, nikel mempengaruhi ukuran butir semakin besar sehingga memungkinkan deformasi plastis yang cukup besar akibat inisiasi fraktur ulet dari dominasi fasa ferit sebanyak 72-77 $\%V_f$. Nilai regangan dikonfirmasi pada Gambar 6.

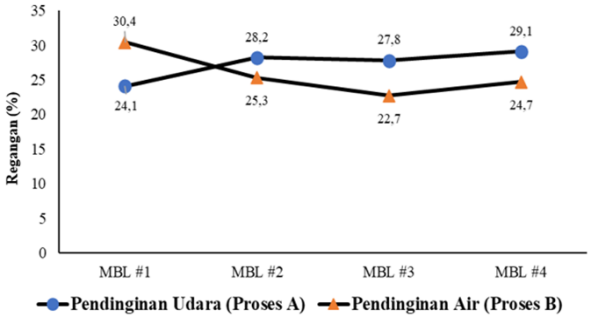


Gambar 6. Nilai regangan pada modifikasi baja laterit A-588

Pada modifikasi baja laterit, proses B (tempa dan dilanjutkan perlakuan panas dengan pendinginan air) menghasilkan kekuatan tarik lebih tinggi 130-150% jika dibandingkan dengan proses A (tempa dan dilanjutkan perlakuan panas dengan pendinginan udara). Kadar nikel memberikan efek yang signifikan berbeda pada pola regangan. Pada proses A dengan pendinginan udara, nilai regangan cenderung naik namun tidak signifikan seiring dengan bertambahnya nikel. Sedangkan, pada proses B, nilai regangan cenderung menurun seiring dengan bertambahnya nikel. Hal ini disebabkan oleh deformasi menyebabkan transformasi

austenit menjadi martensit. Nikel memfasilitasi distribusi slip lebih homogen di seluruh matriks dan proses rekristalisasi yang terjadi bersamaan dengan deformasi akibat tempa panas sehingga menghindari pengerasan regangan dan berakibat nilai keuletan naik [14].

Nilai kekuatan tarik maksimum dan regangan pada baja laterit A-588 melebihi nilai standar A-588 komersil, yakni 485 MPa dan 21% untuk jenis plat dengan ketebalan kurang dari 100 mm [8]. Oleh karena itu, baja laterit mampu menjadi alternatif bahan baku untuk diproses lebih lanjut menjadi baja tahan cuaca.

### 3.4. Pengujian Korosi

Kurva polarisasi modifikasi baja laterit A-588 dalam larutan NaCl 3,5 %berat setelah proses tempa dengan variasi proses perlakuan panas ditunjukkan oleh Gambar 7 dan 8. Gambar tersebut menunjukkan perubahan potensial korosi ($E_{corr}$) dan rapat arus korosi ($I_{corr}$) yang terjadi selama penambahan kadar nikel dan perbedaan perlakuan panas.

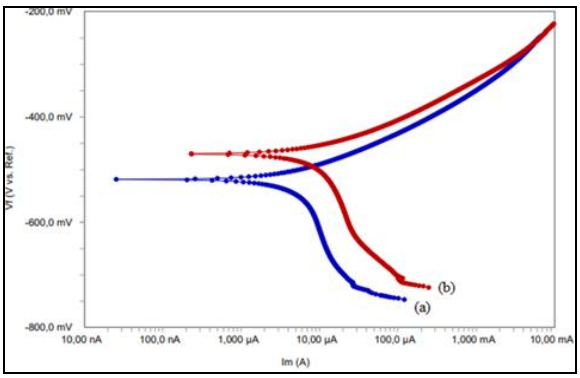


Gambar 7. Kurva polarisasi E versus Log I hasil tempa panas + pendinginan udara (a) 0,42 dan (b) 2 %berat nikel

Gambar 7 menunjukkan perubahan kurva polarisasi yang terjadi pada modifikasi baja laterit hasil tempa panas dan pendinginan udara dengan kadar nikel 0,42 %berat dan 2%berat. Dengan 2 %berat nikel dan bentuk butiran ferit agak kasar, kurva polarisasi bergeser ke kanan atas yang menunjukkan bahwa $I_{corr}$ semakin besar dan $E_{corr}$ semakin positif, yakni -468,4 mV dan $8{,}315 \times 10^{-6}$ A/cm². Hal ini menandakan bahwa pertambahan 2 %berat nikel setelah tempa panas lebih mudah terkorosi akibat dominasi perubahan reaksi anodik dengan elektrolit NaCl 3,5 %volume dengan kondisi belum terbentuknya lapisan protektif antara Cr-Ni-Cu [5]. Selain itu, perbedaan karakteristik elektrokimia berkaitan dengan perbedaan struktur fasa dan ukuran butir. Semakin besar ukuran butir maka celah antar butir semakin besar sehingga semakin mudah terjadinya korosi galvanik, meskipun nikel merupakan salah satu unsur tahan korosi selain Mn, Cr, Cu, dan Mo. Adanya perbedaan fasa yang signifikan menimbulkan kondisi lebih galvanik. Pada baja karbon rendah, struktur butiran ferit berbentuk kolom halus memanjang cenderung lebih stabil terhadap korosi NaCl dan struktur butir kasar menunjukkan perilaku aktif dalam elektrolit [15].

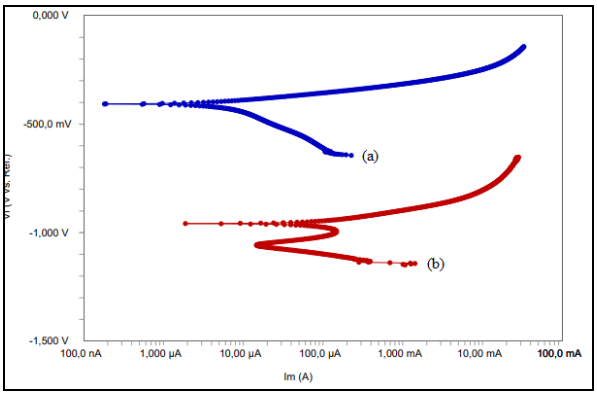


Gambar 8. Kurva polarisasi E versus Log I modifikasi baja laterit A-588 hasil tempa panas + pendinginan air dengan (a) 0,42 dan (b) 2 %berat nikel

Gambar 8 menunjukkan perubahan kurva polarisasi yang terjadi pada modifikasi baja laterit hasil tempa panas yang dilanjutkan proses pemanasan dengan pendinginan air. Akibat penambahan 2 %berat nikel, kurva polarisasi bergeser ke kanan bawah yang menunjukkan $I_{corr}$ lebih besar dan $E_{corr}$ semakin negatif, yakni -994 mV dan $32{,}78 \times 10^{-6}$ A/cm². Hal ini menandakan bahwa baja laterit dengan 2 %berat nikel yang diproses tempa panas dan perlakuan panas fasa ganda menunjukkan lebih terkorosi dalam larutan 3,5 %volume NaCl. Hal ini berkolerasi dengan hasil pengamatan mikro yang menunjukkan fasa austenit sisa dan martensit sebagai fasa aktif. RA cenderung memiliki aktivitas energi lebih tinggi dan kadar karbon lebih tinggi dari fasa martensit sehingga efek peningkatan korosi galvanik dan disolusi selektif marginal terlihat sangat jelas dengan meningkatnya laju korosi [16].

Nilai laju korosi untuk masing-masing modifikasi baja laterit yang diuji pada larutan 3,5 %volume NaCl ditunjukkan pada Tabel 3. Secara umum, penambahan 2 %berat nikel pada modifikasi baja laterit A-588 memiliki $I_{corr}$ dan laju korosi yang lebih tinggi, yakni 3,8 mpy untuk proses A, dan 14,98 mpy untuk proses B. Selain itu, proses kombinasi tempa panas dan perlakuan panas memberikan efek signifikan terhadap perubahan polarisasi. Dengan kadar nikel sama, perlakuan panas dengan pendinginan air memberikan laju korosi lebih tinggi. Hal ini disebabkan oleh perbedaan fasa akhir yang terkandung dalam baja laterit.

Jika dibandingkan dengan A-588 komersil, baja laterit A-588 setelah proses tempa dan penambahan 2 %berat nikel memiliki ketahanan korosi lebih tinggi. ASTM A-588 komersil tanpa penambahan lapisan cat memiliki nilai $E_{corr}$ dan $I_{corr}$ sebesar -693 mV dan 85 µm/cm$^2$ jika terpapar dengan 3,5 %berat NaCl [17]. Laju korosi imersi lebih tinggi dibandingkan dengan laju korosi atmosferik

Tabel 3. Parameter korosi pada modifikasi baja laterit A-588 dalam larutan 3,5 %volume NaCl

| Properties | Proses A (tempa panas + pendinginan udara) | | Proses B (tempa panas + pendinginan air) | |
|---|---|---|---|---|
| | 0,42% Ni | 2% Ni | 0,42% Ni | 2% Ni |
| Beta ($10^{-3}$ V/decade) | 66,37 | 65,32 | 40,74 | 173,7 |
| Potensial korosi (mV) | -515,5 | -468,4 | -405,6 | -994,0 |
| Rapat arus korosi ($10^{-6}$ A/cm²) | 3,714 | 8,315 | 4,549 | 32,78 |
| Laju korosi (mpy) | 1,697 | 3,800 | 2,078 | 14,98 |

## 4. KESIMPULAN

Proses TMCP (*thermo mechanical control process*) berupa kombinasi penempaan panas dengan perlakuan panas diterapkan pada baja laterit A-588 yang dimodifikasi kandungan nikelnya. Kadar nikel mempengaruhi ukuran butir fasa serta fraksi fasa ferit-perlit pada tempa panas dilanjutkan pendinginan udara. Dengan 3 %berat nikel, ukuran butir ferit-perlit yang terbentuk semakin besar yakni ±0,1 mm (ASTM G nomor 3,7), sehingga kekerasan dan kekuatan menjadi semakin turun hingga 185,22 BHN dan 554 MPa, serta regangan semakin meningkat sebesar 29,1%. Perbedaan fasa akhir menimbulkan kondisi lebih galvanik sehingga baja laterit lebih terkorosi dengan laju korosi sebesar 3,8 mpy. Pada baja paduan rendah, butiran ferit berbentuk kolom halus cenderung lebih tahan terhadap korosi NaCl, sedangkan butiran kasar menunjukkan perilaku lebih aktif. Pada baja laterit setelah proses tempa panas dan perlakuan panas dengan pendinginan air, 3 %berat nikel menyebabkan terbentuknya fasa dislokasi bilah martensit + ferit + austenit sisa sehingga kekerasan, kekuatan, dan regangan menurun hingga 236,18 BHN, 852 MPa, dan 24,7%. Fasa austenit sisa memiliki efek merusak pada sifat mekanis dan sifat korosi.

Secara umum, tujuan pembentukan baja tahan cuaca dari baja laterit A-588 belum optimal dalam hal sifat mekanik dan ketahanan korosi. Oleh karena itu, diperlukan penelitian lebih lanjut untuk menganalisis parameter lainnya seperti kadar nikel lebih tinggi, temperatur pemanasan pada proses perlakuan panas, serta proses termomekanikal lainnya.

## UCAPAN TERIMA KASIH

Penulis mengucapkan terimakasih kepada kelompok penelitian Baja Tahan Cuaca. Penelitian ini didanai oleh DIPA Pusat Penelitian Metalurgi dan Material pada tahun 2019.

## DAFTAR PUSTAKA

[1] M. Morcillo, I. Díaz, B. Chico, H. Cano, and D. de la Fuente, "Weathering steels: from empirical development to scientific design. A review," *Corros. Sci.*, vol. 83, pp. 6–31, 2014. Doi: 10.1016/j.corsci.2014.03.006.

[2] V. Urban, V. Krivy, and K. Kreislova, "The development of corrosion processes on weathering steel bridges," *Procedia Eng.*, vol. 114, pp. 546–554, 2015. Doi: 10.1016/j.proeng.2015.08.104.

[3] M. Morcillo, I. Díaz, H. Cano, B. Chico, and D. de la Fuente, "Atmospheric corrosion of weathering steels. Overview for engineers. Part I: Basic concepts," *Constr. Build. Mater.*, vol. 213, pp. 723–737, 2019. Doi: 10.1016/j.conbuildmat.2019.03.334.

[4] K. Zacek, Ondrej;Liska, Miroslav;Kreislova, "Development of new structural weathering steels," *Metals (Basel).*, vol. 19, no. 21, pp. 1–12, 2009.

[5] X. M. Xiao, Y. Peng, C. Y. Ma, and Z. L. Tian, "Effects of alloy element and microstructure on corrosion resistant property of deposited metals of weathering steel," *J. Iron Steel Res. Int.*, vol. 23, no. 2, pp. 171–177, 2016. Doi: 10.1016/S1006-706X(16)30030-9.

[6] Y. Zhou, J. Chen, Y. Xu, and Z. Liu, "Effects of Cr, Ni and Cu on the corrosion behavior of low carbon microalloying steel in a Cl- containing environment," *J. Mater. Sci. Technol.*, vol. 29, no. 2, pp. 168–174, 2013. Doi: 10.1016/j.jmst.2012.12.013.

[7] X. Cheng, Z. Jin, M. Liu, and X. Li, "Optimizing the nickel content in weathering steels to enhance their corrosion resistance in acidic atmospheres," *Corros. Sci.*, vol. 115, pp. 135–142, 2017. Doi: 10.1016/j.corsci.2016.11.016.

[8] A. International, "Standard specification

for high-strength low-alloy structural steel with 50 ksi [345 MPa] minimum yield point to 4 in [100 mm] thick 1," West Conshohocken, 1998.
[9] M. Zhan, Z. Sun, and H. Yang, "*5.20 - modeling of hot forging*," in Comprehensive Materials Processing, vol. 5: Casting, J. McGeough, Ed. New York: Elsevier, 2014, pp. 441–493.
[10] M. A. Irshad, "The effect of prior austenite grain size on the machinability of a pre-hardened mold steel," *Master's degree Diss.*, p. 77, 2011.
[11] F. Zhang, Y. Yang, Q. Shan, Z. Li, J. Bi, and R. Zhou, "Microstructure evolution and mechanical properties of 0.4C-Si-Mn-Cr steel during high temperature deformation," *Materials (Basel).*, vol. 13, no. 1, 2020. Doi: 10.3390/ma13010172.
[12] M. Y.. Hasbi, T. B. Romijarso, P. A. Paristiawan, "Pengaruh kecepatan pendinginan baja fasa ganda Fe-Ni dan nilai kekerasan," *J. Teknol. Bahan dan Barang Tek.*, vol. 10, no. 2, pp. 84–91, 2020. Doi: 10.37209/jtbbt.
[13] E. Keehan, L. Karlsson, and H. O. Andren, "Influence of carbon, manganese and nickel on microstructure and properties of strong steel weld metals: Part 1 - Effect of nickel content," *Sci. Technol. Weld. Join.*, vol. 11, no. 1, pp. 1–8, 2006. Doi: 10.1179/174329306X77830.
[14] C. G. Norwood, "The effect of nickel content on the mechanical properties and microstructure of a high toughness secondary hardening steel," Carnegie Mellon University (Thesis), Pittsburgh, 2016.
[15] H. Zhang, C. Wang, B. Xue, and J. Luo, "Effect of grain size on the corrosion resistance of low carbon steel," *Mater. Sci. Forum*, vol. 984, pp. 43–50, 2020. Doi: 10.4028/www.scientific.net/msf.984.43.
[16] Neetu, P. K. Katiyar, S. Sangal, and K. Mondal, "Effect of various phase fraction of bainite, intercritical ferrite, retained austenite and pearlite on the corrosion behavior of multiphase steels," *Corros. Sci.*, vol. 178, p. 109043, 2021. Doi: 10.1016/j.corsci.2020.109043.
[17] Q. A. . Kaseasbeh, "Electrochemical investigation of corrosion resistance of North Dakota State University," *North Dakota State Univ.*, no. November, 2015.

# INDEKS PENULIS

# INDEKS KATA